

# ULRR

## Non-invasive haemoglobin monitoring by an LED based optical sensor system

Item Type	Thesis
Authors	Timm, Ulrich
Download date	2026-05-13 01:08:04
Item License	<a href="https://creativecommons.org/licenses/by-nc-sa/1.0/">https://creativecommons.org/licenses/by-nc-sa/1.0/</a>
Link to Item	<a href="https://hdl.handle.net/10344/4768">https://hdl.handle.net/10344/4768</a>



# NON-INVASIVE HAEMOGLOBIN MONITORING BY AN LED BASED OPTICAL SENSOR SYSTEM

Dipl.- Ing. Ulrich Timm

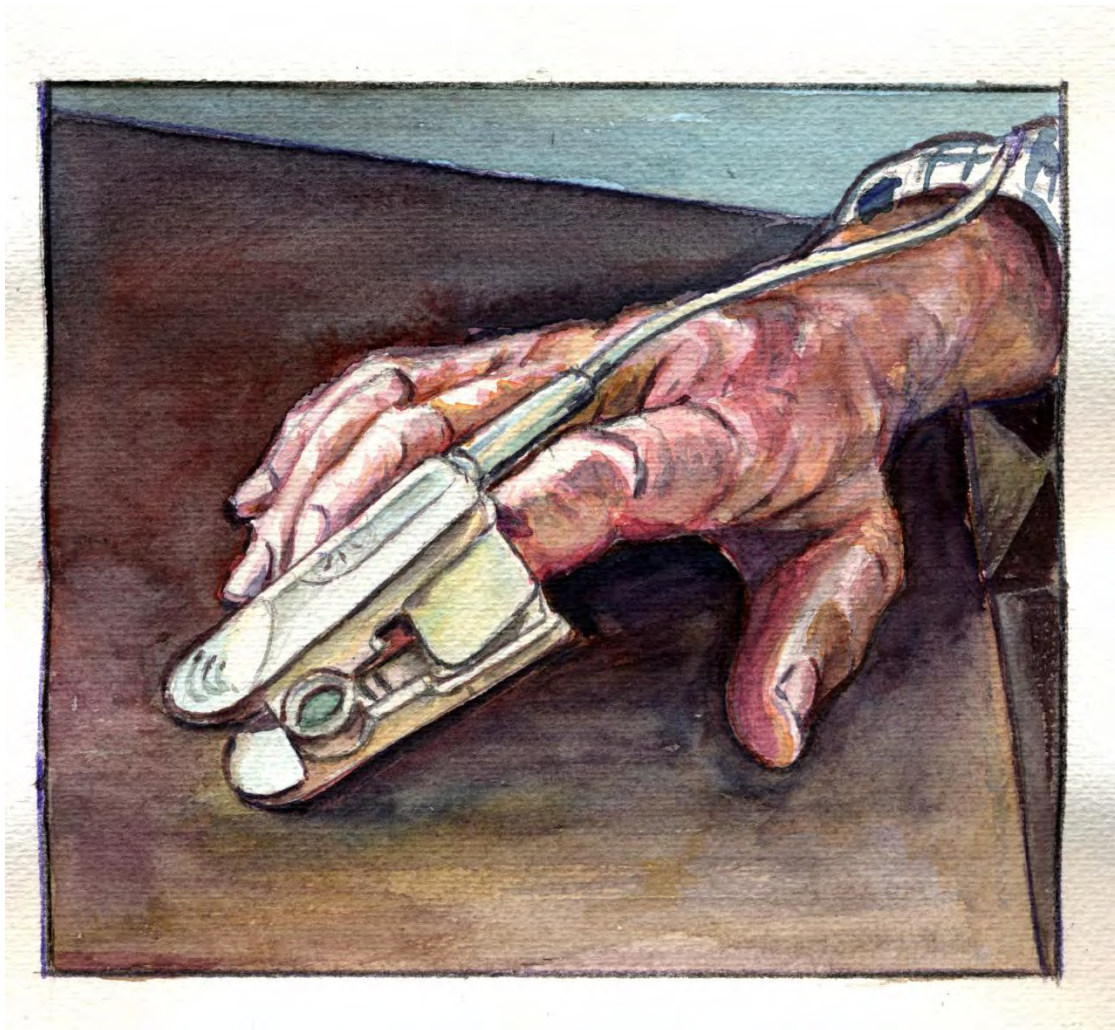
Optical Fibre Sensors Research Centre  
Department of Electronic and Computer Engineering

University of Limerick

Thesis submitted for the degree of Doctor of Philosophy (Ph.D.)

University of Limerick

November 2010



*Commissioned by Ulrich Timm. Artist: Werner Peters, Date: 15.8.2010*

# Abstract

During the perioperative period, which includes the period before surgery (preoperative), during surgery (intraoperative) and after surgery (postoperative), it is essential to measure diagnostic parameters such as: blood oxygen saturation; haemoglobin (Hb) concentration; and pulse rate. The Hb concentration in human blood is an important parameter to evaluate the physiological condition of an individual, as Hb is the oxygen carrying component of red blood cells. By determining the Hb concentration, it is possible, for example, to observe intraoperative or postoperative bleeding, and use this information as a trigger for autologous/allogenic blood transfusions.

The primary objective of this research has been the development of a non-invasive, real-time, Haemoglobin monitor based on the photo-plethysmography (PPG) method and using LEDs as the frequency sources. The system developed operates in the spectral range between 600nm and 1400nm. In an analogous way to pulse oximeters, the Hb sensor is clipped on a fingertip and light is transmitted through the fingertip. The system provides continuous real-time monitoring of the Hb concentration without the need to take blood samples.

This thesis discusses the theory needed to understand and design such a device, e.g.: the transport of light in biological tissue and turbid media; the PPG method; and a model for non-invasive Hb measurement is derived from first principles.

In order to empirically validate the theory of the Hb system, a prototype Hb sensor system and an artificial blood flow model were constructed, which simulate the human circulatory system. The blood flow model allowed a controlled variation of the oxygen saturation and haemoglobin concentration. Results obtained from spectrometer measurements and from the non-invasive Hb sensor system are presented in this thesis.

Furthermore, an in vivo validation was undertaken, where the non-invasive method was compared with an invasive method and an excellent correlation were observed.

# Acknowledgement

I would like to thank my supervisors, Prof. Elfed Lewis and Prof. Hartmut Ewald for their advice and guidance throughout the last number of years. I would also like to thank everyone in the Optical Fibre Sensors Research Centre. They have always been there to give advice and support.

Special thanks to Benno Mossau, Dr. Jens Kraitl and Dr. Gabriel Leen for their help, advice and guidance.

I also wish to express my thanks to those at the Graduate Entry Medical School of the University of Limerick for everything they did, specifically Dr. Deirdre McGrath and Dr. Margaret Toomey.

I would like to thank the Irish Research Council for Science, Engineering and Technology for funding this work.

My family also deserve special thanks, for all the support they have given me over the years.

I would finally like to extend my thanks to all my friends outside of the University who have been a constant support.



5.2	Measurement Method Photoplethysmography.....	50
5.3	Measurement Method Pulse Oximetry .....	51
5.4	Concept of Non-Invasive Haemoglobin Determination.....	57
5.5	Summary .....	60
6	Hb Sensor System .....	61
6.1	Introduction .....	61
6.2	Light sources .....	61
6.3	The Sensor.....	67
6.4	Basic Sensor System.....	70
6.5	Software .....	73
6.5.1	Algorithmic .....	75
6.5.1.1	Validation of the Algorithm.....	77
6.6	Summary .....	80
7	Validation with the blood flow model.....	81
7.1	Introduction .....	81
7.2	The Blood Flow Model .....	81
7.3	Spectrometer Measurements.....	82
7.4	Hemocue vs BGA.....	85
7.5	Blood flow model measurement with the non –invasive haemoglobin sensor system .....	86
7.6	Summary .....	89
8	Online Measurements <i>in vivo</i> .....	90
8.1	Introduction .....	90
8.2	The calibration curve.....	93
8.3	Validation of the calibration curve .....	95
8.4	Discussion.....	98
9	Summary and Outlook.....	100
10	Own Publications.....	102
11	References.....	104
12	Appendix.....	110
12.1	Screenshot Block Diagram LabVIEW .....	110
12.2	Ethic Approval University of Limerick .....	111

# List of Figures

Figure 2-1: ABL800 Flex Blood Gas Analyser from the company Radiometer [96] .....	5
Figure 2-2: Optoacoustic Haemoglobin Determination in Tissue Phantom [11] .....	6
Figure 2-3 Amplitude of the optoacoustic signal measured from the radial artery and actual total haemoglobin concentration during dilution study. [12] .....	7
Figure 2-4: Electrical admittance PG by Yamakoshi et al. with a cuff [14] .....	9
Figure 2-5: Measurement principle of the Astrim Sysmex [17].....	11
Figure 2-6: Comparison of Non- invasive and Invasive method by Nori et al. [20].....	12
Figure 2-7: Orsense NBM-200 [22] .....	13
Figure 2-8: Crit-Scan from Hemametrics [25].....	13
Figure 3-1: Absorption and Scattering in human tissue .....	15
Figure 3-2: Absorption of a Photon and Excitation of the Atom .....	17
Figure 3-3: Anisotropy factor $g$ and the resulting direction of scattering.....	20
Figure 3-4: The water absorption spectra [91] .....	22
Figure 3-5: Intensity scattering in a cylindrical portion in the volume.....	26
Figure 3-6: Illustration of the diffuse radiance in the diffuse approximation .....	29
Figure 3-7: Ulbricht Sphere Single measurement [50] .....	32
Figure 3-8: Ulbricht Sphere Dual Setup [50] .....	33
Figure 3-9: Schematic Goniophotometer .....	33
Figure 4-1: Erythrocytes Concentrate (red, left) and Blood Plasma (yellow, right) in 250ml blood bags.....	35
Figure 4-2: Oxygen transport by haemoglobin [94] .....	36
Figure 4-3: Oxyhaemoglobin dissociation curve [58] .....	39
Figure 4-4: Extinction coefficient of the four most common haemoglobin derivates [75].....	40
Figure 4-5: Blood Absorption spectra ( $cHb = 18g/l$ ) for oxyhaemoglobin, reduced haemoglobin and water [61].....	41
Figure 4-6: The Human Circulatory System [95] .....	43

Figure 4-7: Typical pulse wave obtained with the Non-Invasive Haemoglobin Sensor System.....	44
Figure 4-8: Three-dimensional view of the skin [65] .....	45
Figure 4-9: The reduced scattering coefficient as function as function of the wavelength, equation 4-5.....	47
Figure 4-10: Absorption Spectra of Melanin, Epidermis and Unpigmented Skin from 600 to 1600nm.....	48
Figure 5-1: Model of the Tissue Layers and composition of the AC and DC part.....	53
Figure 5-2: Illustration of the hand vessels.....	54
Figure 5-3: Pulse oxymeter wavelengths and the absorption spectra of oxygenated and deoxygenated haemoglobin .....	55
Figure 5-4: The commercial pulse oximeter calibration curve in comparison with Beer-Lambert for the Philips Sensor M1190A [77] .....	57
Figure 5-5: Transmission spectra with different oxygenation levels and identical Hb of 80 g/l. ....	58
Figure 6-1: Typical LED characteristic graph .....	62
Figure 6-2: Adjustable current source .....	63
Figure 6-3: 670nm LED relative output spectra at 5mA A: raw data 660nm-680nm B: peak wavelength shift C: raw data with periodic fluctuations D: averaged wavelength shift at 668nm .....	64
Figure 6-4: 670nm LED relative output spectra at 20mA A: raw data 660nm-680nm B: peak wavelength shift C: raw data with periodic fluctuations D: averaged wavelength shift at 671nm .....	65
Figure 6-5: Wavelength shift 810nm LED [80] .....	66
Figure 6-6: Wavelength shift 1300nm LED [80] .....	66
Figure 6-7: Responsivity diagram of Silicon, Gallium Arsenide and Indium Gallium Arsenide photodiodes .....	67
Figure 6-8: Spectral responsivity of the InGaAs/InP photodiode [80].....	68
Figure 6-9: Transimpedance amplifier stage with OPA381 .....	69
Figure 6-10: Look inside the finger clip, transimpedance amplifier mounted on the rear side of the PCB .....	70
Figure 6-11: Schematic of the Sensor System .....	71
Figure 6-12: Timing Diagram MSP430 .....	72
Figure 6-13: Hb Sensor System .....	73
Figure 6-14: Screenshot of the Main Application .....	74
Figure 6-15: Architecture of the detection & AC/DC estimator algorithm. ....	75
Figure 6-16 Peak/Valley algorithm .....	76

Figure 6-17: Measuring set-up during dialysis session .....	77
Figure 6-18: AC/DC calculation. Patient state: normal/deoxygenation. ....	78
Figure 6-19: AC/DC calculation. Patient state: pacemaker .....	79
Figure 6-20: AC/DC calculation. Patient state: diabetic angeopathy .....	79
Figure 7-1: Setup Blood Flow Model.....	82
Figure 7-2: Blood spectrum from 600nm to 1400nm in dependence to the oxygen saturation .....	83
Figure 7-3: Absorption spectrum of blood from 600nm to 1700nm in dependence to the oxygen saturation and haemoglobin concentration .....	84
Figure 7-4: Comparison HemCue and Blood Gas Analyser.....	85
Figure 7-5: Corrupted pulse waves during blood flow model measurements.....	86
Figure 7-6: Transmission signals of the non-invasive haemoglobin sensor system and calculated ratios during a de-oxygenation ( $sO_2=97.9\%$ down to $sO_2=50.9\%$ , $cHb=8.5\text{mmol/l}$ ) .....	87
Figure 7-7: Calculated ratios during stepwise cHb change and oxygenation.....	88
Figure 8-1: Hb reference device HemoCue Hb 201+ with cuvette .....	90
Figure 8-2: Raw PPG signals from a measurement using the non-invasive Hb finger clip probe during the calibration study.....	91
Figure 8-8-3: Raw signals and corresponding ratios for $SpO_2$ and cHb .....	92
Figure 8-4: Comparison 1300nm/810nm ratio with the invasive measured value from HemoCue .....	93
Figure 8-5: Influence of the contact pressure in pulse oximetry [90] .....	94
Figure 8-6: Raw signals and calculated ratios with raised contact pressure.....	95
Figure 8-7: Comparison of twenty measurements from non-invasive Hb device and the HemoCue.....	96
Figure 8-8: Bland Altman Plot to compare both measurement methods.....	97
Figure 8-9: Comparison of two finger clips.....	98
Figure 8-10: Wavelength shift between two clips .....	99

# List of Tables

Table 1: Haemoglobin reference range [52] .....	37
Table 2: Hematocrit reference range [52] .....	38
Table 3: Melanin concentration standard values for different type of skin [68] .....	48
Table 4: Initial condition for three data sets for the algorithm validation .....	78
Table 5: Statistical Distribution of the Peak to Peak and Pulse Energy algorithm .....	80

# Glossary

ADC	Analog-to-Digital Converter
BGA	Blood Gas Analysis
CCD	Charged-Coupled Device
Cn-Met-Hb	Cyanmet-haemoglobin
CO <sub>2</sub>	Carbon dioxide
ctHb	Concentration of haemoglobin
DA	Diffusion Approximation
DAC	Digital-to-Analog Converter
DPG	2.3 Diphosphoglyerat
$\epsilon$	Molar extinction coefficient
g	Anisotropy factor
H <sup>+</sup>	Hydrogen ions
Hb	Haemoglobin
HHb	Deoxyhaemoglobin
HbO <sub>2</sub>	Oxyhaemoglobin
Hct	Hematocrit
InGaAs	Indium Gallium Arsenide
InP	Indium Phosphor
$\mu_a$	Absorption coefficient
$\mu_s$	Scattering coefficient
LED	Light Emitting Diode
MC	Monte Carlo
NIR	Near-Infrared
OA	Optoacoustic
PM	Photomultiplier
PO <sub>2</sub>	Partial pressures of oxygen

PPG	Photoplethysmograph
Q	efficiency factor
$R_{\text{diff}}$	Diffuse reflection
RTT	Radiative Transfer Theory
Si	Silicon
SpO <sub>2</sub>	Saturation of Peripheral Oxygen
SNR	Singal-to-Noise Ratio
SPI	Serial Peripheral Interface Bus
$T_{\text{coll}}$	Collimated transmission
$T_{\text{diff}}$	Diffuse transmission
$T_{\text{tot}}$	Total transmissin

## 1 Introduction

This chapter introduces the objective and motivation of this research, to develop a method to non-invasively monitor the total haemoglobin concentration. Haemoglobin (Hb) is an important component of red blood cells. The primary function of Hb is the transport of oxygen from the lungs to the tissue and the transport of carbon dioxide back to the lungs. The total Hb concentration in human blood is an important parameter in evaluating the physiological status of an individual and is an essential parameter in every blood count. Currently invasive methods are used in clinical environments to measure the Hb concentration, whereby blood is taken from the patient and subsequently analysed. Apart from the discomfort of drawing blood samples, an added disadvantage of this method is the delay between the blood collection and its analysis, which does not allow real-time patient monitoring in critical situations. A non-invasive method allows pain free continuous on-line patient monitoring with minimum risk of infection and facilitates real-time data monitoring allowing immediate clinical reaction to the measured data. This final section of this introductory chapter will give an overview of the research towards the goal of developing a non-invasive LED based optical sensor system for the measurement of total haemoglobin.

Chapter 3 introduces the light transport characteristics of biological tissue, and turbid media, and concludes with a discussion of the different models of light propagation.

In Chapter 4 the components of blood are discussed with particular reference to their optical properties. The human circulatory system is described with emphasis given to pulse wave formation.

Chapter 5 discusses the theory of pulse oximetry and a novel method to determine the haemoglobin concentration non-invasively.

Chapter 6 describes the developed sensor system and explains in detail the component of the system.

Chapter 7 first describes *in vitro* validation of the sensor system and the novel method developed to measure total haemoglobin. The *in vitro* measurements are

performed on an artificial blood flow model which simulates the human circulatory system.

In Chapter 8 the *in vivo* validation procedure and results are discussed. Measurements taken with the non-invasive haemoglobin sensor system are compared with reference measurements taken with an invasive instrument.

Chapter 9 concludes the thesis with a review of the novel sensor system developed and the technique applied to measure haemoglobin concentration non-invasively. Suggestions for further work are also discussed in this final chapter.

## **2 Review of current techniques of Haemoglobin determination**

### **2.1 Introduction**

Physicians currently have three methods for assessing the Hb concentration of a patient's blood. There are as follows:

1. Perform a visual inspection of the palpebral conjunctiva. The palpebral conjunctiva is as opposed to the ocular (or bulbar) conjunctiva, the part of the conjunctiva that covers the outer surface of the eye. The visual inspection of the conjunctiva by a physician is at best only 70% accurate and depends on their experience and training.
2. Conduct a complete blood count test.
3. Using a small blood volume haemoglobimeter.

### **2.2 Invasive methods of Haemoglobin determination**

The reference procedure and most exact method to determine the haemoglobin concentration is the cyanmet-haemoglobin (CN-Met-Hb) method [1, 2]. In this case the haemoglobin is transformed to the chemical stable complex cyanmet-haemoglobin whose concentration gives an indication of haemoglobin concentration. The absorption maximum of the obtained cyanmet-haemoglobin complex is at a wavelength of  $546nm$  and by using a photometer the concentration can be determined.

A second method to determine the amount of haemoglobin can be realised by measuring the amount of the bound oxygen in the blood. A Blood Gas Analysis (BGA) for instance is a procedure to measure the partial pressure of oxygen ( $O_2$ ) and carbon dioxide ( $CO_2$ ) gases as well as the pH (hydrogen ion concentration) in arterial blood.

The blood sample is inserted into an analytical instrument that uses electrodes to measure the concentration of hydrogen ions ( $H^+$ ), which is reported as pH, and the partial pressures of oxygen ( $PO_2$ ) and carbon dioxide  $CO_2$  gases. The pH-measuring electrode consists of a special glass membrane that is selectively permeable to hydrogen ions. An electrical potential develops across the inner and outer surfaces of this membrane that is related to the log of hydrogen ion activity in the blood sample. A Severinghaus electrode is used to measure  $PCO_2$  [3]. The measuring principle is the same as for hydrogen ions, except that the electrode tip is covered with a gas permeable membrane, so that the pH change is proportional to carbon dioxide diffusing from the blood sample to the electrode surface.  $PO_2$  is measured using a polarographic (Clark) electrode [4]. Oxygen diffuses from the sample to the cathode, where it is reduced to peroxide ions. The electrons are provided by a silver anode that is oxidized, generating current in proportion to oxygen concentration at the cathode. Electrode signals are dependent upon temperature as well as concentration, and all measurements are performed at  $37^\circ C$  (body temperature). Since the *in vivo* pH, levels of oxygen, and carbon dioxide are temperature dependent, results may need to be adjusted for the patient's actual temperature. This method may also be used to calculate oxygen content, total carbon dioxide, base excess, and the percent oxygen saturation of haemoglobin [5]. In the clinical environment modern blood gas analysers such as the ABL 800Flex are used (Figure 2-1). Such an analyser is quite expensive but much cheaper transportable photometers are also commercially available (around 500Euro + Consumables).



Figure 2-1: ABL800 Flex Blood Gas Analyser from the company Radiometer [96]

An example of a transportable photometer is the HemoCue 201+ system from the company Mallinckrodt. [6] This device is based on the Azide methaemoglobin method which relies on the use of dry reagents [7]. These reagents are included in the micro cuvette and the reaction with the blood results in a stable complex which can be analysed at a wavelength of 570nm and 880nm. The procedure requires only a drop of blood to be extracted from the patient using a finger prick. The whole measurement procedure itself takes approximately one minute to perform.

## 2.3 Non- Invasive methods of Haemoglobin determination

### 2.3.1 Acoustic Methods

Photoacoustic spectroscopy is based on the photoacoustic effect. Alexander Graham Bell showed in 1880 that thin discs emitted sound when they were exposed to a beam of sunlight that was rapidly interrupted with a rotating slotted disk. The absorbed energy from the sunlight is transformed into kinetic energy which results in local heating and thus a pressure wave or sound wave is emitted. The photoacoustic effect can be used to study solids, liquids and gases [8]. Photoacoustic spectroscopy

has also been explored as a method to measure the haemoglobin non-invasively *in vitro* and *in vivo* [9,10,11]. A laser which is directed on the tissue causes a rapid thermal expansion. Depending on the tissue characteristic a pressure wave is created. In the near infrared range the absorption coefficient of haemoglobin is higher than the surrounding tissue which enhances the optically induced thermal modulation. *Petrova et al* [11] presented the optoacoustic signals measured in a tissue phantom which demonstrated a dependence on the haemoglobin concentration, see Figure 2-2.

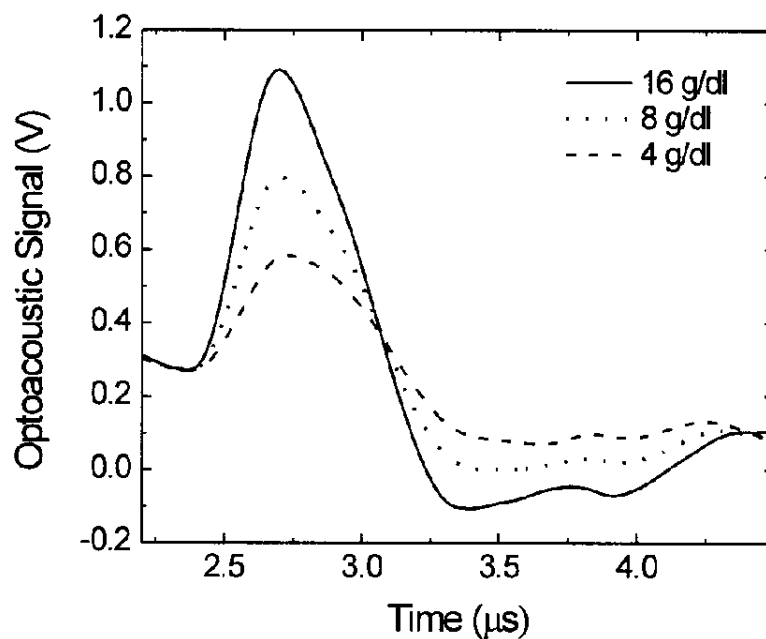


Figure 2-2: Optoacoustic Haemoglobin Determination in Tissue Phantom [11]

Additionally, *in-vivo* optoacoustic measurements performed at the wrist area, above the radial artery, have been studied [12]. The chosen location has the advantage that the optoacoustic measurement in the vessels is close to the surface and the oxygenation is close to 100%. For this reason there is no need for differentiation between the haemoglobin derivatives i.e. oxygenated and reduced. During the *in-vivo* test reported, a saline solution was injected to change the total haemoglobin concentration. The results of this work are shown in Figure 2-3.

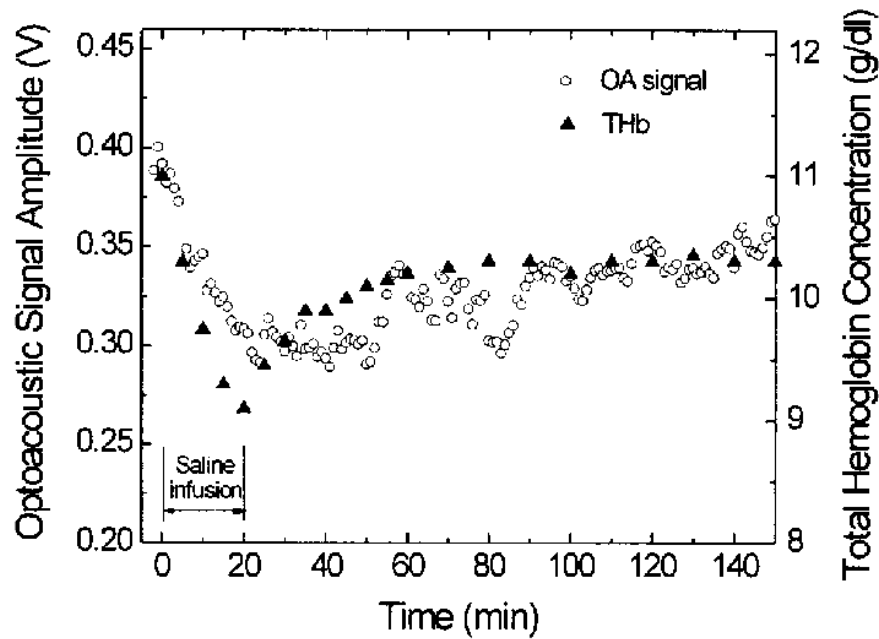


Figure 2-3 Amplitude of the optoacoustic signal measured from the radial artery and actual total haemoglobin concentration during dilution study. [12]

A pulse echo ultrasound method to determine the hematocrit from the Doppler power spectrum is described by *Secomski et al.* [12]. During a six patient *in vivo* study using the Doppler Method the hematocrit was determined from the brachial artery within 5% of the value obtained with an invasive method. The hematocrit determined from the carotid artery was only accurate in a range of 20%.

The problem of the optoacoustic and ultrasound methods for haemoglobin concentration determination is that it is difficult to implement in a practical clinical device.

### 2.3.2 Conductance Methods

Yamakoshi et al. [13] have reported about a method for the non-invasive measurement of hematocrit by means of electrical admittance PG. The principle of this method is based on the evidence that the electrical admittance variation in a finger segment immersed in an electrolyte solution goes to zero when the resistivity of the solution is equal to that of the blood flowing through the segment. The signals

of the total admittance and its pulsatile component in the finger and in the solution were measured by a one or two-channel electrical admittance plethysmography. Two current frequencies were used to avoid an electrical cross-interference within electric circuitries. With this instrument, 48 kHz and 52 kHz of both 2 mA peak to peak constant currents were passed through the segment and the solution, or vice versa via the outer electrodes. Each voltage drop across the inner electrodes is amplified and demodulated to form the impedance signal which was then inverted using a conventional IC divider to yield the admittance signal. Total admittance and its pulsatile variation were obtained using a DC amplifier (high cut-off frequency=0.5 Hz) and an AC amplifier (time constant = 2 s; high cut-off frequency = 40 Hz), respectively. The conductivity of the electrolyte solution can be related to the conductivity of arterial vessels and in turn to the hematocrit. In an *in vitro* blood conductance measurement a correlation to linear regression of  $r = 0.98$  ( $n=16$ ) was exhibited in comparison to a capillary centrifuged reference sample. The group further improved the technique to the level where it could be considered a potentially viable clinical method based on the electrical admittance cuff [14]. This device reported is composed of a rigid annular chamber installed within a surrounding thin-walled tube (cuff), which is filled with electrolyte solution, see Figure 2-4.

With the finger inserted through the cuff, electrical measurements are taken and related to the electrolyte solution conductance in a similar way as is done in the *in vitro* blood conductance measurement.

Difficulties with this kind of technology arise as a result of conductivity measurement, which is prone to variations due to temperature and is furthermore cross-sensitive to intra-, and extra-, cellular water ion content and other blood constituents [15].

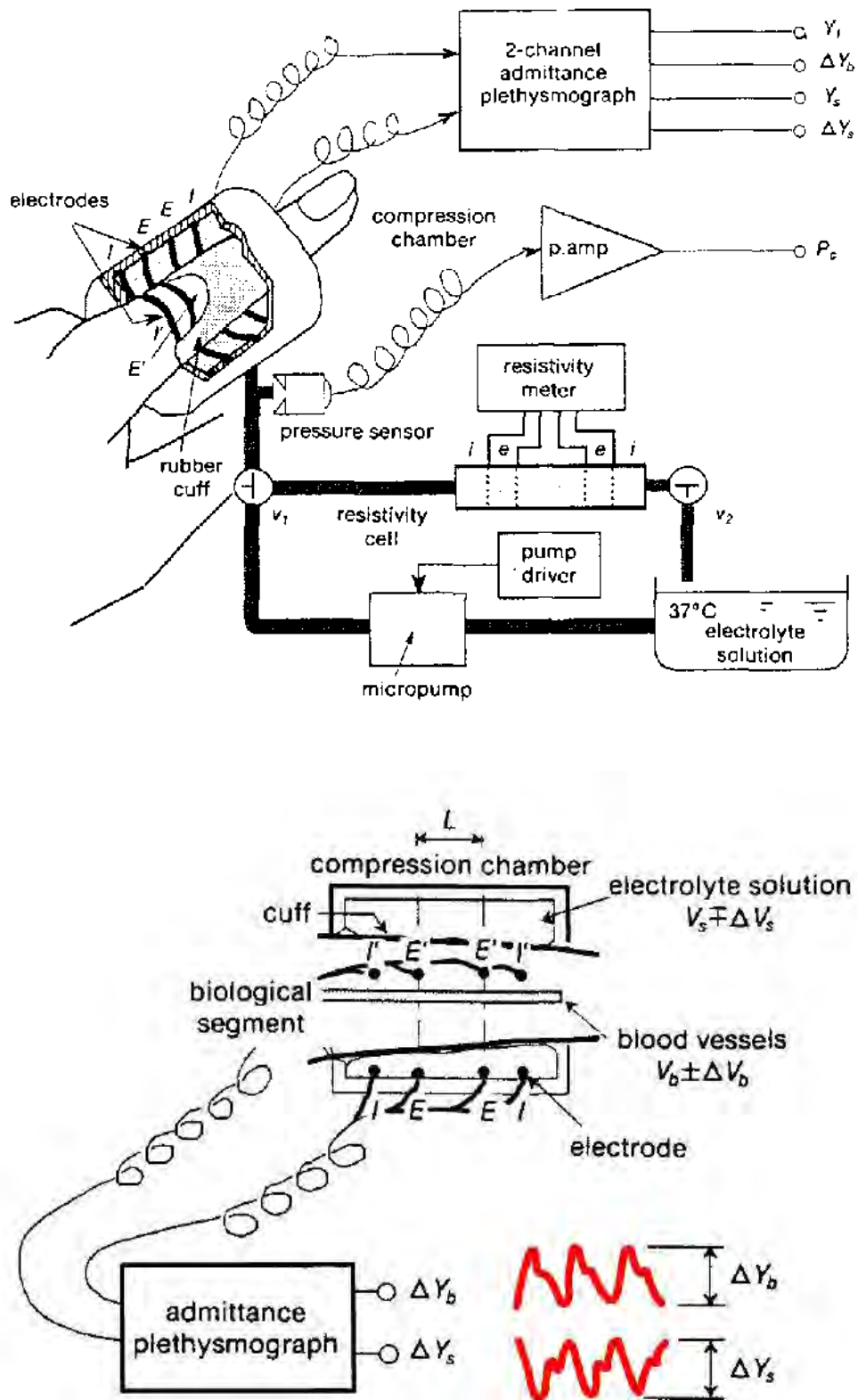


Figure 2-4: Electrical admittance PG by Yamakoshi et al. with a cuff [14]

### 2.3.3 Optical Methods

The key benefits for the use of light to examine biological tissue are that this method facilitates the opportunity for a non-invasive determination of biological parameters, with the elimination of certain potential side effect exhibited by other methods (e.g. corruption of blood samples ), discomfort and other potential risks, such as infection, for the patient. The optical properties of blood in the visible red and near infrared range (NIR) segments of the optical spectrum depend mainly on the oxygenation level of the haemoglobin component [16]. One category of such a device includes the combination near infrared vascular spectrophotometer which can target blood vessels and subsequently estimate the haemoglobin concentration based on the absorption characteristics of individual blood vessels.

Kanashina et al. [17] reported about the correlation between Hb levels determined by the device Astrim Sysmex ([www.sysmex-europe.com](http://www.sysmex-europe.com)) and an automatic cell analyser. Several NIR wavelength bands are simultaneously transmitted through the fingertip and used to visualize veins running close to the surface using a CCD camera as a detector (Figure 2-5) and subsequently calculate the haemoglobin concentration. Incident near-infrared light is transmitted from light sources (LEDs) to a charge-coupled device (CCD) camera, accompanied by absorption and scattering in the human finger. Absorption is due mainly to hemoglobin in blood and scattering to tissue in the finger. The optical image of the transmitted lights taken by the CCD camera can visualize the peripheral blood vessels in the finger. Hemoglobin levels are calculated by examining the optical image of blood vessels in the finger.

A diagnostic sensitivity and specificity of 78.3% and 69% for clinically defined anaemia was reported with a correlation to linear regression of  $r = 0.53$  for anaemic patients. They note that the device is poorly suited to the determination of haemoglobin concentration from a single measurement due to the low accuracy [17].

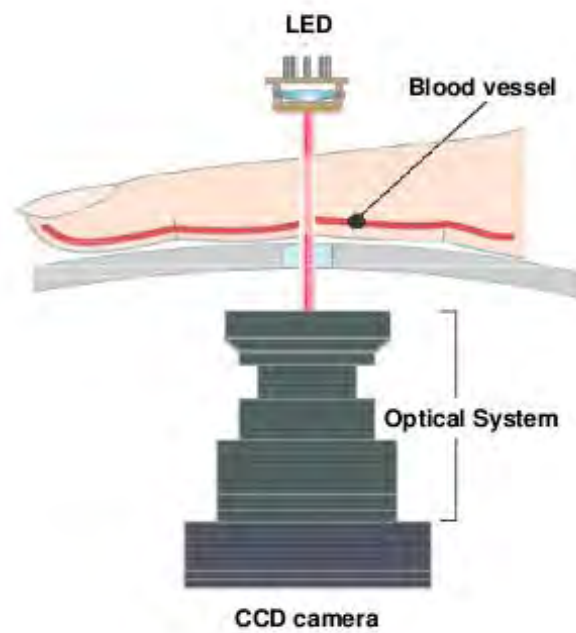


Figure 2-5: Measurement principle of the Astrim Sismex [17]

Another optical method to determine haemoglobin concentration was reported by Jeon et.al [18]. A light source comprising of 5 different wavelength diode emitting arrays is used where are placed at isosbestic points of 525nm, 590nm and 805nm. The group reported a cross validation correlation of  $r = 0.804$  ( $n=97$ ) for a calibration set and relative prediction error of 8.5% ( $n=32$ ) for a prediction set compared to a reference for haemoglobin level obtained using the potassium cyanide method [18]. Nori et al [19] presented a pulse total hemoglobimeter for the non-invasive haemoglobin measurement. Additional to the standard pulse oximeter wavelengths 660nm and 940nm, two additional wavelengths of 805nm and 1300nm were added. The group reported a cross validation correlation of  $r = 0.81$  ( $n=122$ ) for a calibration set compared to a reference haemoglobin measurement obtained with the sodium lauryl sulfate-methaemoglobin method [20].

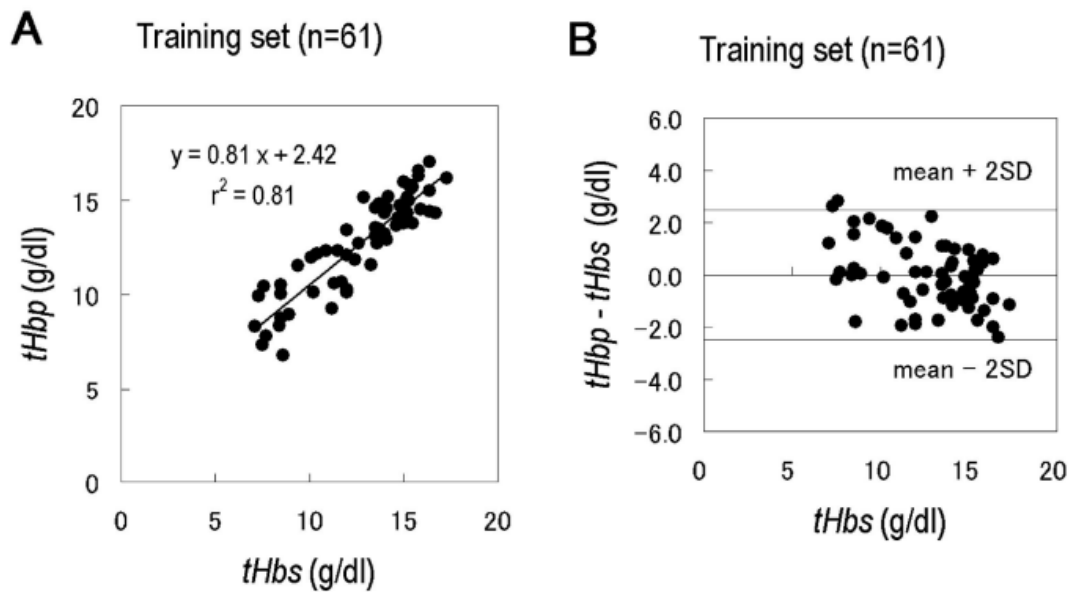


Figure 2-6: Comparison of Non-invasive and Invasive method by Nori et al. [20]

A major application for the device developed by Nori et al. [19] is anemia detection. Anemia is defined as  $<10$  g/dL, and in this case the respective sensitivity and specificity of haemoglobinometer values to detect anemia in patients were 84.3% and 84.6% ( $n = 20$ ). The dependence to a changing  $SpO_2$  level is not disclosed in any literature and the device is not commercially available.

The new instrument Radical-7, from Masimo Corporation, (Irvine, California, USA) allows also a continuous non-invasive measurement of total haemoglobin (Hbt). Few human clinical studies have been undertaken successfully to prove the validity of this device thus far [21]. Neither the mode of operation, nor the number of wavelength used is publically available.

Another commercial available device NBM-200 from Orsense uses a non-invasive optical measurement platform combined with a finger attached ring-shaped sensor probe. The device is shown in figure 2-7. The transmitted optical signal is varied by occluding blood flow with the finger cuff, which is similar to a blood pressure cuff. The result of this occlusion is that the red blood cells are aggregated and after releasing the cuff the red blood cells are allowed to disaggregate. During this process

the optical transmission at multiple wavelengths is monitored [22]. Clinical evaluation of this commercial technology has shown average error values of 0.78 g/dL (n=110) using predefined calibrations for haemoglobin compared to an undisclosed *in vitro* method [23].



Figure 2-7: Orsense NBM-200 [22]

The accuracy of a similar device named called Crit-Scan (Hemametrics, Salt Lake City, [www.hemametrics.com](http://www.hemametrics.com)), which is also equipped with a finger cuff was reported by Miller et al. [24] Miller and colleagues evaluated the efficiency of the device in determining the Hematocrit in 105 males and 93 females. Comparing with readings obtained from intravenous blood simultaneously drawn. The Hct readings gathered via the Crit-Scan had a correlation coefficient of 0.972 and a standard deviation of 1.44. Figure 2-8 shows the device Crit-Scan. The used wavelength used by the device are undisclosed.



Figure 2-8: Crit-Scan from Hemametrics [25]

Murdy et al. [26] report a technique based on the reflectance spectroscopy to analyse the mucosal palpebral conjunctiva (inner lining of the eyelid) as a method of non-invasively monitoring of the total blood haemoglobin concentration. In a nonlinear regression model from diffuse reflectance spectra from the palpebral conjunctiva, a cross-validation correlation of  $r=0.92$  ( $n=30$ ) was obtained for haemoglobin compared to complete blood count testing.

#### **2.4 Summary**

Currently no non-invasive technique has yet been adopted as a standard of care. The reason for the lack of commercial success of such a system includes the complicated nature of the data collection process, the complicated instrumentation needed and accuracy related issues.

A device which enables the possibility to measure the total haemoglobin concentration quickly and noninvasively, with accuracy and precision that is comparable to standard invasive techniques would potentially satisfy several of application areas. Such a non-invasive device would limit the need for painful finger pricks and potentially reduce exposure to blood-borne pathogens.

### 3 Light Transport in Biological Tissue and Turbid Media

#### 3.1 Introduction

This chapter introduces the light transport in biological tissue and turbid media and discusses and describes different models of light propagation.

In order to develop an optical sensor system for the haemoglobin measurement, it is important to establish an understanding of the manner in which light propagates through biological tissue. Figure 3-1 shows schematically some of the transport mechanism of ray propagation diagrams.

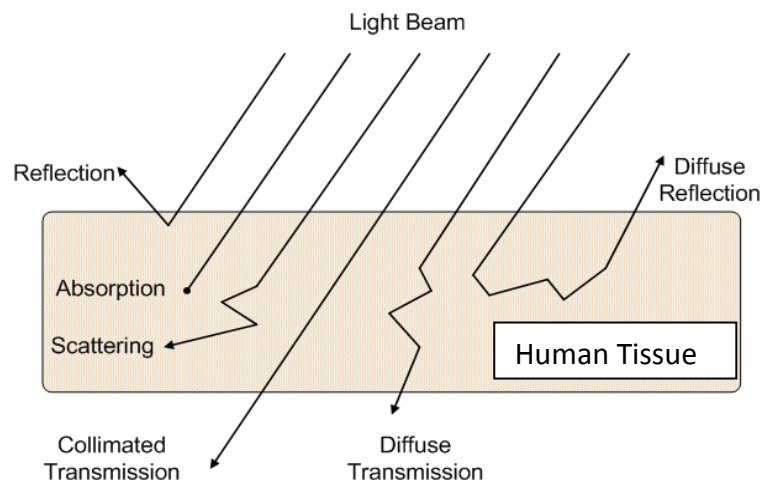


Figure 3-1: Absorption and Scattering in human tissue

During the interaction of light with biological tissue a part of light gets directly reflected at the surface. The ratio of reflected to incident light  $I_R/I_O$  depends on the incident angle  $\vartheta$ , the relative refractive index  $n$  of the first layer of tissue and the polarisation of the incident light (Fresnel Formula). The refractive index  $n$  represents the ratio between the speed of light in vacuum  $c_0$  and the speed of light in the actual medium  $c_n$ .

$$n = \frac{c_0}{c_n} \quad (3.1)$$

In biological tissue such as the human skin typical values for refractive index are in the range from 1.38 to 1.41 [27,28]. The equation that determines the reflectance of parallel (||) or rather perpendicular polarised running light to the surface is given from Bergmann et al. [29]:

$$\left. \begin{aligned} R_{\parallel} &= (I_R/I_O)_{\parallel}^2 = \left[ \frac{n^2 \cos \vartheta - \sqrt{n^2 - \sin^2 \vartheta}}{n^2 \cos \vartheta + \sqrt{n^2 - \sin^2 \vartheta}} \right]^2 \\ R_{\perp} &= (I_R/I_O)_{\perp}^2 = \left[ \frac{\sqrt{n^2 - \sin^2 \vartheta} - \cos \vartheta}{n^2 - 1} \right]^2 \end{aligned} \right\} \quad (3.2)$$

According to Snell's law photons which penetrate the tissue are refracted at the air/skin surface boundary. Depending on the probe geometry the received light intensity can be diffuse reflected or transmitted. The ratio of the diffuse reflection or transmitted intensity to the source intensity is called *diffuse reflection*  $R_{\text{diff}}$  or *diffuse transmission*  $T_{\text{diff}}$ . These components of the light transport are show in figure 3-1. The part of the incident light that leaves the probe in the propagation direction is referred to as collimated transmission  $T_{\text{coll}}$  and the summation of the collimated and diffuse transmission is the total transmission  $T_{\text{tot}}$ . Photons which leave the tissue without interaction (ballistic photons) or finally leave in propagation direction after scattering are responsible for the collimated transmission. Inside the tissue the photons can be scattered or absorbed. With increasing path length the probability for such an event develops exponentially.

### 3.2 Light Absorption

When light radiation is incident on matter composed of discrete electrical charges, the charges are forced to oscillate at the frequency of the incident electric field. During the interaction of light with matter, resonance occurs whereby energy is

transferred from the incident electric field to the matter and the amplitude of vibration of the matter e.g. molecules and atoms (including electrons) is greatly increased. The atoms or molecules will usually lose their energy by colliding with one another and thereby impart kinetic energy to other neighbouring. Hence, the energy associated with the incident field is most often dissipated as heat within the medium. This process is known as absorption [31].

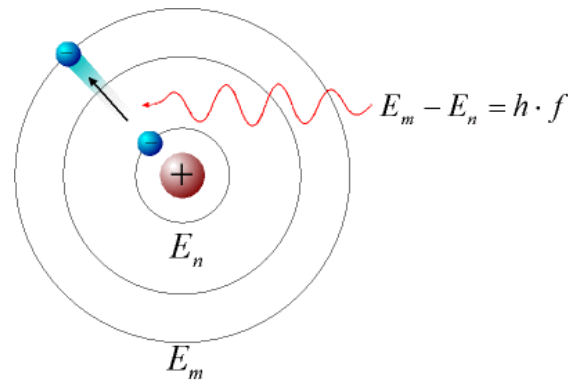


Figure 3-2: Absorption of a Photon and Excitation of the Atom

The overall effect of the absorption is a reduction in the intensity of the light beam traversing the medium. [31,32] A relationship between the absorption of light in a purely absorbing medium and the thickness of the medium is fundamentally described by the Beer-Lambert law, where  $I_0$  and  $I$  are the incident and transmitted light,  $\mu_a$  ( $\text{mm}^{-1}$ ) is the absorption coefficient and  $d$  (mm) the optical path length along the medium.

$$I = I_0 e^{-\mu_a d} \quad (3.3)$$

The absorption coefficient  $\mu_a$  can be interpreted as the probability that a photon will be absorbed by the medium per unit length. The inverse of  $\mu_a$ ,  $1/\mu_a$  can be taken to be the absorption length, i.e. the distance the light has to travel in order to be attenuated by a factor of  $1/e$ . The effectiveness of a material as an absorber is given by its extinction coefficient  $\epsilon$  ( $\text{mm}^{-1}\text{Molar}^{-1}$ ). This is equal to its absorption coefficient

per unit of concentration in Molar. The absorption coefficient for a single at a given concentration  $c$  is given by:

$$\mu_a = \varepsilon * c \quad (3.4)$$

The Beer-Lambert's law is also valid if more than one absorbing substance is present. Each absorber contributes in part to the total absorbance. The unscattered absorbance  $A$  is defined as the negative natural logarithm of the transmittance (ratio  $I$  to  $I_0$ ) of light. The resulting total absorbance  $A_t$  of a medium with  $n$  absorbing substances is given as:

$$A_t = \sum_{i=1}^n \varepsilon_i(\lambda) c_i d_i \quad (3.5)$$

The Beer-Lambert law is only valid under certain limited conditions: the light entering the medium must be monochromatic and perfectly collimated, and the medium itself must be purely and uniformly absorbing.

### 3.3 Light Scattering

When a photon interacts with a particle, one of the possible outcomes is that the direction of propagation of the photon will change. This type of interaction is called scattering. As a result of scattering, the velocity of light in all matter is less than in vacuum and the incident radiation will be scattered in all directions. The phase difference of the scattered light relative to the primary wave depends on the frequency of the primary wave. In any direction the total scattered field is then a superposition of all the scattered wavelets propagating in that direction. The scattered waves interfere with the incident wave, modifying its phase and the velocity of the light through the medium. The most important form of light scattering in the near infrared region is elastic scattering where no energy loss occurs during the scattering process [31,32]. An analogous quantity to the absorption coefficient

$\mu_a$  namely the scattering coefficient  $\mu_s$  is introduced. By definition  $\mu_s$  represents the probability that a photon will be scattered per unit length.

The total attenuation coefficient  $\mu_t$  is given by

$$\mu_t = \mu_a + \mu_s \quad (3.6)$$

According to this, equation 2.7 is a modified form of equation 2.3 and can be written as:

$$I = I_0 e^{-\mu_t d} \quad (3.7)$$

The ratio of the scattering coefficient to the total attenuation coefficient is defined as Albedo  $a$ , which represents the ratio of scattering in comparison to the absorption in the tissue:

$$a = \frac{\mu_s}{\mu_a + \mu_s} \quad (3.8)$$

In case  $a = 0$  the tissue absorbs the whole incident light and if  $a = 1$  all light attenuation is due to scattering. A typical value for biological tissue is  $a = 0.93$  [33] and this shows the dominance of scattering.

Unlike the absorption only case, a description of the entire scattering process using only the scattering coefficient is insufficient.

A photon which encounters a scattering particle within a homogeneous medium is diverted and changes propagation path in any direction. The possibility that a photon is scattered from travelling direction  $\vec{s}$  into the new direction  $\vec{s}'$  specifies the scattering function  $P(\vec{s}, \vec{s}')$ . The scattering direction of the photon is defined by the scattering angle  $\theta$ , the angle between the incident and the scattered directions, and the azimuth angle  $\varphi$ . Integrating the scattering function over the full solid angle  $\Omega$  is given as result of unity i.e. the probability of the light being scattered in any direction is unity.

$$\int_{4\pi} P(\vec{s}, \vec{s}') d\Omega = 1 \quad (3.9)$$

The mean cosine  $g$  of the scattering angle  $\theta$  is known as the anisotropy factor and can take values from minus one to plus one.

$$g = \cos\theta = \int_{4\pi} (\vec{s}, \vec{s}') P(\vec{s}, \vec{s}') d\Omega = \frac{\int_0^{2\pi} d\phi \int_0^\pi \cos\theta P(\theta) d(\cos\theta)}{\int_0^\pi P(\theta) d(\cos\theta)} \quad (3.10)$$

In case of  $g > 0$  the scattering direction is predominantly forward and if  $g < 0$  the scattering is predominantly backward. If  $P$  is equal for all solid angles the scattering is isotropic (or Rayleigh scattering) and  $g$  will be equal to zero. These cases are illustrated in figure 3-3. In biological tissue the preferential scattering direction is forward orientated and the anisotropy factor  $g$  can be assumed as constant for most tissues. An often used constant values for  $g$  is approximately 0.9. [34]

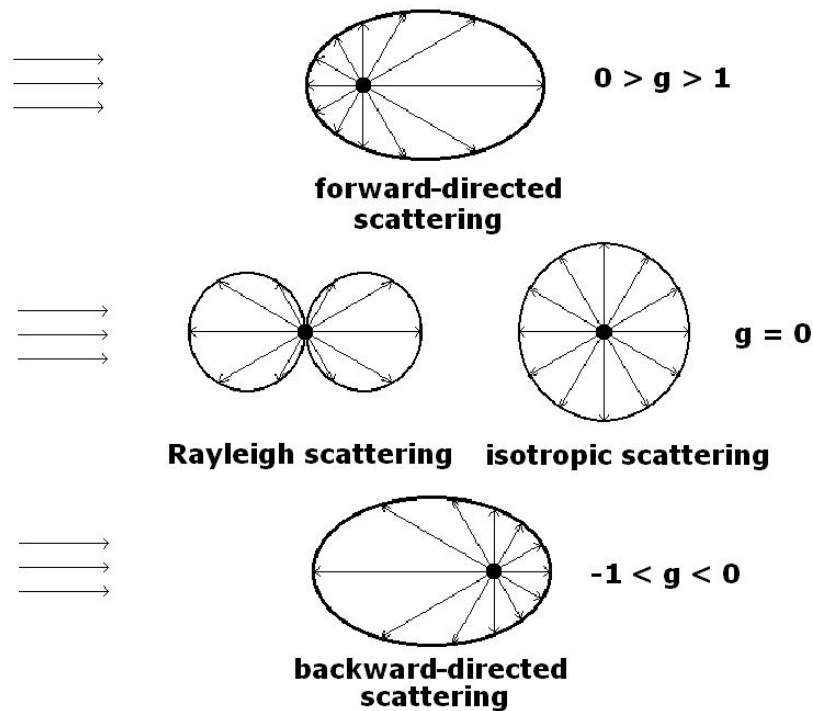


Figure 3-3: Anisotropy factor  $g$  and the resulting direction of scattering

An exact scattering phase function for human tissue is unknown due to the unknown composition of particles causing the scattering. There are many approximations, but the Henyey-Greenstein phase function is the most widely used [35, 36]:

$$p(\theta) = \frac{1}{4\pi} \frac{1 - g^2}{\sqrt{(1 + g^2 - 2g \cos \theta)^3}} \quad (3.11)$$

The Henyey-Greenstein phase function does not depend on the azimuth angle  $\varphi$ . Another often used optical parameter results by combining the scattering coefficient and the anisotropy factor giving the transport scattering coefficient  $\mu_s'$

$$\mu_s' = (1 - g)\mu_s \quad (3.12)$$

The parameter  $\mu_s$ ,  $\mu_a$  and  $g$  are often referred to as optical constants but they are dependent on the wavelength. Due to this property a wide variation in the effects on monochromatic light propagation in biological tissue is observed.

The human skin consists of around 80% of water. Therefore the absorption coefficient of water is highly relevant during the interaction between light and tissue. In the mid and far infrared spectral range (5.6  $\mu m$  - 1000  $\mu m$ ) the water absorption dominates in the biological tissue while in some windows within the visible (380nm - 750nm) up to the near infrared (950nm) spectral range the absorption of water is small. In the range from 600nm to 950nm the blood pigment haemoglobin is the strongest absorber. This area where the penetration depth of photons is highest (the longer the wavelength the greater the penetration depth) is called the optical or therapeutic window. The water absorption and the highlighted therapeutic window are show in Figure 3-4.

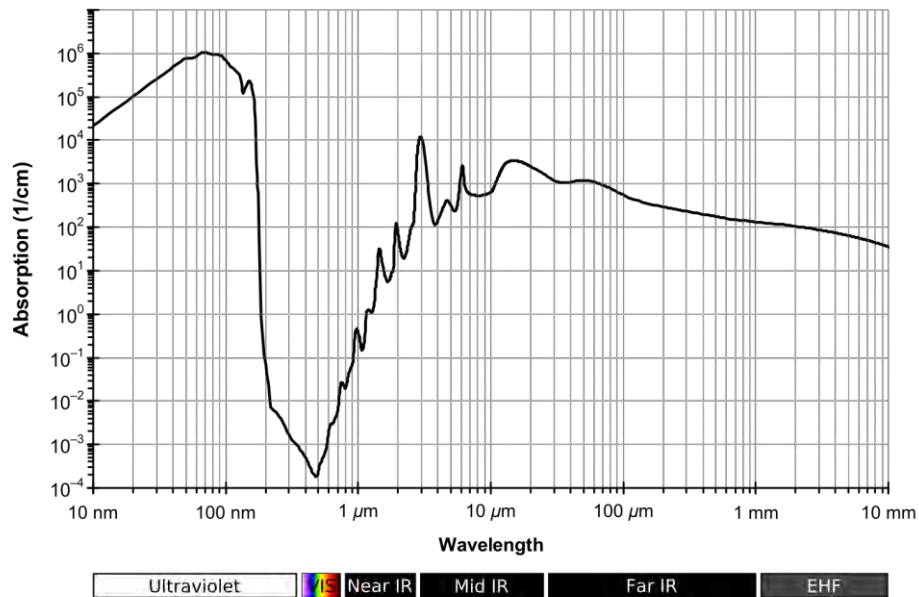


Figure 3-4: The water absorption spectra [91]

Depending on the relation of the wavelength to the dimension the scattering mechanism can be split into Rayleigh and Mie scattering. For spherical particles that are small compared to the wavelength ( $r \ll \lambda$ ), the theory of Rayleigh scattering can be applied. The incident light stimulates the scattering particle to induce a dipole scattering. The intensity,  $I$  of the scattered light wave depends on the squared cosine of the scattering angle  $\vartheta$  and the fourth power of the wavelength [31].

$$I \sim \frac{1 + \cos^2 \vartheta}{\lambda^4} \quad (3.13)$$

Due to the wavelength dependence the Rayleigh scattering, this is the predominant scattering mechanism for short wave radiation such as visible blue and ultraviolet radiation.

For particles that are similar in dimension to the wavelength of the incident light ( $0,1 \lambda < r < 10 \lambda$ ) the Mie theory can be applied.

### 3.4 Models of Light Propagation in Turbid Media

The name turbid media is used for materials whose light propagation is characterized by both scattering and absorption. In the following section two different models for the description of the light propagation in turbid media are introduced.

Based on Maxwell's equations the Mie Theory (3.3.1) describes the light propagation of an electromagnetic wave in a medium containing scattering spheres. Using an analytic method based on Maxwell's equations for a complex structure such as biological tissue is problematical. In this case a phenomenological approach to describe the light propagation can be substituted, one such method is the Radiative Transfer Theory (3.3.2) which reduces the scattering and absorption mechanism to a heuristic approach for the photon transport. Analytical solutions of the Radiative Transport Theory are only possible for simple geometries and in the case of a complex structure or boundary value problem an approximation method as the Diffusion Approximation (3.3.2.1) has to be introduced. To solve the radiative transfer theory, stochastic approaches as the Monte Carlo Method (3.3.3) can be used to describe the interaction of photons and scattering media.

#### 3.4.1 Mie Theory

Mie's Theory commences by considering an electromagnetic wave which propagates in a medium with a refractive index of  $n_1$ . Furthermore, the medium contains spherical particles with refractive index  $n_2$ . Based on the Maxwell's equations for the electrical and magnetic field components  $\vec{E}$  and  $\vec{D}$  and respectively  $\vec{B}$  and  $\vec{H}$  it is feasible to develop a differential equation based on spherical coordinated for the angle and radial proportion.[37, 38] The solutions for the radial part show that they depend only on the ratio of the circumference to the wavelength in the current media. For this reason it is practical to introduce the Mie Parameter  $\alpha$  and  $\beta$ .

$$\alpha = \frac{2\pi r}{\lambda} = \frac{2\pi n_1 r}{\lambda_0} \quad (3.14)$$

$$\beta = \frac{2\pi n_2 r}{\lambda_0} = \frac{n_2}{n_1} \alpha \quad (3.15)$$

r: sphere radius

$\lambda_0$ : wavelength in vacuum

The cross section for the scattering  $\sigma_{sca}$  and the extinction which is the sum of scattering and absorption  $\sigma_{ext} = \sigma_{sca} + \sigma_{abs}$  can be calculated with the help of the transition conditions. Thereby the transition conditions premise the continuity of the normal components  $\vec{B}$  and  $\vec{H}$  as soon as the tangential components  $\vec{E}$  and  $\vec{D}$  on the surface of the sphere [39]. The cross section in the MIE Theory is often replaced with the efficiency factor Q which represents the ratio of cross section to the geometrical shadow area  $\pi r^2$  of the particle [40].

$$Q_{sca} = \frac{\sigma_{sca}}{\pi r^2} = \frac{2}{\alpha^2} \sum_{k=0}^{\infty} (2k+1) [|a_k|^2 + |b_k|^2] \quad (3.16)$$

$$Q_{ext} = \frac{\sigma_{ext}}{\pi r^2} = \frac{2}{\alpha^2} \sum_{k=0}^{\infty} (2k+1) \text{Re}\{a_k + b_k\} \quad (3.17)$$

$$Q_{abs} = Q_{ext} - Q_{sca} \quad (3.18)$$

The coefficients  $a_k$  and  $b_k$  are given by:

$$\left. \begin{aligned} a_k &= \frac{\psi_k(\alpha)\psi'_k(\beta) - m\psi_k(\alpha)\psi'_k(\beta)}{\xi_k(\alpha)\xi'_k(\beta) - m\xi_k(\alpha)\xi'_k(\beta)} \\ b_k &= \frac{m\psi_k(\alpha)\psi'_k(\beta) - \psi_k(\alpha)\psi'_k(\beta)}{m\xi_k(\alpha)\xi'_k(\beta) - \xi_k(\alpha)\xi'_k(\beta)} \end{aligned} \right\} \quad (3.19)$$

The function  $\psi_k(x)$  and  $\xi_k(x)$  can be defined by the Ricatti-Bessel functions of the first and second kind [41] and the  $k$  is the wave number.

$$\left. \begin{aligned} \psi_k(x) &= \sqrt{\frac{\pi x}{2}} J_{k+\frac{1}{2}}(x) \\ \xi_k(x) &= \sqrt{\frac{\pi x}{2}} H_{k+\frac{1}{2}}(x) \end{aligned} \right\} \quad (3.20)$$

It is only possible to calculate the efficiency coefficients of scattering and absorption where the anisotropy factor different calculation programs and methods are known [42]. In the case of small scattering radii ( $\alpha \ll 1$ ) Rayleigh scattering occurs and the solution for the anisotropy results in  $g \approx 0$ . If a media contains a great many of Mie scatters multiple scattering will take place. Each scattering event can be considered as independent if distance between the scatterers is clearly larger than wavelength of the incident light. Under these terms the scattering and absorption coefficient (section 3.1 and 3.2) of the media can be calculated from the particle cross-section  $\sigma$  and particle density  $\rho$ .

$$\mu_s = \sigma_s \rho \quad (3.21)$$

$$\mu_a = \sigma_a \rho \quad (3.22)$$

The accuracy of the Mie Theory is limited if the particle shape and size is not uniform or the reflectance index of the media is not homogeneous. Also if the definition of the scattering particles inside the media is unknown as in biological tissue, another approach must be chosen. This is available in the Radiative Transfer Theory which is described in the following section.

### 3.4.2 The Radiative Transfer Theory

The Radiative Transfer Theory (RTT) is the description of the energy transport through a medium which contains scattering and absorbing particles. The RTT uses a phenomenological approach and the most important requirements for the validity of the RTT are:

- Homogeneity of the medium
- Independence of the individual scattering processes among each other
- Uniform scattering characteristic of the scattering particles

The scalar form of the RTT which is described here ignores effects depending on polarisation as well as diffraction during the interaction between the photons and the scattering medium. An inclusion of the polarisation is possible but results in significant higher mathematical effort and is not considered necessary or justifiable in this thesis as polarisation effects are negligible.

The basic equation of the RTT was developed 1950 from the Indian physicist Chandrasekhar [43] in order to describe light passage through the atmosphere. To derive the RTT a specific spectral radiance  $L(\vec{r}, \vec{s})$  is assumed which is propagating the direction of the unit vector  $\vec{s}$ . A differential small part of the incident radiation will pass through a cylindrical portion in the volume  $dV$  with the Ground area  $G$  and the differential small height  $dx$ . This is shown in Figure 3-5.

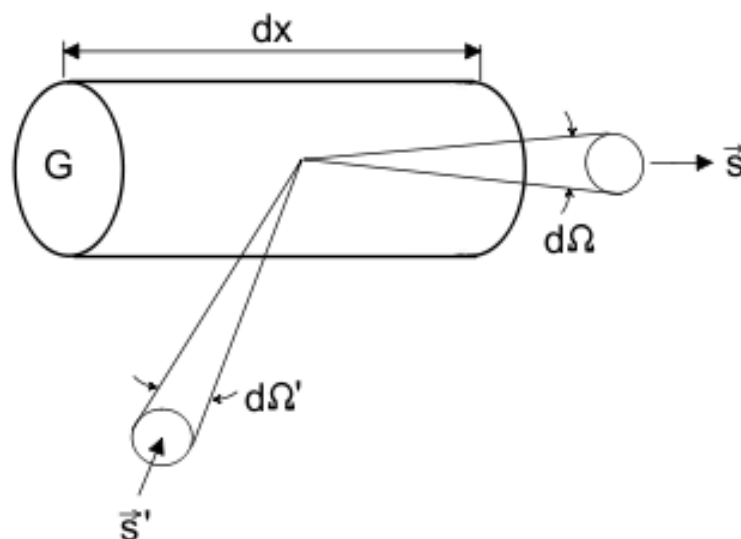


Figure 3-5: Intensity scattering in a cylindrical portion in the volume

In the case that the volume  $Gdx$  includes a number of  $\rho Gdx$  scattering particles ( $\rho$  is particle density) every particle absorbs and scatters a part  $\sigma_a L$  and  $\sigma_s L$  of the

incident light intensity depending on the respective cross section  $\sigma_a$  and  $\sigma_s$  of the particle. The reduction of the radiance  $dL(\vec{r}, \vec{s})$  in the direction  $\vec{s}$  in the volume  $Gdx$  can be expressed as:

$$dL(\vec{r}, \vec{s}) = -dx\rho(\sigma_a + \sigma_s)L(\vec{r}, \vec{s}) \quad (3.23)$$

Simultaneously the radiance in direction  $\vec{s}$  is rising caused by the part of the radiance  $L(\vec{r}, \vec{s})$  originating from other directions  $\vec{s}'$  which have been scattered into the direction  $\vec{s}$  within the observed volume. The additional radiance  $L(\vec{r}, \vec{s})$  which interacts with a particle in the volume  $Gdx$  arriving from the solid angle  $d\Omega'$  is given as  $L(\vec{r}, \vec{s}')d\Omega'$ . The scattered radiance by the particle is  $L(\vec{r}, \vec{s}')d\Omega'\sigma_s$ .

The additional scattered radiance in the volume  $GdX$  into the direction  $\vec{s}$  results in the scattering function (integral above full solid angel ( $4\pi$ )):

$$\int_{4\pi} \rho\sigma_s dx P(\vec{s}, \vec{s}')L(\vec{r}, \vec{s}') d\Omega' \quad (3.24)$$

The classic expression of the RTT results from the summation of equations 3.23 and 3.24:

$$\frac{dL(\vec{r}, \vec{s})}{dx} = -\rho(\sigma_a + \sigma_s)L(\vec{r}, \vec{s}) + \rho\sigma_s \int_{4\pi} P(\vec{s}, \vec{s}')L(\vec{r}, \vec{s}') d\Omega' \quad (3.25)$$

By combining with the Equations 3.21 and 3.2 for the absorption and scattering coefficient the RTT results in the Radiative Transfer Equation (RTE):

$$(\vec{s} \nabla)L(\vec{r}, \vec{s}) = -(\mu_a + \mu_s)L(\vec{r}, \vec{s}) + \mu_s \int_{4\pi} P(\vec{s}, \vec{s}')L(\vec{r}, \vec{s}') d\Omega' \quad (3.26)$$

The first term on the right hand side describes the attenuation of the primary beam caused by absorption and scattering and the second term represents the increase of the intensity by light from other solid angles that get scattered into the observed propagation direction. In the case of a non-scattering media ( $\mu_s = 0$ ) the RTT will be reduced to the Beer-Lambert law (equation 3.3) with  $\vec{s} = (1,0,0)$  :

$$\frac{dL(\vec{x})}{dx} = -\mu_a L(\vec{x}) \rightarrow L(\vec{x}) = L_0 e^{-\mu_a x} \quad (3.27)$$

In the case  $\mu_s \neq 0$  an exact solution of the RTT for any geometric and boundary values it has not been possible to obtain. This is due to the complexity of the geometry and therefore a reasonable approximation is necessary. A common approximation for biological tissue is the Diffusion Approximation which is described in the next section.

### 3.4.2.1 Diffusion approximation

The assumptions made in the Diffusion Approximation (DA) are that the source is an isotropic point source and scattering within the medium is approximately isotropic[44]. The radiance  $L(\vec{r}, \vec{s}, t)$  will be split into a diffuse and a collimated part  $L_{\text{diff}}$  and  $L_{\text{coll}}$ :

$$L(\vec{r}, \vec{s}, t) = L_{\text{coll}}(\vec{r}, \vec{s}, t) + L_{\text{diff}}(\vec{r}, \vec{s}, t) \quad (3.28)$$

The collimated part contains the unscattered light and follows the Beer-Lambert Law. The photons moving into the direction of the incident light beam after multiple scattering processes are ignored. Based on the Radiative Transfer Equation the function for the diffuse part of the radiation is approximated by the two first terms of a Taylor series:

$$L_{\text{diff}}(\vec{r}, \vec{s}, t) = \frac{1}{4\pi} U(\vec{r}, t) + \frac{3}{4\pi} \vec{j}(\vec{r}, t) \vec{s} \quad (3.29)$$

$$\text{with } U(\vec{r}, \vec{s}, t) = \int_{4\pi} L(\vec{r}, \vec{s}, t) d\Omega \quad \text{and} \quad \vec{j}(\vec{r}, t) = \int_{4\pi} L(\vec{r}, \vec{s}, t) \vec{s} d\Omega \quad (3.30)$$

The diffuse flow  $U(\vec{r}, t)$  in equation 3.29 represents the isotropic part and the diffuse flux density vector  $\vec{j}(\vec{r}, t)$  the weak orientated anisotropic part of the diffuse radiance (FIG 3-6).

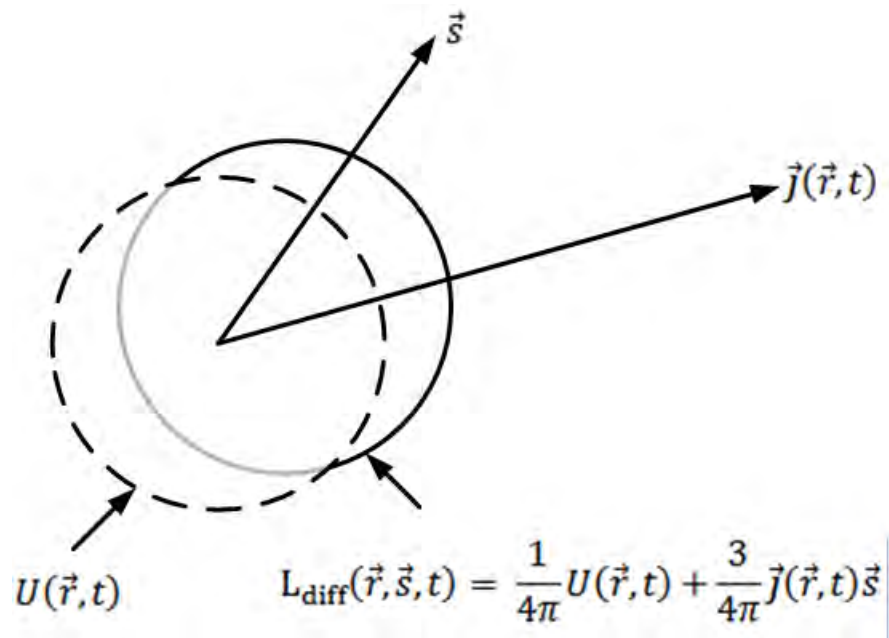


Figure 3-6: Illustration of the diffuse radiance in the diffuse approximation

After integrating the function over the full solid angle the radiance transfer equation can be reduced to a time-dependent diffusion equation for the diffuse flux  $U(\vec{r}, t)$ .

$$\left( \frac{1}{c_n} \frac{\partial}{\partial t} - D \nabla^2 + \mu_a \right) U(\vec{r}, t) = S(\vec{r}, t) \quad (3.31)$$

Diffusion coefficient:

$$D = \frac{1}{3(\mu_a + 1 - g)\mu_s} \quad (3.32)$$

Source energy density:

$$S(\vec{r}, t) = \int_{4\pi} Q(\vec{r}, \vec{s}, t) d\Omega \quad (3.33)$$

Using the diffuse approximation solely, it is necessary to know the absorption coefficient  $\mu_a$  and the reduced scattering coefficient  $\mu_s' = \mu_s(1 - g)$  for the description of the light propagation.

The reduced scattering coefficient describes that forward orientated (e.g.  $\mu_s = 10\text{mm}^{-1}$ ,  $g=0,9 \rightarrow \mu_s' = 10\text{mm}^{-1}$ ) and weak isotropic scattering (e.g.  $\mu_s = 1\text{mm}^{-1}$ ,  $g=0 \rightarrow \mu_s' = 1\text{mm}^{-1}$ ) provide the same diffuse light distribution after a number of scattering events. In the literature several publications can be found which describe the limitation of the diffuse approximation [45, 46]. Another mandatory criterion for the validity of this approximation is that light distribution can only be considered in a distance of ten transport path lengths  $1/\mu_s'$  from the light source [47]. The reduced scattering coefficient for biological tissue is best suited to a value of  $1\text{mm}^{-1}$  and the distance between the light source and the receiver in case of the used finger clip is above one centimetre. For this reason the diffuse approximation is feasible to describe the light propagation in the finger terminal element. The expected absorption within the finger tissue describes an exponential behaviour in dependency to a function  $f(\mu_a, \mu_s')$ . This function is unknown and the reduced scattering as well as the absorption coefficient is hard to determine experimentally. For this reason a calibration procedure with simultaneously obtained in-vivo measurement values is indispensable and forms an integral part of this investigation.

### 3.4.3 The Monte Carlo Method Applied to Radiative Transfer

The Monte Carlo Method is based on the radiative transfer equation and involves computer simulated calculations of photon propagation in scattering media. The photons are treated as particles and wave characteristics as well as polarisation states nature are ignored. In a Monte Carlo simulation photons are injected into the medium and their path is traced until they are either absorbed or permanently scattered out of the region of interest [48, 49]. The statistic uncertainty is proportional to  $1/\sqrt{N}$  where  $N$  is the number of photons. The rules of photon propagation are expressed as probability distributions which are based on the

geometry and optical properties of the medium. The Monte Carlo simulation consists of three steps

- Photon generation
- Simulation through the tissue (random walk) and
- Photon detection at regions of interest

The computational time depends on the number of photons. While values for diffuse reflectance demand a few thousand photons, a complete three-dimensionally spatial distribution of photons may demand several hundred thousand or millions of photons. In basic situations photons are launched as a collimated beam perpendicular to the tissue surface. Further steps in the simulation process depend on the statistical sampling of the probability distributions for step size and angular deflection per scattering event. The probability of photon being absorbed or scattered while it propagates in the tissue is related to the absorption and scattering coefficient. The photon step size through the medium is expressed as the probability  $\xi$  ( $0 \leq \xi \leq 1$ ) that a photon propagates a distance  $L$  without being scattered or absorbed. Due to the exponential decrease of intensity with increasing distance into the medium, the Beer-Lambert can be expressed as:

$$L = -\frac{\ln(\xi)}{\mu_a + \mu_s} \quad (3.34)$$

Every photon in the simulation starts with an initial weight and direction, determined by functions whose arguments are randomized numbers. During the propagation of the photon the weight and direction are adjusted in every step until the photon is absorbed or leaves the medium. The advantage of the Monte Carlo Method is that there exist no limitations with regard to the geometries of the probe, boundary conditions or the assembly of the light source and detector. It is possible to simulate every experimental configuration and the only limiting factor is the calculation time.

### 3.5 Measurement of optical properties

The optical parameter ( $\mu_a, \mu_s$ ) for turbid media are not directly measurable and for this reason diffused light spectrometers are used to receive the diffuse reflected and transmitted light of a probe. By choosing one adequate model for the light distribution inside the probed volume of tissue the optical constants can be inverse calculated by one of the above described methods. The most important diffused light spectrometer is the Ulbricht Sphere and the Goniophotometer.

The Ulbricht sphere, also known as integrating sphere, is a spherical hollow cavity with a highly reflective non-absorbing surface [51] and is shown on Figure 3-7. The diffuse transmitted or reflected scattered light intensity is measured using a detector is mounted on a selected output port. The integrating sphere is used for measuring the output power of a light source and due to the set up the propagation characteristics of the light source which has no influence of the measurement. To determine the sphere coefficients an initial calibration measurement has to be carried out. To calculate the optical properties  $\mu_a$  and  $\mu_s'$  the diffuse reflectance and diffuse transmittance of the sample have to be determined. The measurement can be done in two steps using a single sphere (figure 3-7) or in one step using a dual sphere (figure 3-8).

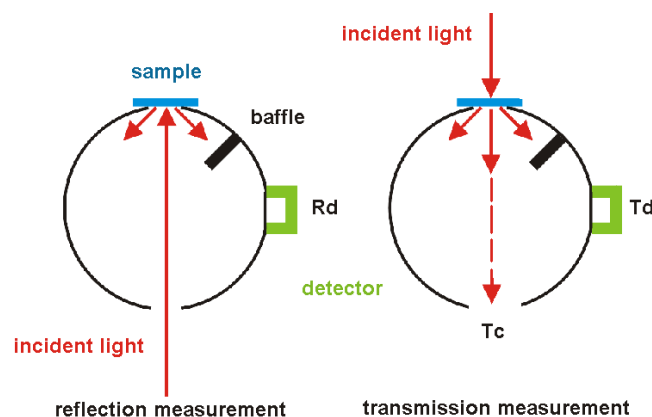


Figure 3-7: Ulbricht Sphere Single measurement [50]

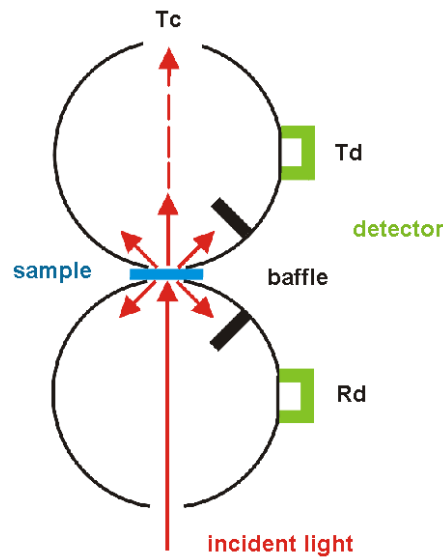


Figure 3-8: Ulbricht Sphere Dual Setup [50]

The advantage of the dual sphere setup is its capability to simultaneously measure the reflection and transmission which does not require a movement of the probe. A disadvantage is the necessity to use thin optical samples through which light exchanges between the spheres can occur. That would result in a distortion of the results and necessitate a complex calibration [48].

The collimated light source of the goniophotometer illuminated the sample located in the centre through a pinhole. A photomultiplier (PM) describes a circle around the fixed sample. Thereby the reflected and transmitted scattered lights are detected and are angle dependent.

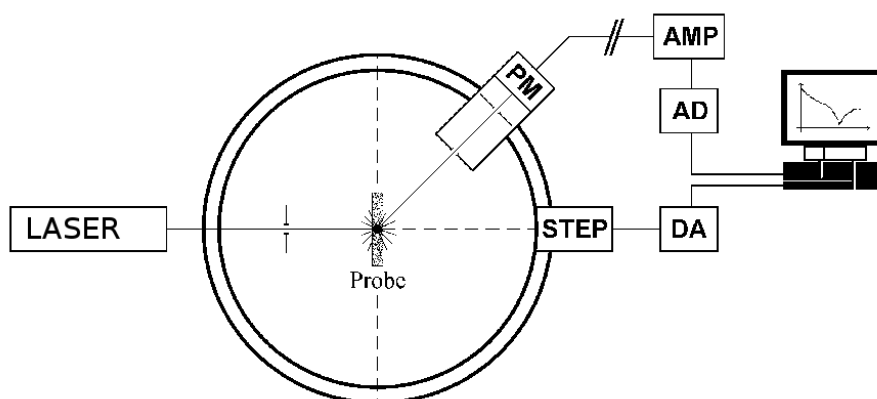


Figure 3-9: Schematic Goniophotometer

To reduce the reflection loss and reduction of the critical angle of the total reflection on the glass-air boundary it is possible to measurement in a water filled acrylic glass cell. With known sample geometry a Monte Carlo simulation with the measured photon allocation it is possible to draw conclusions of the single scattering processes and hence deduce the phase function and the anisotropy [49].

The Ulbricht sphere spectroscopy in combination with the inverse Monte Carlo algorithm is actually the gold standard. Nevertheless the measurement of scattering and absorption in turbid media is complicated [50, 52]. However the most significant disadvantage of the Ulbricht sphere spectroscopy is that the method can be only used *in vitro*.

## 4 Human physiology

### 4.1 Introduction

To develop a measurement method for the non-invasive haemoglobin determination it is essential to understand the mechanism of the signal formation and the interaction of light and tissue. In this chapter the physiological basics are described and discussed.

### 4.2 Blood

Blood is the human body's fluid transport medium which has to fulfil multiple tasks as a means of transport system or for heat balancing and a physiological protection system. It consists of cellular components and blood plasma as an intravascular fluid. The plasma is around 90% by volume water and contains dissolved proteins, glucose, clotting factors, mineral ions, hormones and carbon dioxide. The absorption properties in the red and near infrared range are similar to absorption of water [53, 54]. The blood cells are the erythrocytes (red blood cells), leucocytes (white blood cells) and the thrombocytes (platelets) which evolve from pluripotent stem cells of the bone marrow. Figure 4-1 shows a blood bag of erythrocytes concentrate and blood plasma. The blood looks red due to the iron and the blood plasma is yellow due to the proteins. The amount of blood is around 6-8 % of the body weight of a male human which corresponds to 4-6 litres. The blood plasma makes up about 55% of the total blood volume.



Figure 4-1: Erythrocytes Concentrate (red, left) and Blood Plasma (yellow, right) in 250ml blood bags

### 4.2.1 Red Blood Cells and Haemoglobin

Haemoglobin is carried in the erythrocytes, or red blood cells, and constitutes about 40-45% of the whole blood. The main function of the red blood cells is to carry the oxygen to the tissue and to return the carbon dioxide from the tissue to the lungs. Each red blood cell contains about 640million haemoglobin molecules. Haemoglobin consists of the protein globin bound to four haem groups. Each haem group contains an iron atom at the centre of a ring structure. An iron ion  $Fe^{2+}$  is able to covalently bind to an oxygen molecule in order to become oxygenated. One haemoglobin molecule with its four iron centres can carry a total of four molecules of oxygen, as shown in Figure 4-2.

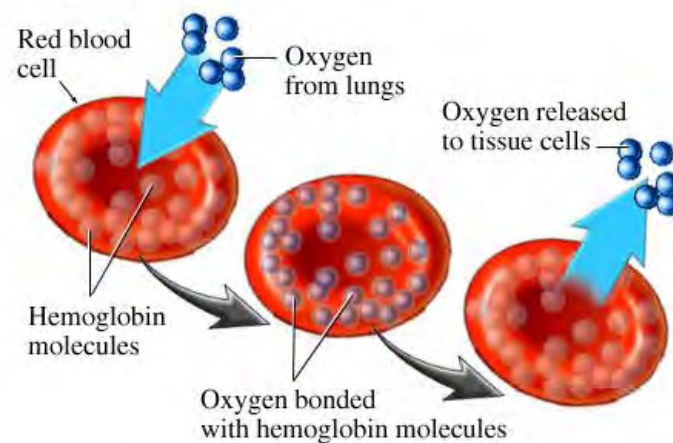


Figure 4-2: Oxygen transport by haemoglobin [94]

In its oxygenated state haemoglobin is known as oxyhaemoglobin ( $HbO_2$ ) and the deoxygenated form is known as deoxyhaemoglobin (HHb). In case that  $Fe^{2+}$  is oxidised to  $Fe^{3+}$  the haem group is called methaemoglobin which is not available for the oxygen transport [55, 56]. In a normal range the MetHb concentration makes up to 0.5% of the total haemoglobin. In case that MetHb raises above 10% the skin and the mucosa develops blue coloration (cyanosis).

	Haemoglobin reference range	
Male	140 g/l - 180g/l	8.7mmol/l – 11.2mmol/l
Female	120 g/l - 160g/l	7.4mmol/l – 9.9mmol/l

Table 1: Haemoglobin reference range [57]

In Table 1 the typical values for the haemoglobin concentration in a health adult are shown for male and females. If the concentration is below normal, this is called anemia. The most common type of anaemia is iron-deficiency anaemia, caused when there is not enough iron in the body.

If iron-deficiency anaemia is not treated, there are a range of possible complications. For example in adults, it can affect the ability to work and exercise. It can also increase the risk of heart problems.

A reduction of haemoglobin is usually accompanied by a fall in red cell count and hematocrit but these may be normal in some patients with subnormal haemoglobin levels. Alterations in total circulating plasma volume as well as total circulating haemoglobin mass determine the haemoglobin concentration. After an acute major blood loss, anaemia is not immediately apparent because the total blood volume is reduced. It takes up to a day for the plasma volume to be replaced and so for the degree of anaemia to become apparent. The regeneration of haemoglobin mass takes much longer. If a patient has symptoms for anaemia these are usually weaknesses, lethargy or headaches [58].

Other symptoms of iron-deficiency anaemia include:

- shortness of breath particularly on exercise
- feeling tired
- palpitations
- looking pale
- a rapid pulse

Hematocrit is an important indicator of haemoglobin concentration. Hematocrit is the proportion, by volume, of the blood that consists of red blood cells. The hematocrit (hct) is expressed as a percentage. For example, a hematocrit of 25% means that there are 25 milliliters of red blood cells in 100 milliliters of blood. The hematocrit is typically measured from a blood sample by an automated machine which makes several other measurements at the same time. Most of these machines in fact do not directly measure the hematocrit, but instead calculate it based on the determination of the amount of haemoglobin and the average volume of the red blood cells. The hematocrit can also be determined using a less automated method based on centrifuging a blood sample. When a tube of blood is centrifuged, the red cells will be packed into the bottom of the tube. The proportion of red cells to the total blood volume can be visually measured [60]. In normal conditions, there is a linear relationship between hematocrit and the concentration of haemoglobin (ctHb). The relationship can be expressed as follows:

$$Hct(\%) = \left( \left( 0.485 \times ctHb \left( \frac{mmol}{L} \right) + 0.0083 \right) \right) \times 100 \quad (2.1)$$

A low hematocrit reflects a low number of circulating red blood cells and is an indicator of a decrease in the oxygen-carrying capacity or of overhydration. A high hematocrit may reflect an absolute increase in the number of erythrocytes<sup>1</sup>, or a decrease in plasma volume.

The normal healthy levels in terms of Hematocrit range are shown in Table 2.

	Hematocrit reference range
Male	40% - 52%
Female	37% -46%

Table 2: Hematocrit reference range [57]

---

<sup>1</sup> Red blood cells are also referred to as erythrocytes

#### 4.2.2 The blood oxygenation

The oxygen concentration in blood depends from the oxygen partial pressure  $pO_2$  and the Bunsen solubility coefficient  $\alpha$ . The Henry Dalton law (equation 4.1) explains the relationship between both mentioned coefficients:

$$cO_2 = \alpha_{O_2} pO_2 \quad (4.1)$$

The oxyhaemoglobin dissociation curve, as shown in Figure 4-3, describes the relationship between the partial pressure of oxygen in the blood and the percentage of oxygen bound to haemoglobin compared to the maximum.

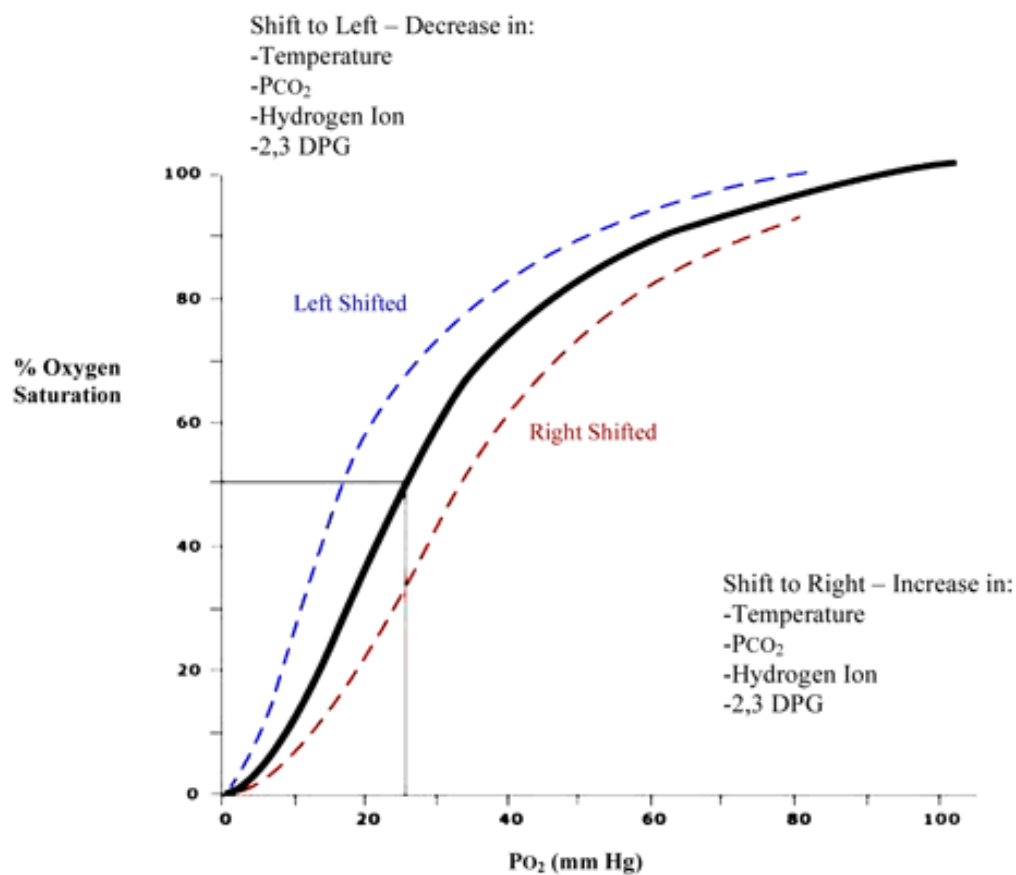


Figure 4-3: Oxyhaemoglobin dissociation curve [58]

Factors such as decreasing carbon dioxide partial pressure, increasing pH, decreasing temperature and decreasing of 2.3 diphosphoglyerat(DPG) will shift the curve

toward left [59]. A left shifted curve implies that the haemoglobin molecules will be more highly saturated at a lower partial pressure of oxygen.

### 4.3 Optical properties of Haemoglobin

Within the optical window defined in Section 2.2 (600nm-1000nm) the most dominant absorber of NIR light is the haemoglobin in its various forms [61, 62]. The chemical binding of the different haemoglobin species also changes the physical properties of the haemoglobin. Figure 4-4 shows the variation extinction coefficient of oxyhaemoglobin, reduced haemoglobin, methaemoglobin and carboxyhaemoglobin in the range from 600nm to 1000nm. Below 600nm the slope of the molar extinction of haemoglobin is much higher than within the optical window and the light penetration is low. At a wavelength of around 805nm is a so called isosbestic point where the extinction of oxyhaemoglobin and reduced haemoglobin are the same. At this wavelength the absorption does not depend on the oxygen saturation.

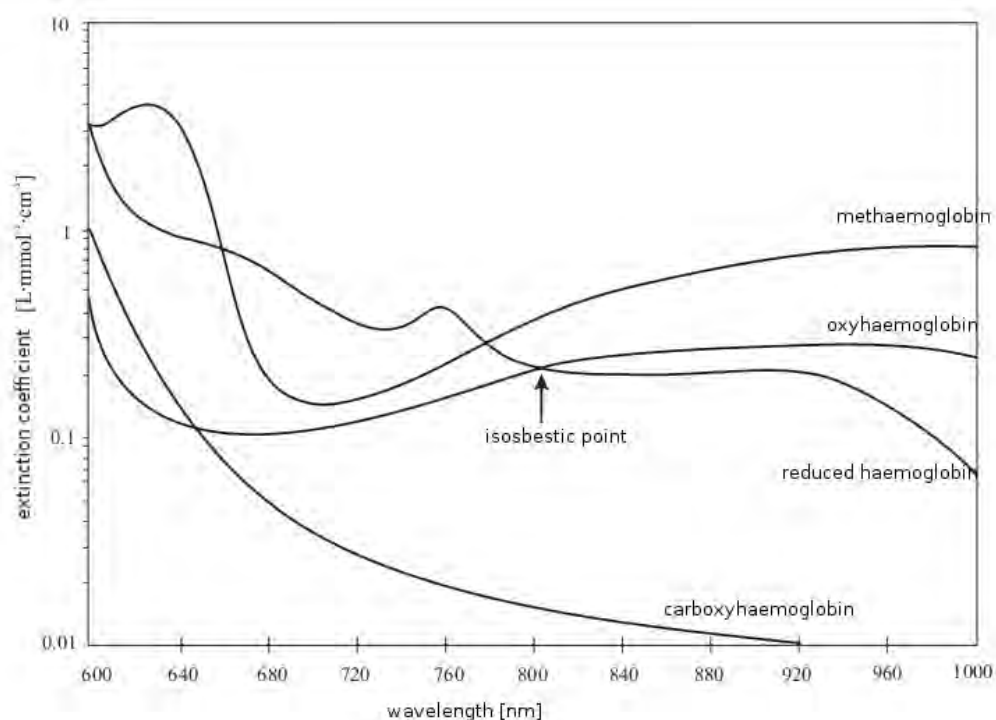


Figure 4-4: Extinction coefficient of the four most common haemoglobin derivatives [75]

The absorption coefficient for reduced ( $\mu_a^{HHb}$ ) and oxyhaemoglobin ( $\mu_a^{HbO_2}$ ) can be calculated by using the molar mass of haemoglobin ( $M_{Hb} = \frac{64500g}{mol}$ ), the concentration  $c_{Hb}$  and the appropriate extinction coefficient ( $\varepsilon^{HHb}(\lambda)$ ,  $\varepsilon^{HbO_2}(\lambda)$ ).

$$\mu_a^{HbO_2} = \ln(10) \frac{\varepsilon^{HbO_2}(\lambda) c_{Hb}}{M_{Hb}} = 2,303 \frac{\varepsilon^{HHb}(\lambda) c_{Hb}}{64500g/l} \quad (4.2)$$

$$\mu_a^{HHb} = \ln(10) \frac{\varepsilon^{HHb}(\lambda) c_{Hb}}{M_{Hb}} = 2,303 \frac{\varepsilon^{HHb}(\lambda) c_{Hb}}{64500g/l} \quad (4.3)$$

The molar extinction coefficient is based on a common logarithm which is considered with the coefficient  $\ln(10)$  [62]. Figure 4-5 shows the absorption spectra for blood ( $c_{Hb} = 18g/l$ ) from 400nm to 1800nm [54]. Above 1200nm the absorption coefficient of reduced and oxygenated haemoglobin is virtually indistinguishable and follows the water absorption.

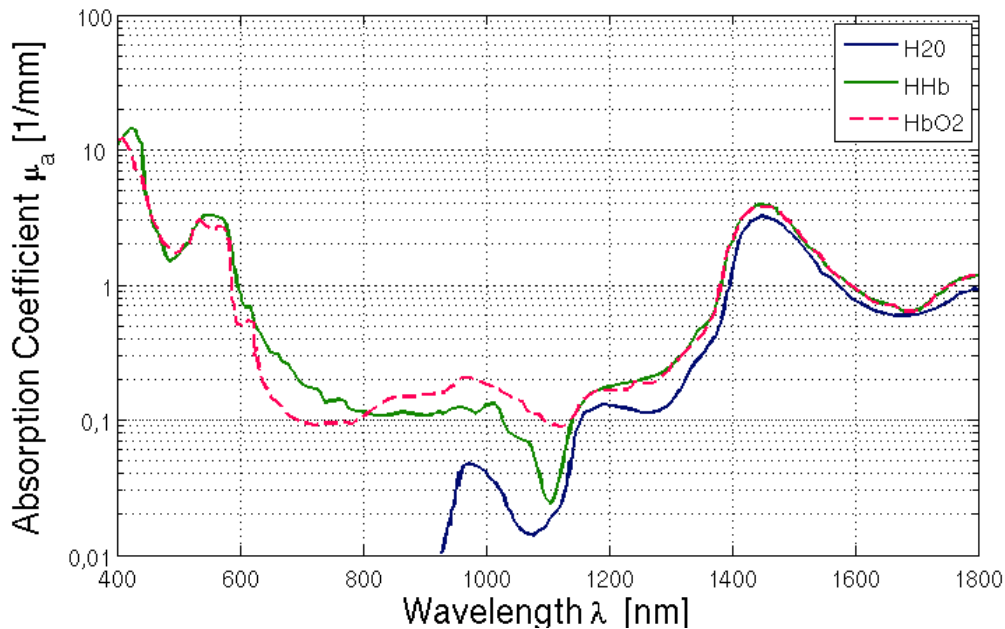


Figure 4-5: Blood Absorption spectra ( $c_{Hb} = 18g/l$ ) for oxyhaemoglobin, reduced haemoglobin and water [61]

### 4.3.1 The Human Circulatory System

The human circulatory system is a fast regulatory transport system [56]. This closed circuit consists of parallel and serially connected blood vessels and the heart acts as a circulation pump. The heart is a hollow muscle which is divided into four chambers. These are the right atrium, the right ventricle and the left atrium and the left ventricle. In functional and morphological terms the circulatory system consists of two serial sections. The heart also can be considered as two serial pumps. The right cardiac side absorbs the de-oxygenated blood from the body and transports it to the lungs (lung circuit), where it is re-oxygenated. The oxygenated blood arrives at the left cardiac side, wherefrom the dispensation to various organs takes place (body circuit). The oxygenated blood in the body circuit is pumped from the left ventricle via the aorta and main arteries whose sub branches lead to the tissue and organs. Following the next stage of branching into arteriole and capillary, the oxygen and nutrients and the ingestion of carbon monoxide and intermediate catabolic products are distributed to the tissue and organs of the body [56]. Finally the capillaries terminate into venules and veins which transport the deoxygenated blood back to the right atrium. Figure 4-6 shows a schematic of the human cardiovascular system.

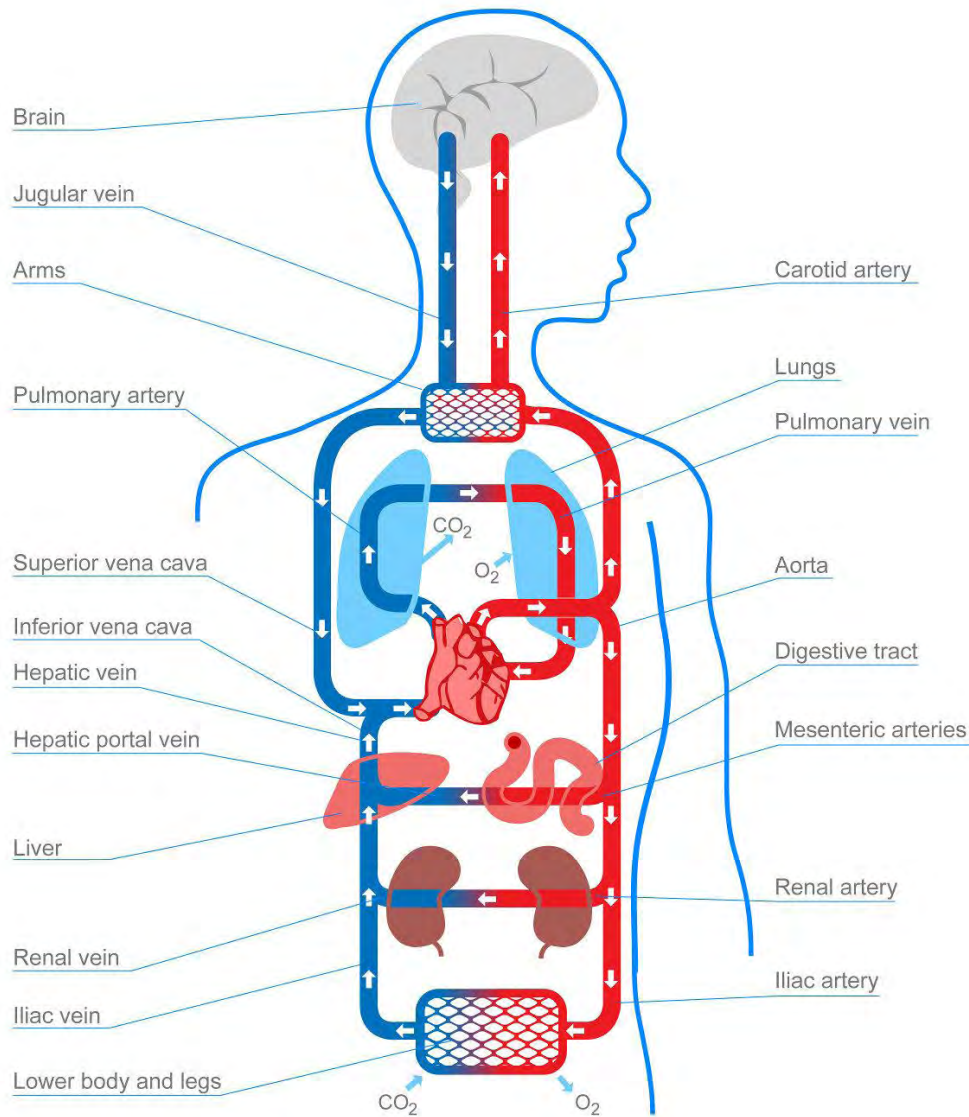


Figure 4-6: The Human Circulatory System [95]

#### 4.3.1.1 Formation of pulse waves and regulation mechanism

A pulsatile flow exists within the arteries of the body and the lung vascular system. The vascular walls are not stiff but rather elastic. Pressure changes and fluid shifts propagate as wavelike pulse motions of the wall. The origin of the pulse wave is the blood flow which results from contractive left or rather right chamber into the arterial parts of the body and lung vascular system[65]. Thereby a local pressure increase occurs at the entrance of the vascular system caused by the acceleration of

the blood in the beginning of the systole. The consequence is a distension of the elastic vascular wall and a local cross section increase of the vessel diameter. The wall distension causes volume storage of the fluid in new available room. Instead of an acceleration of the whole liquid column in the arterial system at the same time, the acceleration only extends on the first part of the system. By splitting the wave in multiple parts of small time periods first a fluid acceleration occurs which result in a higher pressure and increasing the diameter. Then the stretched wall contracting and pushes the storage volume into the next bordering section where the same procedure is starts. In this way the wave is moving along the whole arteries. This effect is also called “windkessel effect”. Figure 4-7 shows a typical time resolved optical cardiograph.

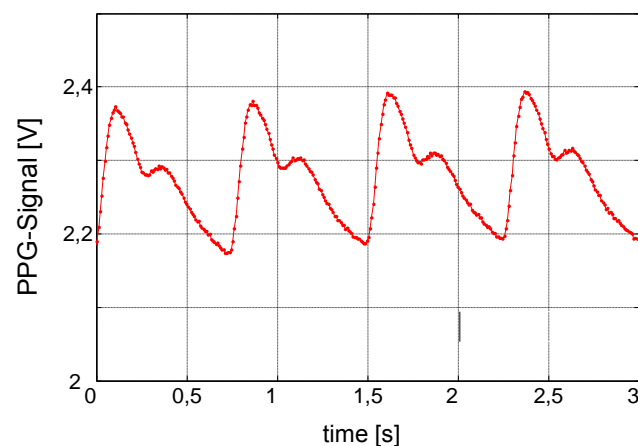


Figure 4-7: Typical pulse wave obtained with the Non-Invasive Haemoglobin Sensor System

The increase of the aorta diameter during the diastole phase in the ascending aorta is around 6% and in the aorta pulmonalis around 10%. The dicrotic notch (the shoulder on the peaks in Figure 4-7) indicates the cessation of systole and represents closure of the aortic valve and subsequent retrograde flow. The location of the dicrotic notch varies according to the timing of aortic closure in the cardiac cycle. An alternative view is that the dicrotic notch in an arterial pressure waveform does not necessarily correspond to the incisura in the aortic pressure waveform caused by closure of the aortic valve. The dicrotic notch and the dicrotic wave that follow it are thought to be due to a reflected pressure wave [63]. Klemsal et al [64] shows in animal experiments that the height of the dicrotic notch reflects the elasticity of the large and middle vessels.

#### 4.4 The Human tissue

The optical properties of the skin are important since all *in vivo* NIRS measurements will include a contribution from the skin. Figure 4.8 shows a three-dimensional view of the human skin and its two main layers: the epidermis and the dermis. Beneath the dermis is the fat layer referred to as the hypo- or subdermis, but which is not strictly part of the skin.

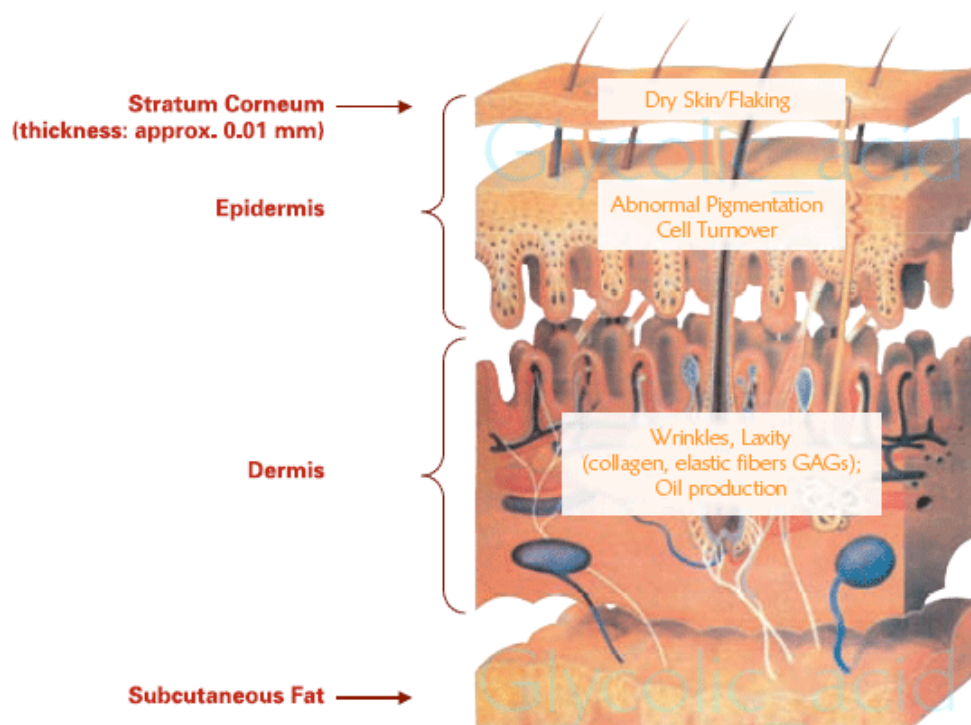


Figure 4-8: Three-dimensional view of the skin [65]

The epidermis is made up of stratified squamous epithelium with an underlying basal lamina and contains no blood vessels. Cells in the deepest layers are nourished by diffusion from capillaries underneath the epidermis, which are linked to an arteriole and a venule. In some areas like the ears, nose and fingertips arterial shunt vessels may bypass the network. The formation of cells takes place at the basal layer through mitosis. The daughter cells move up the strata changing shape and composition due to their isolation from the blood source, which leads to cell death. Keratinocytes, melanocytes, Langerhans and Merckels cells are the main type of cells within the epidermis [63]. Melanin, which is responsible for the tan of the skin, is

produced by melanocytes. The thickness of the epidermis is usually between 40  $\mu\text{m}$  (forehead region) and 1.5mm (hand surface, sole of foot).

The dermis is located underneath the epidermis and cushions the body from stress and strain. The tight connection between the dermis and epidermis is provided by a basement membrane. Contents of the dermis include hair follicles, apocrine glands, sebaceous glands, sweat glands, lymphatic vessels and blood vessels. Deeper into the dermis nerve endings provide the sense of heat and touch. The dermis is subdivided into the papillary region, a superficial area adjacent to the epidermis, and the reticular region. The papillary region consists of connective tissue and is named for the papillae that bind the dermis with the epidermis. The papillae provide the dermis with a rough surface due to the finger like geometry [66]. In some regions of the human body like palms, fingers, toes and soles, papillae form contours on the surface of the skin. Those contours are called friction ridges. They occur in patterns, which are genetically determined and unique to the individual. This uniqueness and certainty makes identification via fingerprint or footprint possible. The reticular region is much thicker than the papillary region and consists of dense irregular connective tissue. It is named for the dense concentration of elastic, collagenous and reticular fibres. The strength, elasticity and extensibility of the dermis originate from those fibres. Other components like roots of the hair, sweat glands, nails, receptors and blood vessels are also located in the dermis. The thickness of the dermis varies between 1 and 4 mm underneath the dermis lays the hypodermis, which is not a part of the skin. The hypodermis is responsible for the attachment of bones and muscles to the skin as well as supplying the muscles with nerves and blood vessels. Fat within the hypodermis serves as padding and insulation for the body. The thickness of the hypodermis can be several centimetres [66].

The optical properties of the skin are well known [67]. Saidi et al shows that the scattering and absorption properties of the skin can be described by a superposition of a Mie-scattering portion caused by the collagen fibres (diameter  $2,8 \pm 0,8 \mu\text{m}$ ) and a Rayleigh portion caused by smaller structures.

Saidi reported following approximation for the reduced scattering coefficient  $\mu_s'$  [63]:

$$\mu_s'(\lambda) = [ (2 * 10^4 \{\lambda\}^{-1,5}) + (2 * 10^{11} \{\lambda\}^{-4}) ] mm^{-1} \quad (4.4)$$

MIE- Portion                      Rayleigh-Portion

Figure 4-9 shows the reduced scattering coefficient as a function of the wavelength.

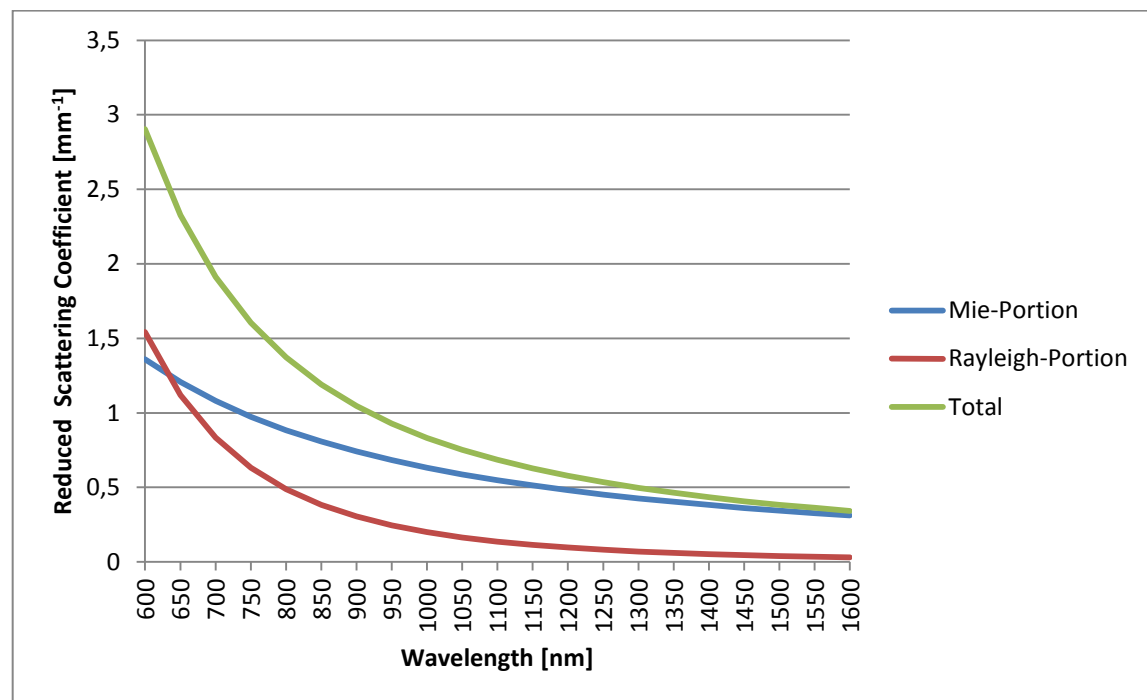


Figure 4-9: The reduced scattering coefficient as function as function of the wavelength, equation 4-5

Every skin layer has different absorption properties. The absorption coefficient of the epidermis  $\mu_a^{epidermis}(\lambda)$  depends on the melanin concentration  $f_{mel}$  of the observed skin area [68, 69]. The absorption coefficient consists of background absorption from unpigmented skin (vitiligo)  $\mu_a^{vitiligo}(\lambda)$  and the characteristic melanin absorption  $\mu_a^{Mel}(\lambda)$  :

$$\mu_a^{epidermis}(\lambda) = (1 - f_{mel})\mu_a^{vitiligo}(\lambda) + f_{mel}\mu_a^{Mel}(\lambda) \quad (4.5)$$

Jacques et al reported [70] an approximation for the unpigmented skin in the visible and near infrared region:

$$\mu_a^{vitiligo}(\lambda) = 0,0244 + 85,3 \exp\left(-\frac{(\lambda) - 154}{66,2}\right) \quad (4.6)$$

The absorption of melanin can be approximated with [66]:

$$\mu_a^{Mel}(\lambda) = 6,6 * 10^{10} (\lambda)^{-3,33} \quad (4.7)$$

The melanin concentration differs for each type of skin and standard values can be found in the literature [69, 70]:

Type of skin	$f_{mel}$
Light skinned	1,3 - 6,3 %
Moderate pigmented	11 - 16 %
Strong pigmented	18 - 43 %

Table 3: Melanin concentration standard values for different type of skin [69, 70]

Figure 4-10 shows the absorption spectra of pure Melanin, unpigmented skin and the epidermis with a melanin concentration of 6 %. While the epidermis is just 10  $\mu\text{m}$  up to 1.5mm thick, the contribution to the attenuation of light is strongly dependent on the type of skin.

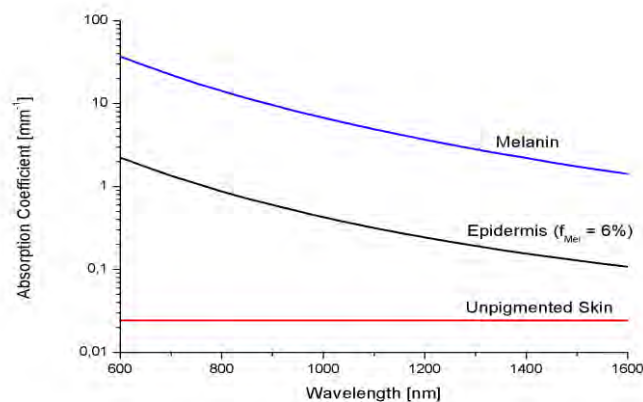


Figure 4-10: Absorption Spectra of Melanin, Epidermis and Unpigmented Skin from 600 to 1600nm

#### **4.5 Summary**

This chapter gives a short introduction into the physiological basics that are necessary to understand the assumptions are made in chapter five. The human circulatory system as source of the pulse waves, the optical properties of the human skin and the blood components are explained in detail. Based on these fundamentals and theory of light transport in biological tissue, the principle of a non-invasive haemoglobin measurement is presented in the next chapter.

## 5 The non-invasive Hb measurement

### 5.1 Introduction

In this chapter the concept for the non-invasive haemoglobin measurement is described. Based on the photoplethysmography which is described in chapter 5.2 the pulse oximetry is explained in chapter 5.3. These both methods result in a method for a non-invasive Hb measurement in chapter 5.4.

### 5.2 Measurement Method Photoplethysmography

A photoplethysmograph (PPG) is an optically obtained plethysmograph, a volumetric measurement of an organ. A PPG is often obtained by using a pulse oximeter which illuminates the skin and measures changes in light absorption (Shelley and Shelley, 2001). A conventional pulse oximeter monitors the perfusion of blood to the dermis and subcutaneous tissue of the skin. With each cardiac cycle the heart pumps blood to the periphery. Even though this pressure pulse is somewhat damped by the time it reaches the skin, it is enough to distend the arteries and arterioles in the subcutaneous tissue. If the pulse oximeter is attached without compressing the skin, a pressure pulse can also be seen from the venous plexus, as a small secondary peak. The change in volume caused by the pressure pulse is detected by illuminating the skin with the light and then measuring the amount of light either transmitted or reflected to a photodiode. Each cardiac cycle appears as a peak, as seen in the figure. Because blood flow to the skin can be modulated by multiple other physiological systems, the PPG can also be used to monitor breathing, hypovolemia, and other circulatory conditions. Additionally, the shape of the PPG waveform differs from subject to subject, and varies with the location and manner in which the pulse oximeter is attached [93].

### 5.3 Measurement Method Pulse Oximetry

Perhaps pulse oximetry is the most established optical measurement technique for monitoring the arterial oxygen saturation. Recognised worldwide as the standard of care in anaesthesiology, it is widely used in intensive care, operating rooms, emergency, patient transport, birth and delivery, neonatal care, sleep laboratories, home care, and in veterinary medicine. Oxygen is necessary for the functioning cells in human and animal bodies. Following a long absence of oxygen, cells will die. Gases such as oxygen are not particularly soluble in blood. For this reason an effective measurement method for oxygen transport is necessary. The blood component haemoglobin provides a binding mechanism that allows oxygen transportation in blood [71]. With haemoglobin the amount of oxygen transported is 65 times higher than without. Pulse oximetry is a non-invasive optical method to measure the oxygenation of haemoglobin in human blood. The Beer-Lambert law (equation 3.3) describes the reduction of light which is travelling through a homogeneous medium contain an absorbing substance.

Therefore, Beer-Lambert law allows the concentrations of  $n$  different substances to be determined if the absorbance of light is measured at  $n$  different wavelengths and the extinction coefficient of the substances are known [72, 73].

The measuring principle of pulse oximetry is based on the different absorbance properties of oxygenated and deoxygenated haemoglobin and the pulsatile intensity variation. The volume and pressure fluctuations are generated in the systolic phase of the heart. Oxygenated ( $\text{HbO}_2$ ) and reduced haemoglobin (HHb) are the main light absorbers in human blood. A further distinction is drawn between functional and dysfunctional haemoglobin. Functional Haemoglobin is able to bind reversible oxygen, dysfunctional is not. Most of the haemoglobin in healthy blood is functional haemoglobin whose extinction coefficient is greater than that of dysfunctional haemoglobin. In pulsoximetry the oxygen saturation is defined as [74, 75, 76]:

$$SaO_{2,funct} = \frac{c_{HbO_2}}{c_{HbO_2} + c_{HHb}} * 100\% \quad (5.1)$$

Thus the concentration of oxygenated haemoglobin ( $c_{HbO_2}$ ) and reduced haemoglobin

( $c_{HHb}$ ) can be expressed as:

$$c_{HbO_2} = (SaO_2)(c_{HbO_2} + c_{HHb}) \quad (5.2)$$

$$c_{HHb} = (1 - SaO_2)(c_{HbO_2} + c_{HHb}) \quad (5.3)$$

According to equation 3-5 the total absorbance  $A_t$  results in:

$$A_t = \sum_{i=1}^n \varepsilon_{HbO_2}(\lambda) c_{HbO_2} d_{HbO_2} + \varepsilon_{HHb}(\lambda) c_{HHb} d_{HHb} \quad (5.4)$$

In the case that the optical path length  $d$  is identical for oxygenated and deoxygenated haemoglobin equation (5.4) leads to equation 5.5 by substituting equation 5.2 and 5.3.

$$A_t = d(c_{HbO_2} + c_{HHb})[\varepsilon_{HbO_2} SaO_2 + \varepsilon_{HHb}(\lambda)(1 - SO_2)] \quad (5.5)$$

Using this equation, it is possible to determine the functional oxygen saturation of blood *in vitro* with a sample of arterial blood and a low cost spectrometer. The arteries contain more blood during the systolic phase of the heart than during the diastolic phase, due to an increased diameter of the arteries during the systolic phase. This effect occurs only in arteries but not in veins. For this reason the absorbance of light in tissues with arteries increases during systole because the amount of haemoglobin (absorber) is higher and the light passes through a longer optical path length  $\Delta d$  in the arteries. This altering (AC) part allows the differentiation between the absorbance due to venous blood (DC part) and that due to the pulsatile component of the total absorbance (AC part). Figure 5-1 shows the absorption model of light penetrating tissue to sufficient depth to encounter arterial blood and the composition of the AC and DC part.

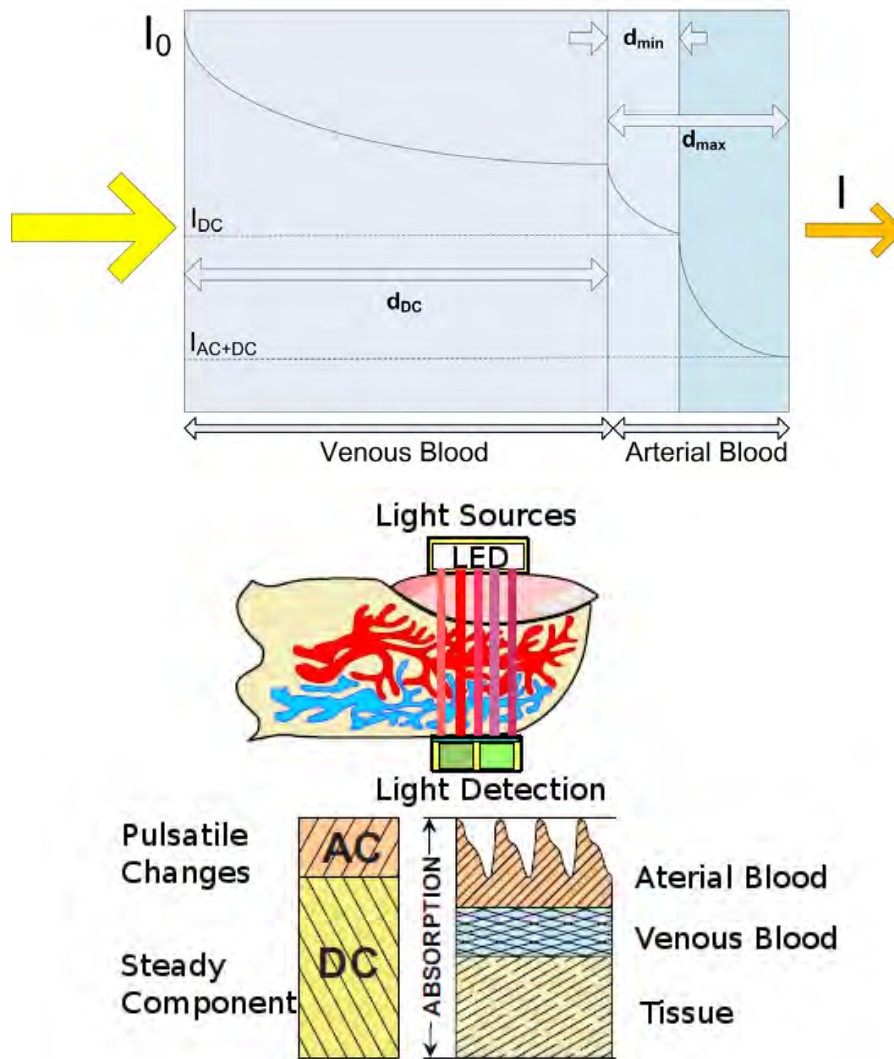


Figure 5-1: Model of the Tissue Layers and composition of the AC and DC part

For a transmission measurement (tissue thickness smaller than 15mm) only measuring points with an adequate perfusion are eligible. Usually the finger, the earlobe or in the case of infants the toe are used. Figure 5-2 shows a preparation of the hand vessels which demonstrates the good perfusion of the finger terminal element.



Figure 5-2: Illustration of the hand vessels

According to Beer-Lambert law the DC component can be written as:

$$I_{DC} = I_o e^{-\varepsilon_{DC}(\lambda)c_{DC}d_{DC}} e^{-[\varepsilon_{HbO_2}(\lambda)c_{HbO_2} + \varepsilon_{HHb}(\lambda)c_{HHb}]d_{min}} \quad (5.6)$$

The alternating component is by definition attributed to the arterial blood. For this reason, only the arterial layer thickness  $\Delta d$  change which in turn causes an intensity variation.

$$I_{AC + DC} = I_o e^{-\varepsilon_{DC}(\lambda)c_{DC}d_{DC}} e^{-[\varepsilon_{HbO_2}(\lambda)c_{HbO_2} + \varepsilon_{HHb}(\lambda)c_{HHb}]d_{max}} \quad (5.7)$$

The light intensity  $I$  of the light arriving at the photo detector is a function of the diameter  $d$  of arteries. During one cardiac cycle the diameter of the arteries changes from  $d_{min}$  to  $d_{max}$ . By substituting  $d$  with  $d_{min} + \Delta d$  the following equation (5.8) can be derived from the Beer-Lambert where  $I$  is expressed as a function of  $I_{DC}$  and  $\Delta d$  [75 , 76]:

$$I = I_{DC} e^{-[\varepsilon_{HbO_2}(\lambda)c_{HbO_2} + \varepsilon_{HHb}(\lambda)c_{HHb}]\Delta d} \quad (5.8)$$

Equation 5-8 identifies the possibility to measure the arterial oxygen saturation using two different wavelengths. It is to be measured at wavelengths where the differences in the extinction coefficients of oxygenated and deoxygenated haemoglobin are high. Pulse oximeters normally work in the wavelength range from 600nm to 1000nm. Figure 5-3 shows the absorption spectra of HHb and HbO<sub>2</sub> and their significant differences at selected wavelengths.

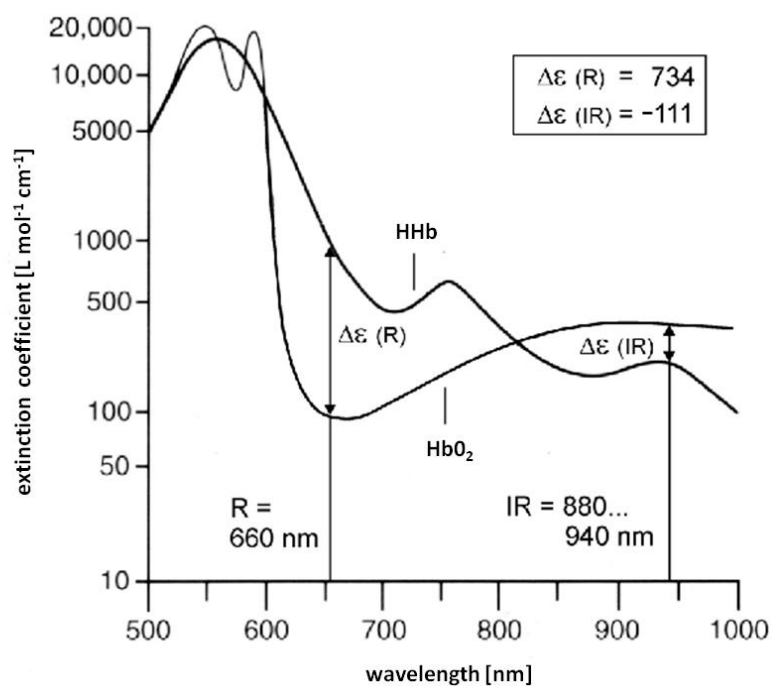


Figure 5-3: Pulse oximeter wavelengths and the absorption spectra of oxygenated and deoxygenated haemoglobin

Light emitting diodes (LEDs) are sources which produce different output light intensities at different wavelengths. For comparison of the two wavelengths a normalisation is therefore necessary. As a result of the normalisation the optical path length (if  $d_{\lambda_1} = d_{\lambda_2}$ ) through the tissue and the incident intensity  $I_0$  is no longer significant. The ratio of the AC/DC -values of the both wavelengths used results in the ratio  $R$ .

$$R = \frac{A_{t,RED}}{A_{t,IR}} = \frac{\ln\left(\frac{I_{AC+DC,RED}}{I_{DC,RED}}\right)}{\ln\left(\frac{I_{AC+DC,IR}}{I_{DC,IR}}\right)} \quad (5.9)$$

By using a normalised equation 5.9 and equation 5.5 the ratio can be derived as:

$$R = \frac{\varepsilon_{HHb}(\lambda_{RED}) + SaO_2[\varepsilon_{HbO_2}(\lambda_{RED}) - \varepsilon_{HHb}(\lambda_{RED})]}{\varepsilon_{HHb}(\lambda_{IR}) + SaO_2[\varepsilon_{HbO_2}(\lambda_{IR}) - \varepsilon_{HHb}(\lambda_{IR})]} \quad (5.10)$$

With the determined value  $R$  and the extinction coefficients of oxygenated ( $\varepsilon_{HbO_2}$ ) and deoxygenated haemoglobin ( $\varepsilon_{HHb}$ ) it is feasible to calculate the arterial oxygen saturation:

$$SaO_2 = \frac{\varepsilon_{HHb}(\lambda_{IR})R - \varepsilon_{HHb}(\lambda_{RED})}{\varepsilon_{HbO_2}(\lambda_{RED}) - \varepsilon_{HHb}(\lambda_{RED}) - R[\varepsilon_{HbO_2}(\lambda_{IR}) - \varepsilon_{HHb}(\lambda_{IR})]} \quad (5.11)$$

This theoretical equation leads to incorrect results in practice, because the optical properties encountered in human blood are much more complicated than the simplified model due to the assumptions made in Figure 5-1. The conditions of Beer-Lambert's law are not complied with due to the complex multilayer absorber. Therefore a calibration of the pulse oximeter in comparison to a blood gas analysis is inevitable. Figure 5-4 shows the difference between Beer-Lambert's law and calibration for the Philips Sensor M1190A [77]. The calibration process will be explained in Chapter 7 using the example of the haemoglobin sensor system.

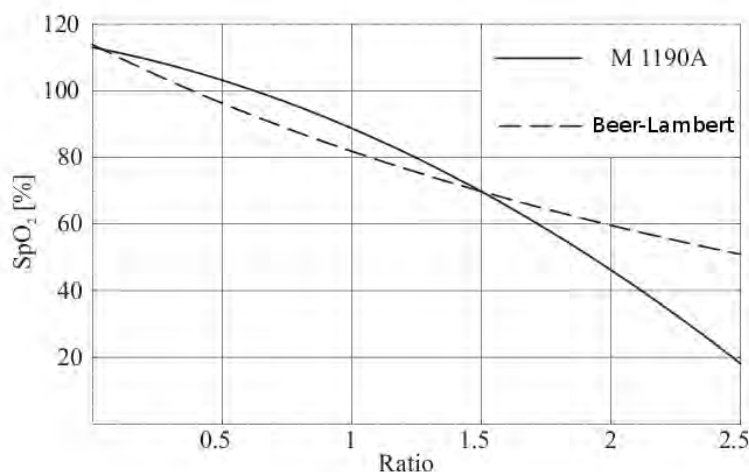


Figure 5-4: The commercial pulse oximeter calibration curve in comparison with Beer-Lambert for the Philips Sensor M1190A [77]

#### 5.4 Concept of Non-Invasive Haemoglobin Determination

Based on the pulse oximetry derivation the following concept explains the underlying theory of how to measure the haemoglobin concentration in blood non-invasively. The optical absorption and scattering of blood is influenced mainly by the total haemoglobin concentration and the amount of red blood cells. The principle of measurement is based on the fact that there is a substantial absorption/transmission difference of light in the red and near infrared region between oxygenated (HbO<sub>2</sub>), reduced haemoglobin (HHb), and blood plasma which optical properties are similar to water. As shown in Figure 5-5, HHb is optically much denser to the red light than HbO<sub>2</sub>, whereas the reverse is true in the near infrared region although to a lesser degree. The existence of the isosbestic wavelength band in the range of 800 nm to 810 nm within the transmission of HbO<sub>2</sub> and HHb is equal is critical to the successful measurement of the total haemoglobin by optical means. Figure 5-5 shows the transmission spectra of blood for different haemoglobin values [78].

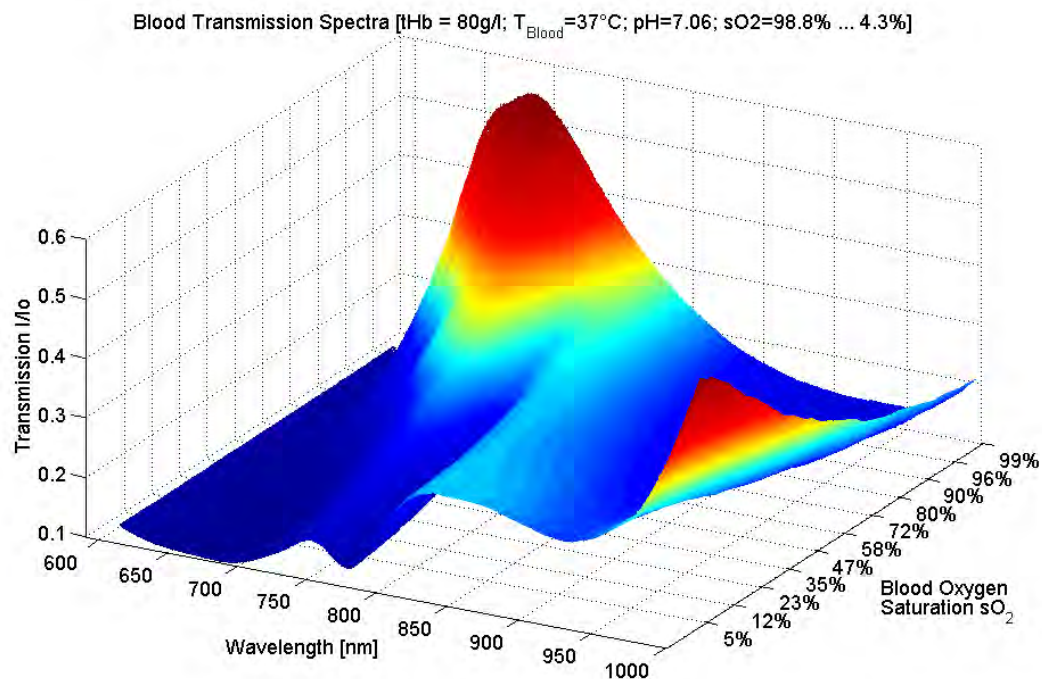


Figure 5-5: Transmission spectra with different oxygenation levels and identical Hb of 80 g/l.

To determine the haemoglobin concentration the wavelength choice is critical and therefore suitable wavelengths need to be selected.

The following assumptions are made:

- The absorption of plasma and pure water is similar
- Red blood cells are mainly filled with haemoglobin and water
- The absorption spectra of HHb and HbO<sub>2</sub> above 1200nm is identical and the absorption is dominated by water
- The concentration of haemoglobin is constant per erythrocyte

The measurement should not depend on the oxygen saturation and that means that the measurement is only practicable at the isobestic point where the extinction coefficient of both haemoglobin derivatives is identical. For the purpose of this investigation the wavelength was selected as 810nm. According to the assumption that red blood cells are mainly filled with water, the absorption coefficient of blood is similar to a solution consisting HHb, HbO<sub>2</sub> and plasma and the absorption of HHb

and HbO<sub>2</sub> is indistinguishable to the absorption of water above 1200nm. If the system is able to isolate the presence of water in the blood it is therefore necessary to select a second wavelength in this region which is outside the traditional optical diagnostic window. Finally the determination of haemoglobin concentration measurement is performed at the wavelengths  $\lambda_1 = 810\text{nm}$  and  $\lambda_2 = 1300\text{nm}$ .

According to equation 5-9 the ratio of the AC/DC ratio of both wavelengths leads to the quotient H:

$$H = \frac{A_{t,810\text{nm}}}{A_{t,1300\text{nm}}} = \frac{\ln\left(\frac{I_{AC+DC,810\text{nm}}}{I_{DC,810\text{nm}}}\right)}{\ln\left(\frac{I_{AC+DC,1300\text{nm}}}{I_{DC,1300\text{nm}}}\right)} \quad (5.12)$$

At a wavelength of 810nm the absorption coefficient of water is insignificantly small in comparison to the haemoglobin concentration. At a wavelength of 1300nm this situation is completely different (Figure 4-5) with the water absorption closely matching the oxygenated and non-oxygenated haemoglobin. It can be assumed that. Equation 5.12 can be rewritten as:

$$H = \frac{\mu_a^{Hb}(\lambda_{810\text{nm}})}{\mu_a^{H_2O}(\lambda_{1300\text{nm}})} \quad (5.13)$$

The absorption coefficient  $\mu_a^{Hb}$  depends on the haemoglobin concentration cHb equation 4.13 can be written as:

$$H = \ln(10) \frac{\varepsilon_{Hb}(\lambda_{810\text{nm}})c_{Hb}}{\mu_a^{H_2O}(\lambda_{1300\text{nm}})M_{Hb}} \quad (5.14)$$

Finally the haemoglobin concentration can be determined as follows:

$$c_{Hb} = 0,434 \frac{H * \mu_a^{H_2O}(\lambda_{1300\text{nm}})64500\text{g/mol}}{\varepsilon_{Hb}(\lambda_{810\text{nm}})} \quad (5.15)$$

## 5.5 Summary

With the equations described at the end of chapter 5.4 and if the assumptions made for the RTT were valid it would be theoretically possible to calculate the total haemoglobin concentration in this manner. However, in practice the experimentally measured optical intensity values do not reflect the actual haemoglobin concentration and therefore the theoretical model is invalid for completely describing the Hb measurement. Due to the overwhelming nonlinear effects of tissue scattering, a calibration of the PPG measurement for the total haemoglobin determination is necessary as in case of the commercial pulse oximeters.

## 6 Hb Sensor System

### 6.1 Introduction

This chapter describes the practical elements Haemoglobin sensor system developed in this investigation and the requirements to design such a system. To capture pulse waves above a wavelength of 1100nm where the water absorption dominates requires level of a high accuracy in the measurement system. Every module of the sensors system is described in this chapter. Firstly the light sources and the receiver unit which are located within the sensor head are characterised followed by a description of the receiver and the remaining system components. The both last section explains the controller program, the analysing software and the algorithmic.

### 6.2 Light sources

The spectral range width of LEDs is much wider in comparison to Laser diodes but on the other side LEDs are much cheaper, robust (i.e. less sensitive to failure) and smaller. Technological development in LEDs fabrication and packaging over in the last years and currently LEDs with centre wavelengths of 670nm, 810nm and 1300nm are available with a sufficient power output. The power output was especially a problem for higher centre wavelengths. The LED has one more disadvantage in comparison to the laser diode which is the lack of monitoring photodiode inside the housing. By analysing the photocurrent of the photo diode it is feasible to control the power of the laser diode output and stabilising the centre wavelength. The LED is a semi-conductor and as all other semi-conductors the LED is influenced by temperature. This temperature effect causes a wavelength drift and intensity fluctuation. In opposition to an ohm load the output of an LED is controlled by the current. Figure 6-1 shows the characteristic graph of a 3W high power LED. Below 3Volt is no current flow and above the same value the forward current rises rapidly and for this reason it is essential that the LED output is controlled by the LED forward current.

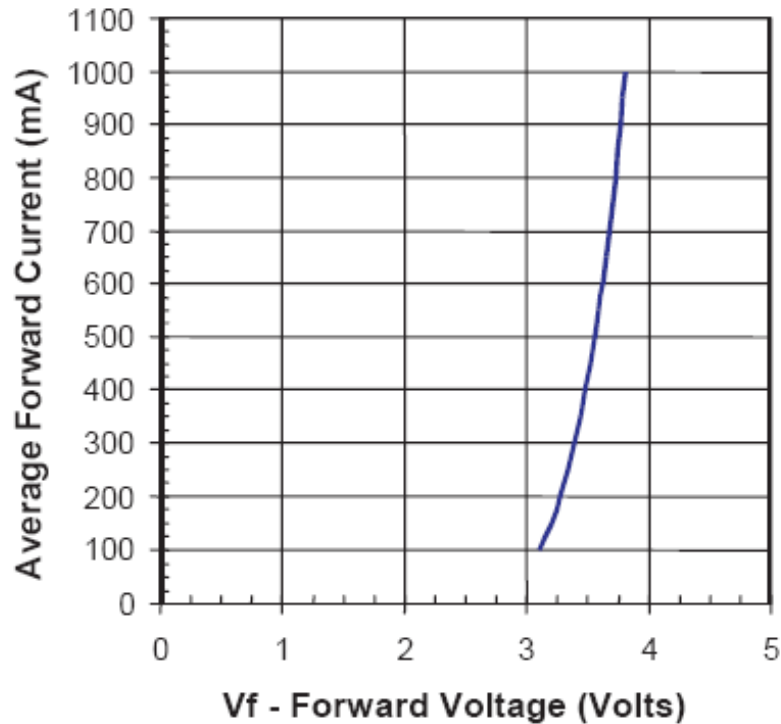


Figure 6-1: Typical LED characteristic graph

Figure 6-2 shows a simple but reliable adjustable current source which enables the possibility to control the LED output. The amplifier is adjusting the voltage output that the applied voltage on resistor  $R_1$  is identical to  $U_2$ . The resulting current through the resistor  $R_1$  is  $U_2/R_1$ . In the case of the bipolar transistor a part of the emitter current drains out of the basis. The current amplification  $B$  depends from  $U_{CE}$  and  $I_B$  changes also with the Output Voltage  $U_1$ . Equation 6.1 explains the link between actuating variables and the LED current [79].

$$I_{LED} = \frac{U_2}{R_1} \left(1 - \frac{1}{B}\right) \quad (6.1)$$

By using the current source from figure 6-2 and corresponding spectrometers for the wavelength output the LED properties were analysed. The measurement was set-up in the dark room of the optical fibre sensor research of the University of Limerick. The LED was coupled with the spectrometer by a fibre and by using an optical attenuator an over steering was avoided. As spectrometer the Ocean Optics SR2000-TR was used. The LED spectrum was measured continually and a parallel running

Matlab program analysed the peak wavelength drift and generated a relative output spectra. Figure 6-3 and 6-4 shows the recorded spectra for the 670nm LED (ELD-670-524) with a forward current of 5mA and 20mA.

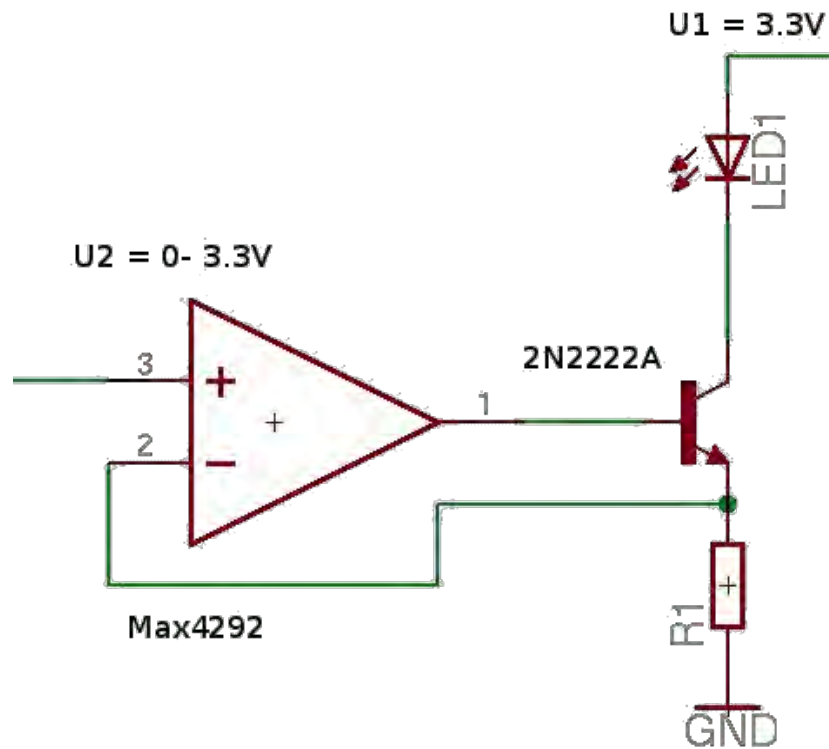


Figure 6-2: Adjustable current source

In Figure 6-3 the output fluctuation is between -0.2 and 0.4% and the averaged peak wavelength is 668nm. The output fluctuations are very small and the periodic behaviour can be caused by the internal cooling system of the spectrometer or by the current source. At the peak wavelength the output fluctuations are in a range of -0.1% to 0.1%. Figure 6-4 shows the output characteristic of the 670nm LED with a forward current of 20mA. The peak wavelength drifted from 668nm to 671nm and the power fluctuations in this at region are about +0.5%.

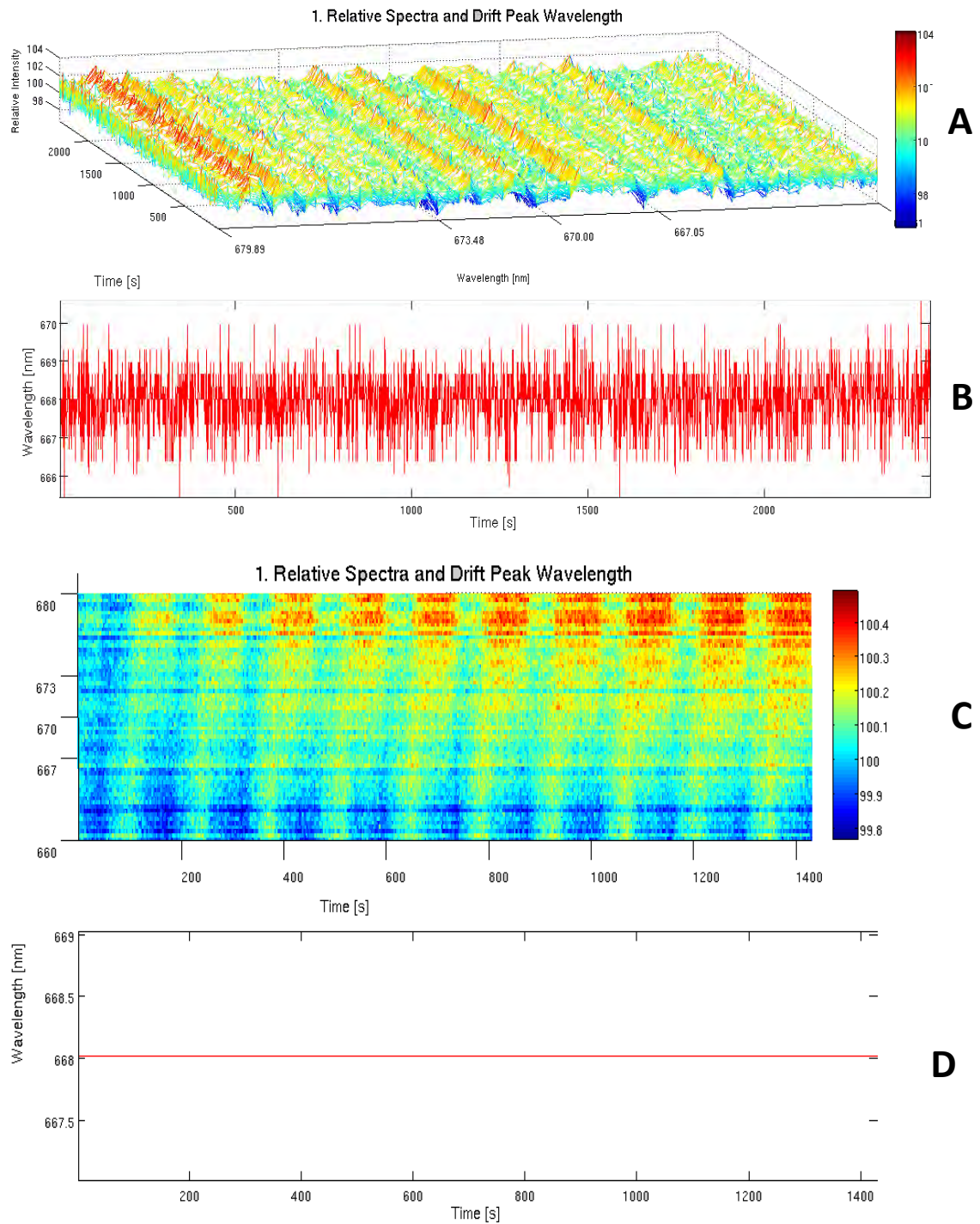


Figure 6-3: 670nm LED relative output spectra at 5mA A: raw data 660nm-680nm B: peak wavelength shift C: raw data with periodic fluctuations D: averaged wavelength shift at 668nm

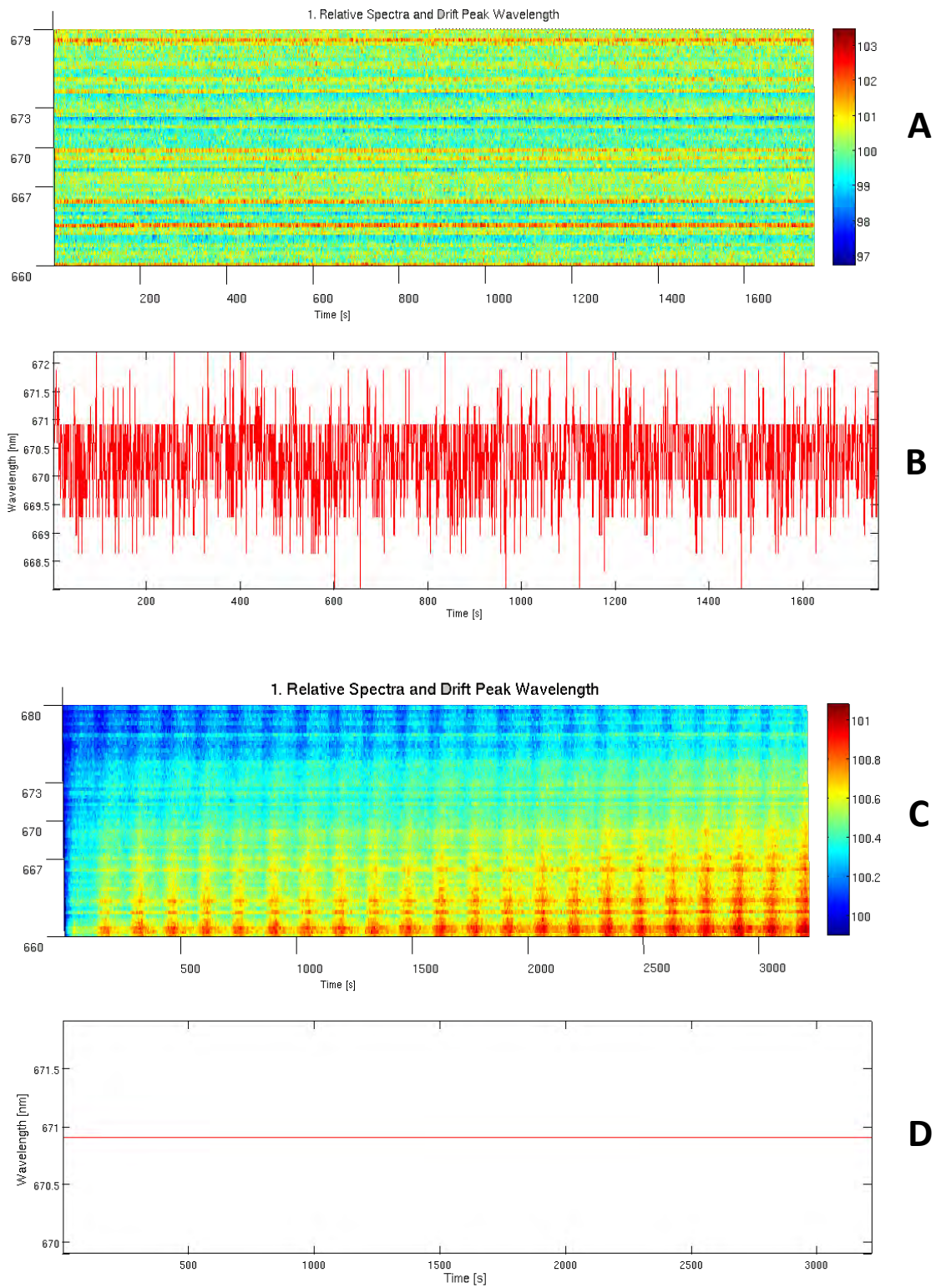


Figure 6-4: 670nm LED relative output spectra at 20mA A: raw data 660nm-680nm B: peak wavelength shift C: raw data with periodic fluctuations D: averaged wavelength shift at 671nm

Figure 6-5 and 6-6 shows the correlation between the forward current and the wavelength shift for the 810nm (ELD-810-525) and 1300nm LED (ELD-1300-525).

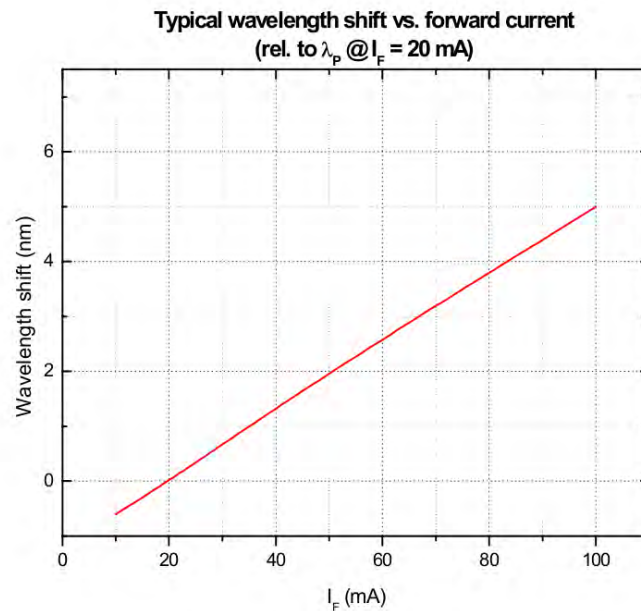


Figure 6-5: Wavelength shift 810nm LED [80]

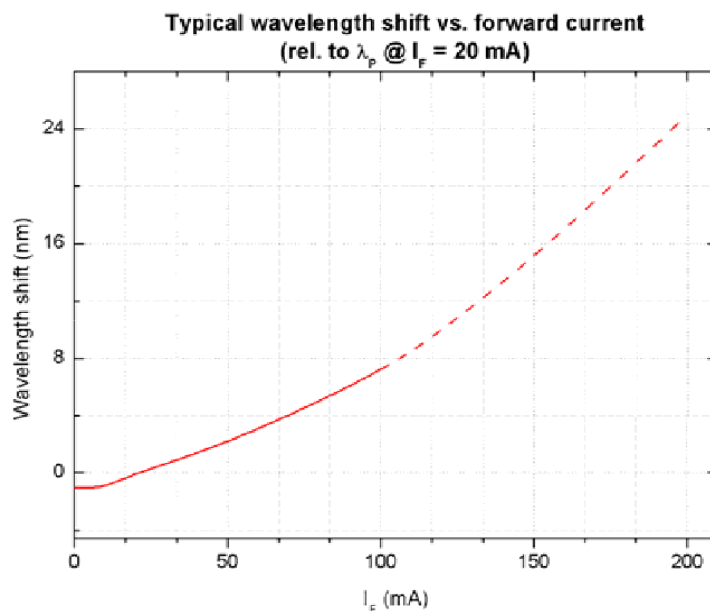


Figure 6-6: Wavelength shift 1300nm LED [80]

The pure intensity fluctuations are uncritical for the measurement system and can be ignored since there is normalisation of measured light intensity. A wavelength shift

for the 670nm and 810nm LED is in a range of -2nm and 2nm and can also be considered as insignificant as the spectra are relatively flat in these regions. The isosbestic point is in range from 800nm to 810nm and the LED would be suitable for this application. The 1300nm LED needs to be driven with a forward current of 80mA - 100mA and that can cause wavelength shifts of 6-8nm. Corresponding to the absorption spectra in figure 4-5 wavelength shifts up to 10nm greatly influence the measured absorption. Pulse oximeter manufacturers order complete series of LEDs and analyse and characterise shifting the peak wavelength and adding a calibration coefficient for wavelength shift into the calibration curve of the device. For the developing of a prototype such a procedure is not necessary and the LEDs chosen suit the application for this investigation in highly satisfactory manner.

### 6.3 The Sensor

The Haemoglobin Sensor includes the light sources, an appropriate wavelength selective optical receiver and the necessary circuits for signal conditioning and processing. All these parts are included in the finger clip housing. Due to the wide used spectral range (from 670nm up to 1300nm) the photodiode choice is an essential parameter in the design process. Figure 6-7 shows the spectral responsivity of some common photodiodes.

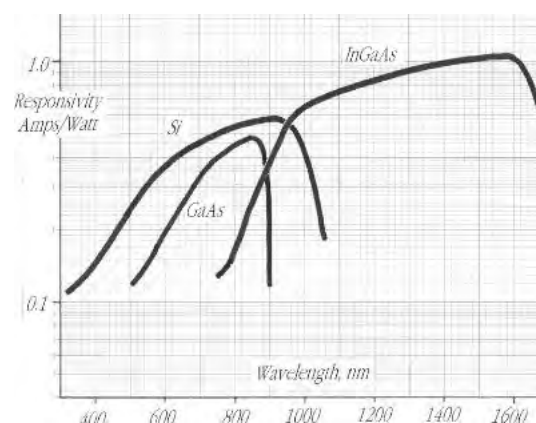


Figure 6-7: Responsivity diagram of Silicon, Gallium Arsenide and Indium Gallium Arsenide photodiodes

Figure 6-7 shows that none of the photodiodes cover the required spectral range. In such a case a sandwich detector or two separate photodiodes (Si+InGaAs) are

necessary. The advantage of the sandwich detector is that both diodes share the same surface. Therefore the same photons are incident on both detectors which propagate along the same optical path but otherwise the intensity at the lower diode is attenuated. A disadvantage in both cases is the need for two separate signal processing circuits. To avoid these problems a special coated InGaAs photodiode was chosen. To expand the spectral range into the visible area an Indium Phosphor (InP) layer was added. Figure 6-8 shows the spectral responsivity of the InGaAs/InP photodiode and the selected light sources.

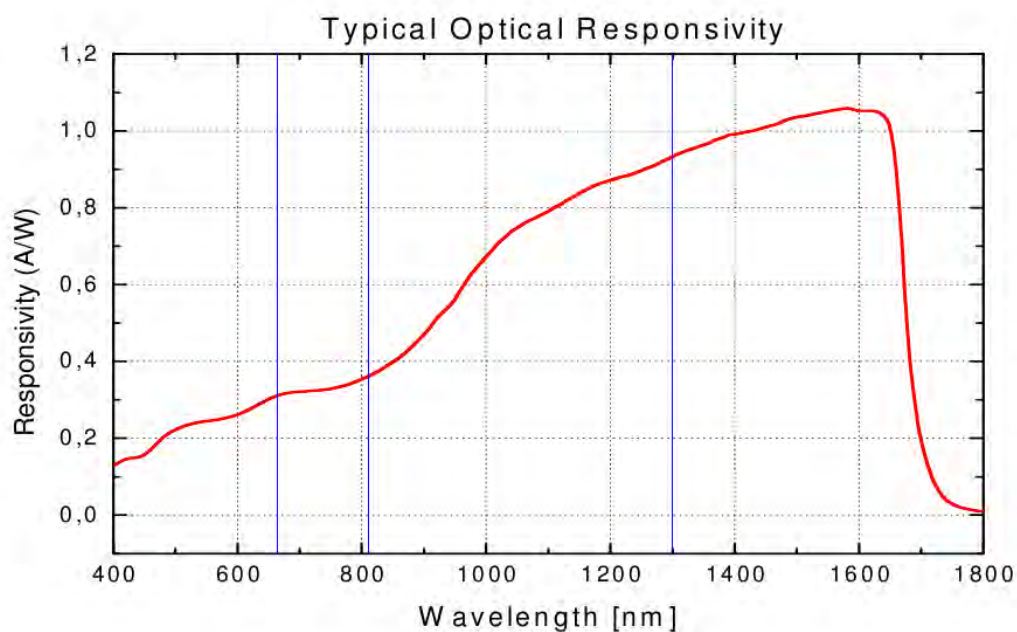


Figure 6-8: Spectral responsivity of the InGaAs/InP photodiode [80]

The selected detector surface has a size of  $0.78\text{mm}^2$  and due to the single detector design only one transimpedance amplifier and one signal processing pathway is necessary. The photodiode is housed in a two pin TO-18 housing where the cathode of the diode is connected to the housing. This constellation results in a huge disadvantage in combination with normal transimpedance amplifier stages where the photodiode is used in as spear direction. The coupling of the cathode to the inverting output of the amplifier results in a 50Hz noise caused by coupling of the 50Hz main noise through the housing to the circuit. A low pass or a notch filter can be used to remove the noise but the signal in this case the pulse wave is distorted after filtering. The final solution for this problem was to invert of the photo diode so

that the cathode with housing connection lays on ground potential and the anode is connected to the non-inverting input of the amplifier. Due to this connection it is necessary to drive the amplifier with a negative input voltage. The amplifier used was the rail to rail TI OPA381 [81] which was supplied with -3.3V on VEE and VCC is connected to ground.

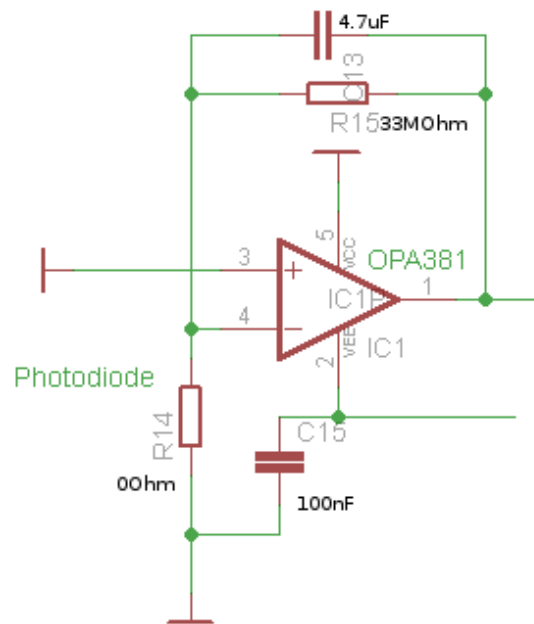


Figure 6-9: Transimpedance amplifier stage with OPA381

Figure 6-9 shows the transimpedance amplifier stage which is wholly integrated within the finger clip. In commercial SpO<sub>2</sub> devices the transimpedance stage is located inside the main device and the small photo current is transferred through the connecting wire. Figure 6-10 shows a picture of the complete finger clip.

The second generation of the finger clip includes an additional 14 bit analog digital converter (ADC), a 12 bit digital to analog converter (DAC) and a programmable amplifier. The wiring to the finger clip is a completely digital (SPI Bus) and the analog wiring is reduced to a minimum which a results in further enhancement of the signal to noise ratio.

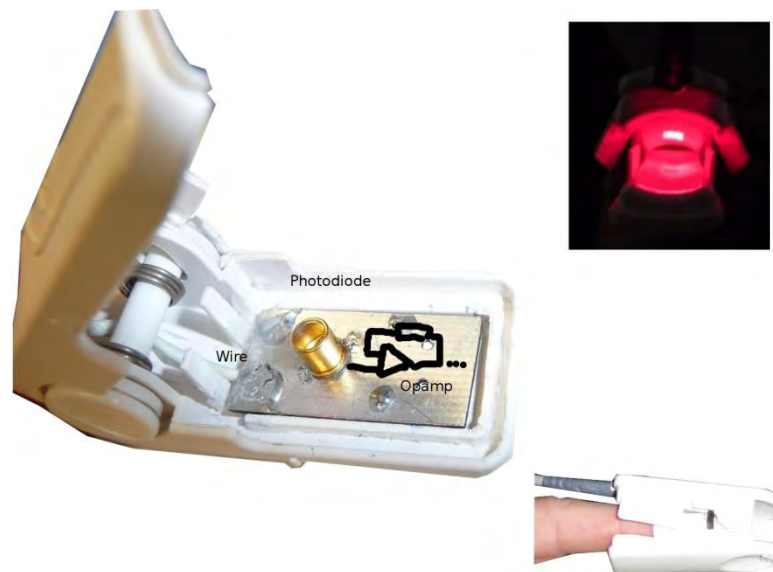


Figure 6-10: Look inside the finger clip, transimpedance amplifier mounted on the rear side of the PCB

#### 6.4 Basic Sensor System

The main system for the analog clip (figure 6-10) comprises three separate sub systems namely, the LED driver circuit, signal conditioning circuit and the microcontroller with periphery. The MSP430F1611 [82] is a 16bit RISC ultralow power microcontroller with two built-in 16-bit timers, a 12-bit ADC and two 12-bit DAC. The signal conditioning circuit consist of programmable gain amplifiers which allow a subtraction of the DC part.

Figure 6-11 shows a schematic of the sensor system of this investigation.

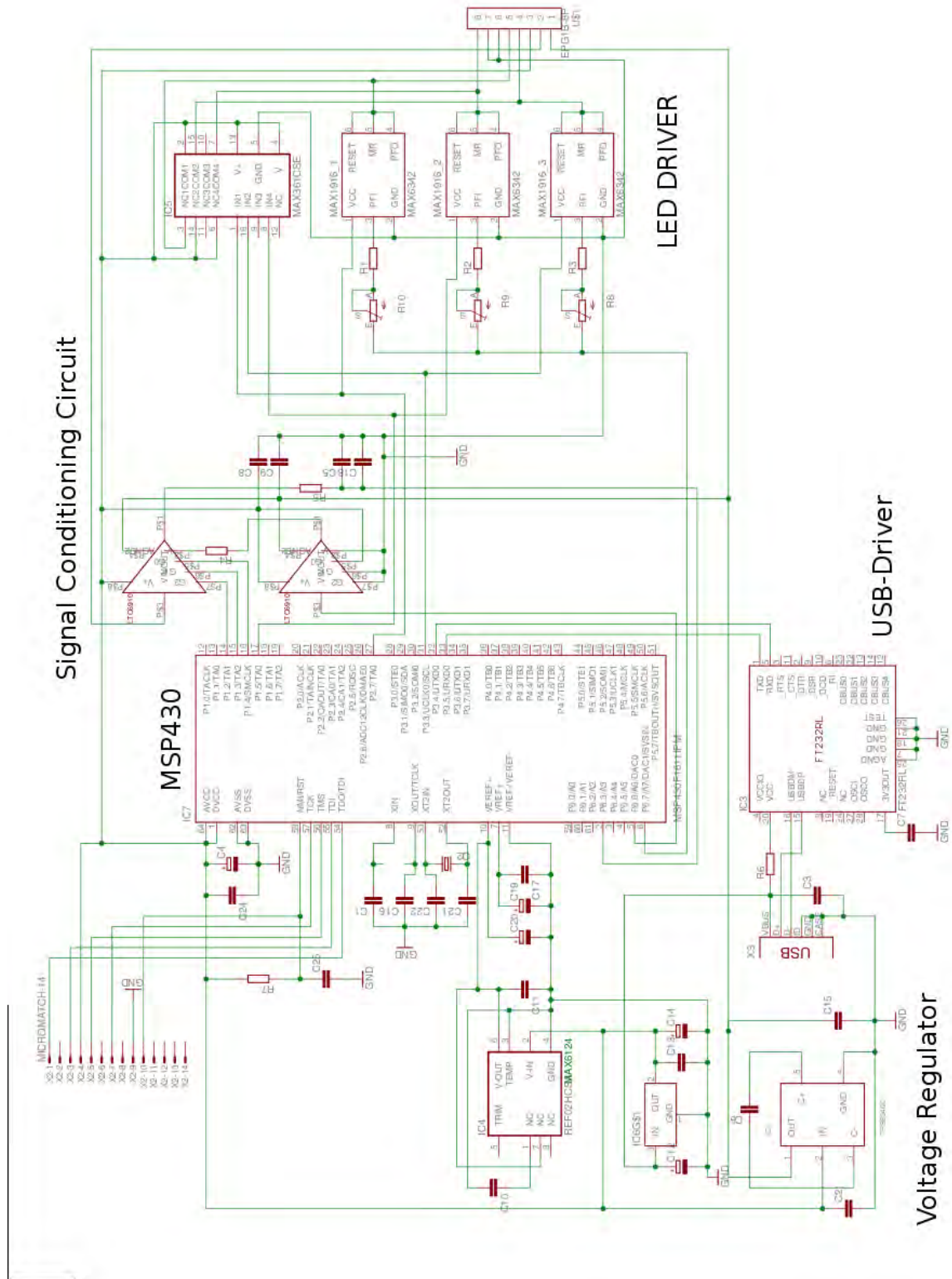


Figure 6-11: Schematic of the Sensor System

Two additional amplifier stages allow a DC part subtraction and an amplification of the left over AC part. One of the MSP430 internal 12bit DACs is used to generate the voltage for the DC subtraction. It is always possible to reconstruct the DC part by using the DAC value and considering the programmed amplification. This stage raises the SNR allows a capturing of pulse waves also in case low perfusion. Each LED Driver enables the possibility to drive a current per LED up to 160mA. After the signal conditioning circuit the final signal is sampled by the internal 12bit ADC.

The LED driver circuit consists of three separate voltage controlled current sources which are time multiplexed driven and controlled by the MSP430. Figure 6-12 shows the timing sampling and the timing diagram.

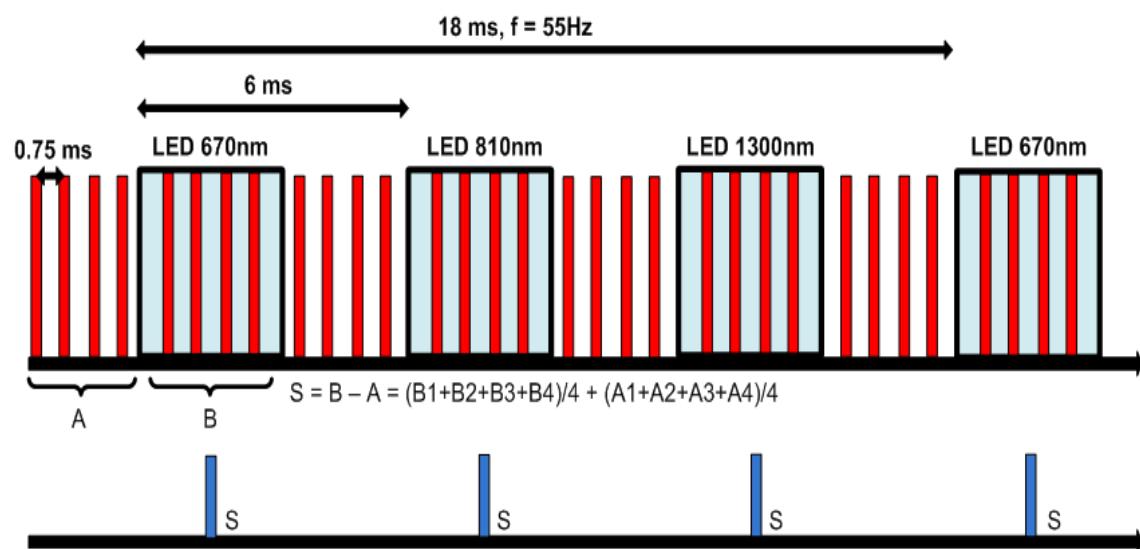


Figure 6-12: Timing Diagram MSP430

Each LED is switched on for 3ms and during this time four samples are recorded. The average of these four samples is calculated. In order to reduce the influence of the ambient light the same procedure is performed during the LED switch off time. The difference of the two values represents the sample for one LED phase and the sample frequency for each LED is around 55Hz. Finally the raw data are transmitted via an RS232 or Bluetooth interface to the measuring PC. Figure 6-13 shows the sensor system with a connected finger clip.



Figure 6-13: Hb Sensor System

## 6.5 Software

The main application was written in LabVIEW 2009 from National Instruments [83]. Figure 6-14 shows a view of the front panel. A block panel view is shown in the Appendix. To establish a communication with the device the COM-port and the communication parameters have to be selected. To improve the comfort for the user this happens full automatically. A routine of running in the background detects the ID of the FTDI USB chip and adapts the parameter. The system stores also automatically three storage files. The first one saves the whole data stream for each PPG wave in voltages and the second one in bit values from 0-4095 (12bit). The third file contains all calculated results for every buffer. The size of the buffer can be manually changed. The initial value was set to 250 and depending on the pulse rate 4-8 pulses are included in the buffer. Five pulses are recommended for the buffer. From this point the application runs completely automatically. The pulse wave at 810nm is shown in the top right window. The heart rate, SpO<sub>2</sub> and Hb are shown as numeric value in the middle and as graph on the left side. In the bottom right window the pulse wave is show in the frequency domain (wavelet transformation). In this window the pulse wave is very distinct at a pseudo frequency of around 1.1Hz which is equivalent to a hear rate of 66bpm.

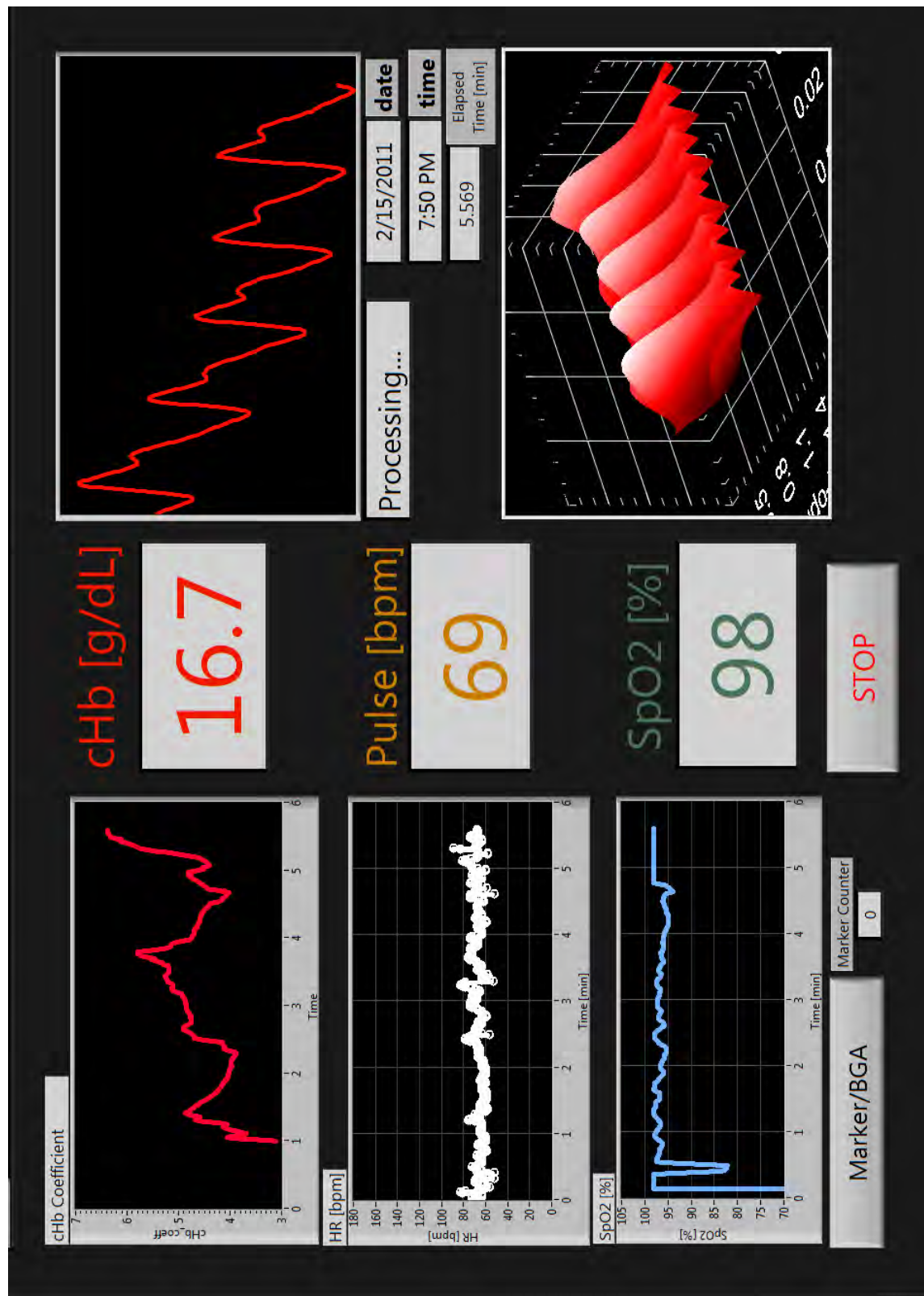


Figure 6-14: Screenshot of the Main Application

### 6.5.1 Algorithmic

Figure 6-15 shows a schematic of the used algorithm which runs continuously in the background and processing the received input buffers to usable output parameters [84].

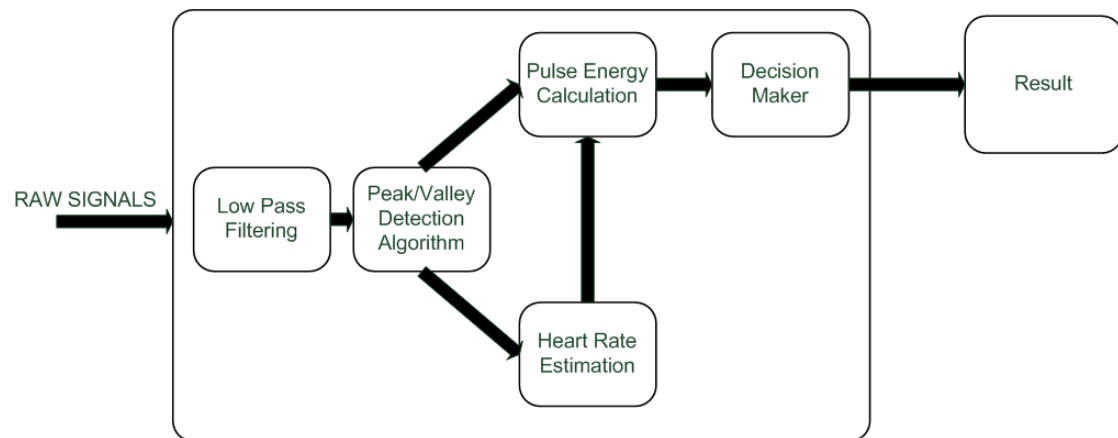


Figure 6-15: Architecture of the detection & AC/DC estimator algorithm.

At the beginning the raw signal is pre-processed by a Bessel low-pass filter with a cut-off frequency of 5 Hz. The advantage of the filter is a near - constant time delay along the frequency band which is useful when the correlation in the time domain is an important parameter. It reduces the problem of a delaying low and medium frequency and due to this fact the peaks and troughs remain relatively correlated. The next step of the pre-processing stage is digital time-delay compensation. Further in detection algorithm process the first and second derivative are formed to determine peaks and valleys of each pulse. The “4th order Central” method of the derivative extraction was used [85].

$$f'(t_n) = \frac{1}{12dt} (-x_{n+2} + 8x_{n+1} - 8x_{n-1} + x_{n-2}) \quad (6.2)$$

Thereby  $n$  is the number of samples in  $f(t)$ . The general problems with the peaks and troughs determination are caused by the individual physiological conditions of the patients. Among the potential problems are dirotic notches and motion artefacts

(external, muscles etc.). Generally, in all cases a sophisticated decision logic and algorithm is needed which relies on an extensive database of real patient data. The peak/valley detection algorithm is shown in Figure 6-16 in order to separate peaks and valleys from diastolic notches.

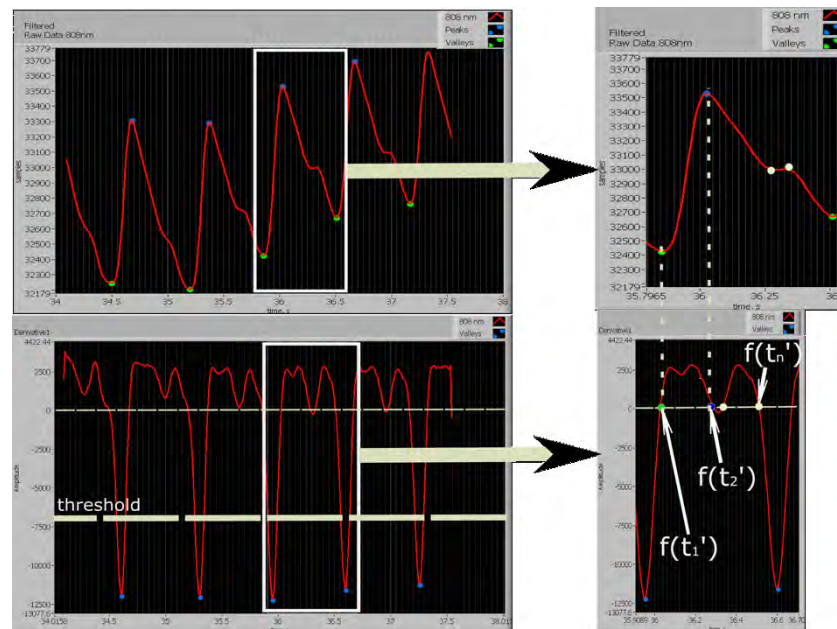


Figure 6-16 Peak/Valley algorithm

A threshold for the first derivative transformation of the original data was set to identify the troughs. Further it is possible to generate a buffer filled with the local extremums which are located between the identified valleys. The peak detection is executed in several phases. First all extremums  $f'(t_n)$  in the first derivative buffer are detected. Then the second derivatives  $f''(t_n)$  of the founded global extremums are composed to prove the peak/valley conditions. A major advantage of the derivative method compared to the other techniques is a lack of a DC-level drift [86]. This drift is present in the time domain and causes difficulties with the proper threshold settings, especially in critical cases of deoxygenation. The pulse wise analysis is more precise in case of the pulse rate calculation comparing to the FFT-based techniques where the fundamental frequency is a sum of all frequency components of a time buffer. After valid peaks/valley detection it is feasible to calculate the energy of every pulse which is mathematically the square of the sample points under the curve. It allows the inclusion of the complete pulse waveform information located

between the two predetermined troughs. The estimation of the blood components are only possible once per heart beat/pulse. This new approach to use the whole information accumulated in a single beat by taking its energy as variable AC and the area under the constant baseline as DC value makes the algorithm more robust than the traditionally used AC/DC peak ratio calculation.

#### 6.5.1.1 Validation of the Algorithm

Raw data from patients were stored during dialysis sessions. An ethical approval was given by the University of Rostock Ethic Commission. The study was done in cooperation with nephrology station of the University of Rostock. The measuring set-up is shown in Figure 6-17.

There are two basic groups of PPG pulse wave artefacts: physiological and those induced by the measuring system. Ones which belong to the second group rely strongly on the sensor circuit and hardware design. They can be efficiently minimized by a proper design, sensor shielding and digital filtering of the raw data. Reasons for the physiological artefacts can differ. These include motion, caused by venous blood and other non-pulsatile components movement [87], problems with the cardiovascular system, as well as poor peripheral blood circulation (e.g. angiopathic diabetic patients).

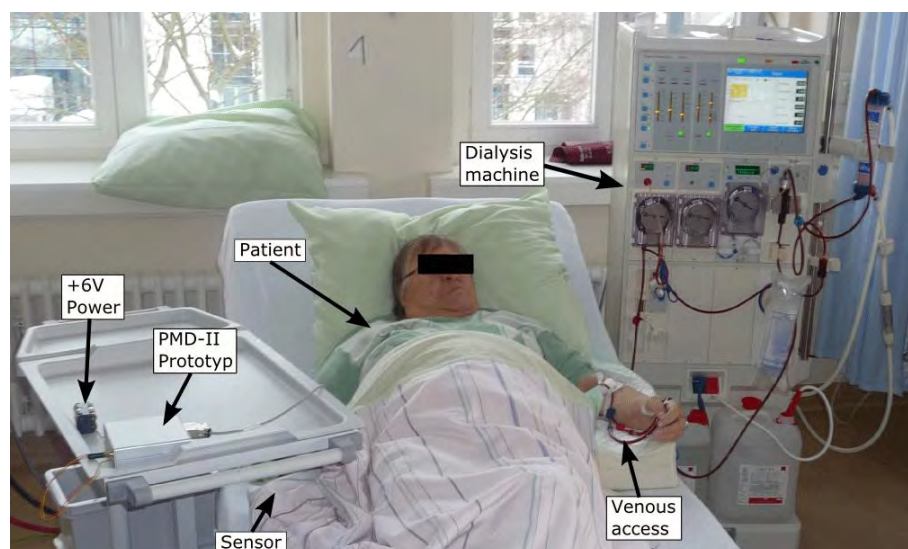


Figure 6-17: Measuring set-up during dialysis session

Two AC/DC ratio detection algorithms, peak-to-peak and the novel pulse energy techniques are compared for three different situations (Table 4).

Patient state	SpO <sub>2</sub> , %	Time [min]	Features
Normal/ deoxygenation	95-75	18.2	- fast varying SpO <sub>2</sub> value - DC level drift
Decease I/ diabetic angeopathy	97	4.1	- relatively stable SpO <sub>2</sub> value
Decease II/ pacemaker	97	8.4	- corrupted PPG - hard to identify a single heart stroke

Table 4: Initial condition for three data sets for the algorithm validation

Figure 6-17 to 6-19 shows a comparison of both algorithms the common pulse oximeter wavelength 670nm and 905nm and table 5 reports the parameter of the statistical distribution (median and standard deviation from median).

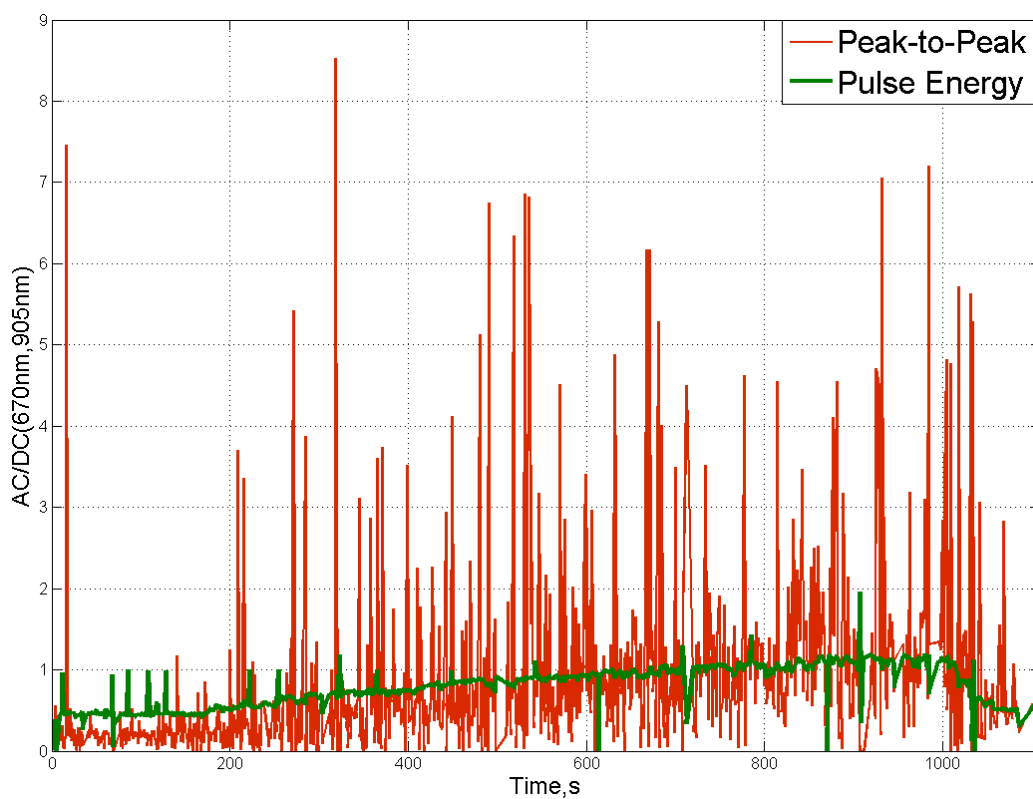


Figure 6-18: AC/DC calculation. Patient state: normal/deoxygenation.

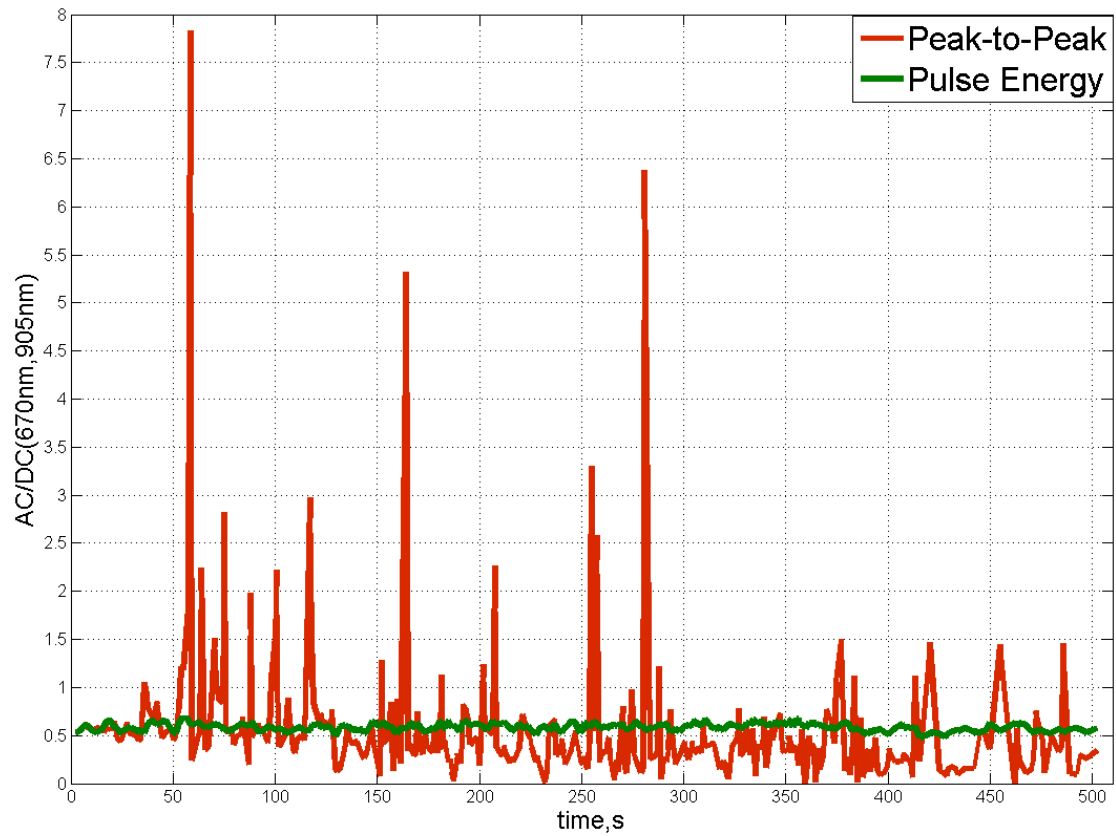


Figure 6-19: AC/DC calculation. Patient state: pacemaker

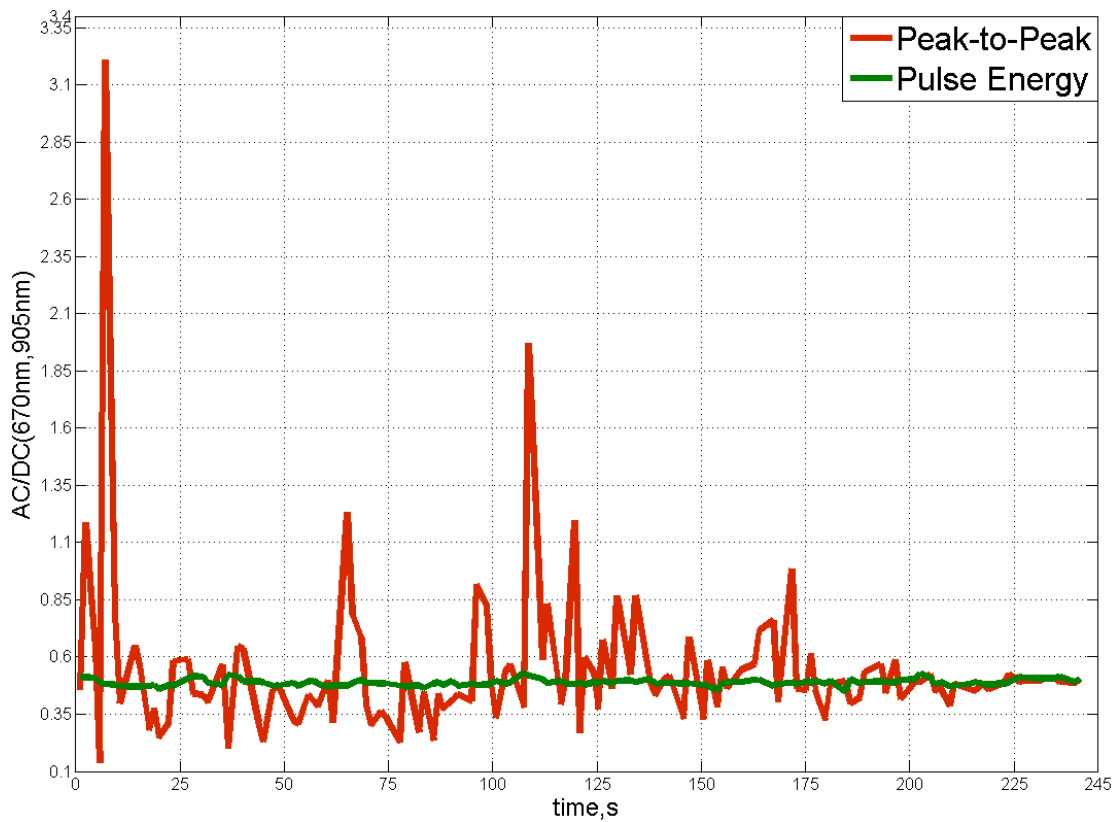


Figure 6-20: AC/DC calculation. Patient state: diabetic angeopathy

Patient state	Algorithm	Median	Max SD	Kurtosis
Normal/Deoxygenation	Peak to Peak	0.17-1.53	7.83	17.89
	Pulse Energy	0.2-1.12	0.86	2.55
Pacemaker	Peak to Peak	0.42	7.41	50.75
	Pulse Energy	0.59	0.1	2.41
Diabetic Angeopathy	Peak to Peak	0.48	2.73	37.42
	Pulse Energy	0.49	0.05	3.52

Table 5: Statistical Distribution of the Peak to Peak and Pulse Energy algorithm

The results of table 5 show that the novel algorithm using the pulse energy for the *AC/DC* ratio estimation is superior in comparison to the standard method. The algorithm does not depend on the buffer length and does not require a setting of a specific threshold for the peak and valley detection, which might cause some limitations in accuracy. The novel algorithm is computationally efficient and ready to use for real-time measuring applications. The whole analysis is realised in the time domain and for this reason the algorithm is also well suited to slower embedded platforms.

## 6.6 Summary

This chapter gives a detailed description of the MSP430 based sensors system and the used components for the non-invasive Hb measurement. The LEDs as suitable light source and a broadband photodiode are used in the sensor head. A new algorithm for peak detection is presented as well the clinical validation.

## 7 Validation with the blood flow model

### 7.1 Introduction

The *in vitro* validation of the haemoglobin measurement method was conducted on an artificial blood flow model. The advantage of using such a system is the possibility to change each of the process parameters independently. Additionally spectrometer measurements are possible to review the literature data which presented in chapter 4.3. In particular the position of the isosbestic point and the influence on the haemoglobin concentration can be independently investigated.

### 7.2 The Blood Flow Model

Based on the human circulatory system a blood flow model was developed which is necessary for the validation of the haemoglobin concentration results and the above described optical sensor system. With the help of the model a controlled variation of the haemoglobin concentration and oxygen saturation are possible. Therefore both parameters can be changed separately or simultaneously. Non circulating blood is not a representative typical physiological condition as in reality blood does stagnate into the tissue. Therefore a setup for optical measurements on flowing blood is necessary. By using a circulation system based on a roller pump the blood is circulated through the closed circuit and also a pulsing blood volume is generated (0-200 ml/min). The schematic diagram of the system is shown in Figure 7-1. A blood reservoir a common blood bag from the blood donation was used. The bag is submerged in 36°C -37°C tempered water to simulate the human blood temperature. An additional tube heater is also used to maintain this temperature at a stable level. The blood plasma and erythrocyte concentrate can be externally added at the input valve. The mixture ratio of them gives the required haemoglobin concentration.

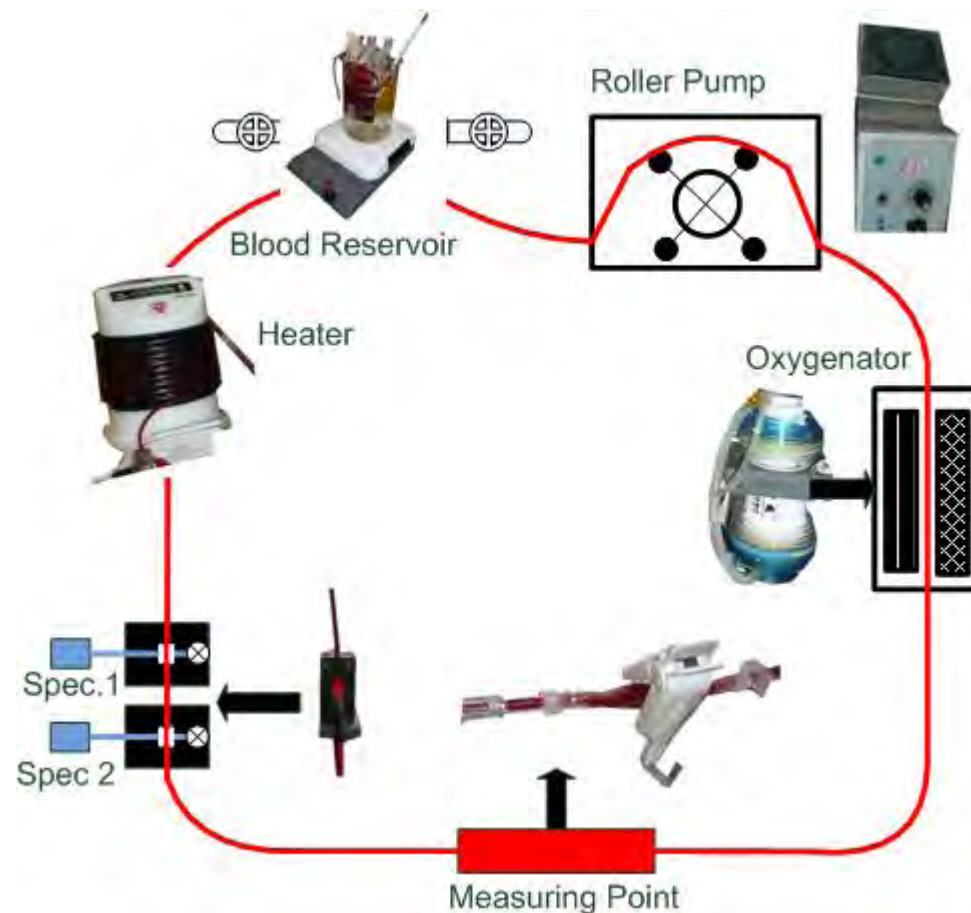


Figure 7-1: Setup Blood Flow Model

The input point is at the same time the blood sample extraction point. The blood gassing takes place in the oxygenator which allows the precisely controlled introduction of oxygen and nitrogen. As oxygenator the DIDEKO Lilliput D901 with a membrane surface of  $0.34\text{m}^2$  was used. To oxygenate the blood a nitrogen-oxygen mixture (70:30) is used with a maximum flow rate of 3 l/min. Two optical cuvettes with an optical path length of 5mm are included in the circuit to facilitate the spectrometer measurements. Both spectrometers are necessary to capture the spectral range from 600nm-1700nm. The sensor head is clipped on an enlarging section of the blood tube.

### 7.3 Spectrometer Measurements

To analyse a spectral range from 600nm to 1700nm the spectrometers Avantes AvaSpec 2048x14 and the Jeti VS 140 were used. The Avantes AvaSpec has a spectral

range from 200nm to 850nm while the Jeti VS140 NIR has a spectral range from 800nm to 1700nm. A white light halogen lamp was used as the optical source. The light is transmitted across a 5mm thick cuvette before it reaches the spectrometer. First the light source spectrum was captured which was later subtracted from all measurements. The blood was analysed with the blood gas analyser ABL System 625 from Radiometer. Figure 7-2 shows the recorded blood transmission spectrum with an oxygen variation from 14% to 96%.

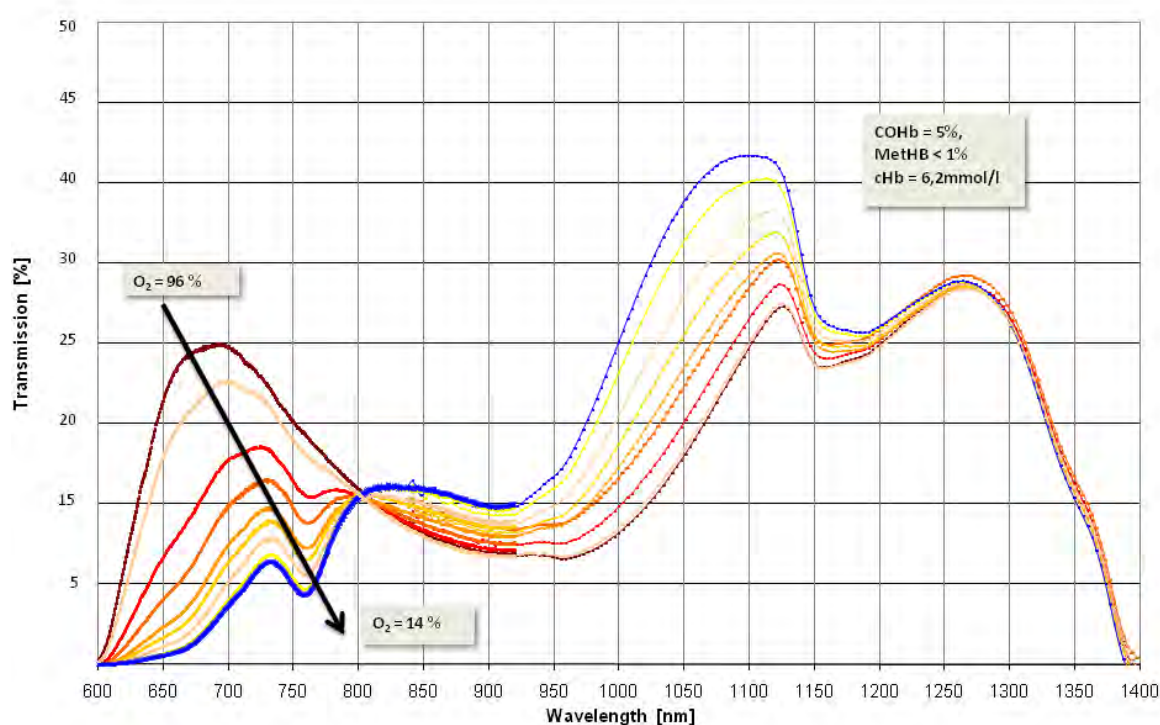


Figure 7-2: Blood spectrum from 600nm to 1400nm in dependence to the oxygen saturation

The difference between the extinction coefficient of HHb and HbO<sub>2</sub> is larger below 800nm than above. The isosbestic point which is independent of the oxygenation is located between 800nm and 810nm. Up to 1150nm the spectrum shows oxygen dependence which gets smaller and nearly disappears from 1200nm. The measurement confirms that the chosen wavelength at 1300nm is not influenced by the oxygen saturation.

In addition to the oxygen variation, the haemoglobin concentration was changed between 8.5mmol/l and 3.3mmol/l. The corresponding absorption spectrum is shown in figure 7-3.

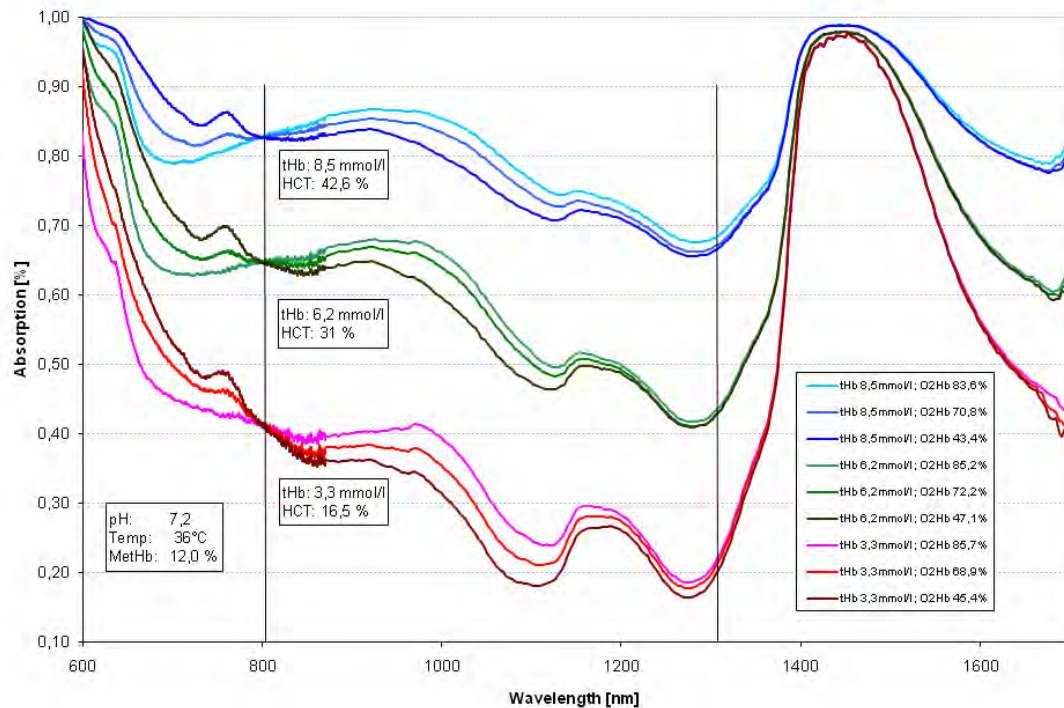


Figure 7-3: Absorption spectrum of blood from 600nm to 1700nm in dependence to the oxygen saturation and haemoglobin concentration

The total absorbance of the blood across all measured wavelength rises with an increase of the haemoglobin level. As in the previous measurements the isosbestic point is still between 800nm and 810nm and the absorption does not change with the oxygen concentration. Above 1200nm the absorption spectrum follows the water absorption as simulated in Figure 4-5. Thus the chosen wavelength of 1300nm is an optimal oxygen independent measuring position for the non-invasive haemoglobin determination. The peak around 1450nm is the characteristic water absorption peak [54]. The spectrometer measurements therefore confirm the assumptions made in chapter 5.2.

#### 7.4 Hemocue vs BGA

The handheld device HemoCue Hb 201+ from Mallinckrodt Medical [88 ]was used for the *in vivo* validation of the non-invasive haemoglobin sensor system. During the measurements on the blood flow model the HemoCue was also used to measure the haemoglobin concentration. Figure 6-4 shows the comparison of fifty test samples using the Radiometer ABL625 and the HemoCue Hb 201+.

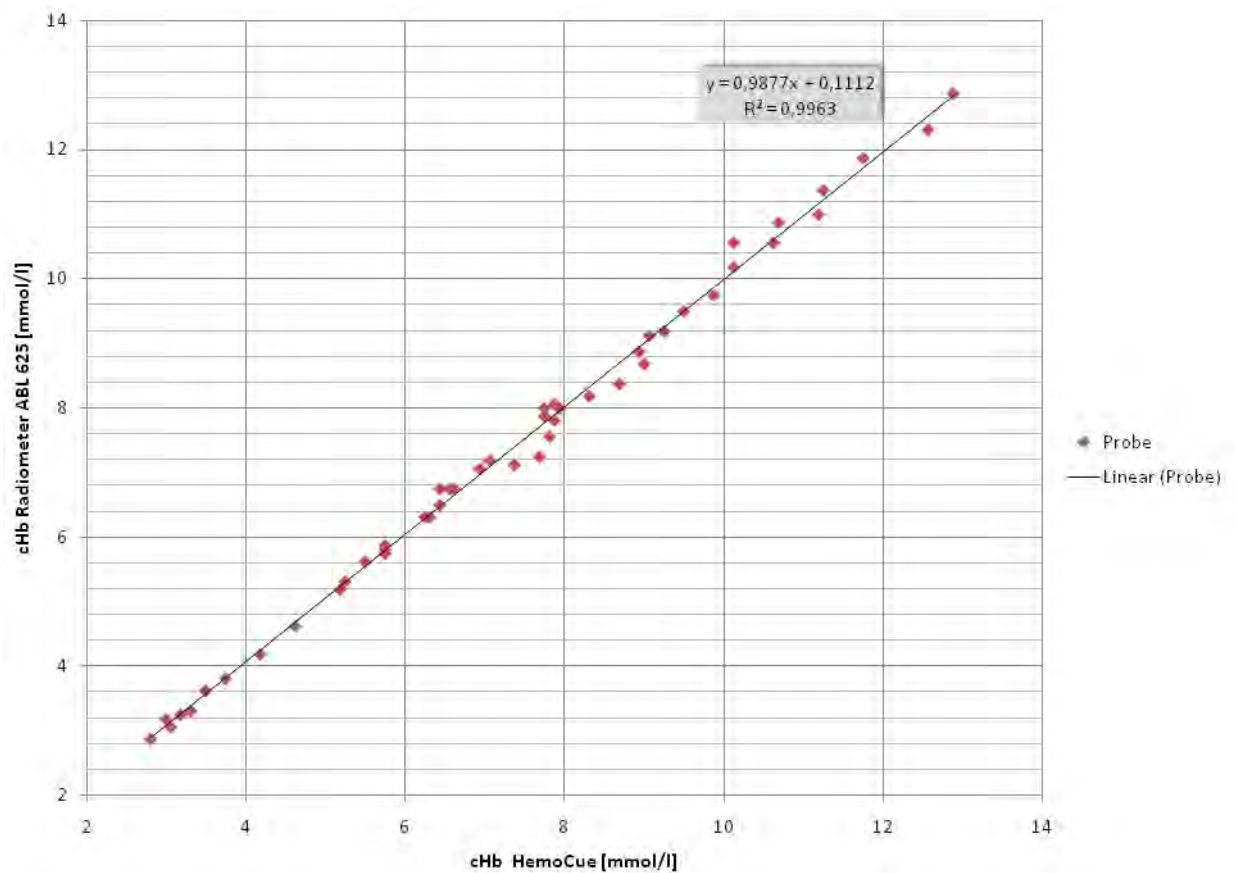


Figure 7-4: Comparison HemCue and Blood Gas Analyser

The coefficient of determination  $R^2 = 0.9963$  is high and for this reason the HemoCue is an excellent choice as reference for the non- invasive haemoglobin sensor system.

### 7.5 Blood flow model measurement with the non –invasive haemoglobin sensor system

To enable the possibility to measure with the non-invasive haemoglobin sensor system an elastic piece of tube with the shape of a pillow was integrated in the blood flow model (Figure 7-1 at the measuring point). The finger clip was clipped on the pillow and physically fixed to prevent a shifting. During the measurement all data were stored in sample blocks of all three wavelengths plus time stamp with a sample frequency of 55Hz. As in case of the spectrometer measurements the oxygen saturation and the haemoglobin concentration were changed. The usage of the pulse energy algorithm (6.4.1) is possible in this case due to the pulsating shift which is comparable to the body's pulse wave. During the measurements the pump rotating speed was set from 30 up to 40 rpm (pulse frequency of 60 to 80) to prevent a settling out of the erythrocytes. The mechanical vibration originating from the massive pump interfered with the measurement and distorted the pulse forms. This was determined by analysing only with DC part of the PPG waveform. A disadvantage is that the measurement series are not quantitatively comparable against each other. However this not important for the validation of the measuring method themselves because the optical path length is constant and a functional demonstration is possible. Figure 7-5 shows the small section of raw date during the measurement at the blood flow model to point out the corrupted pulse waves.

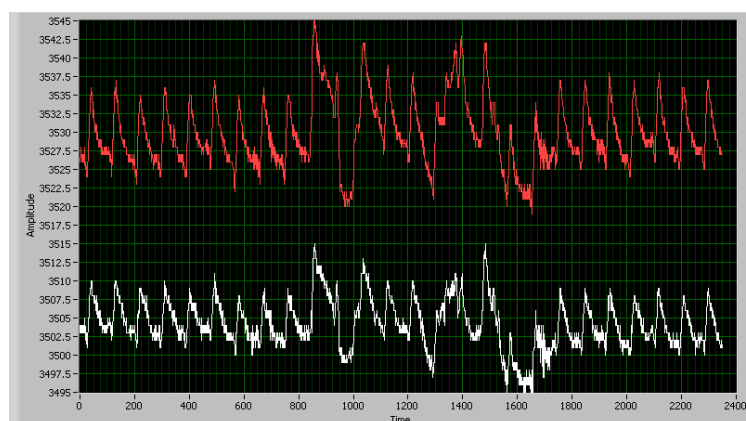


Figure 7-5: Corrupted pulse waves during blood flow model measurements

The amplitude of the presented AC part is around 5 digits which is equal to 3.05mV. That emphasizes again the high accuracy of the sensor system. Figure 7-6 shows the DC component of all three used wavelengths and both calculates ratios while the oxygen saturation was changed.

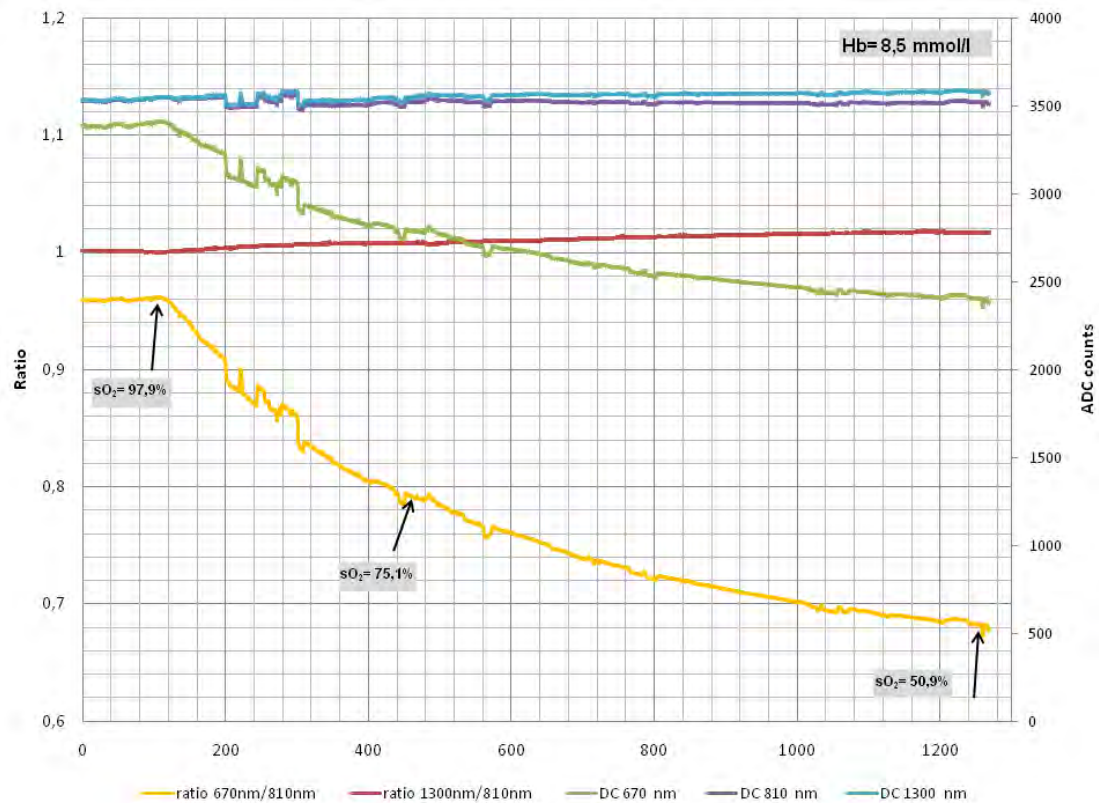


Figure 7-6: Transmission signals of the non-invasive haemoglobin sensor system and calculated ratios during a de-oxygenation ( $sO_2=97.9\%$  down to  $sO_2=50.9\%$ ,  $cHb=8.5\text{mmol/l}$ )

During the measurement the DC components of 810nm and 1300nm remain constant as expected because they are not dependent on the oxygen saturation in opposition to the DC component of the 670nm wavelength. The ratio 1300nm/810nm ratio represents the haemoglobin concentration and changes from 1 to 1.02 which is relatively insignificant. Firstly the  $SpO_2$  change is physiological untypical being very large and secondly the power input of the LED was highly increased to 160mA in comparison to the normal operating range with finger measurement of 5mA to 20mA. That increase was necessary to transmit through the thicker absorber layer blood. The increase also causes a wavelength shift into the direction of higher wavelengths which makes the measurement more  $SpO_2$  sensitive

(Figure 7-5). The ratio at an oxygen saturation of 75.1% corresponds to an increase in same ratio of 0.01 in comparison to the value at 97.9%. After analysing the measurement it can be ascertained that the ratio measured wavelengths of 1300nm and 810nm does not depend on the oxygen saturation.

The change of the 670nm and 810nm ratio shows the expected correlation to the oxygen saturation which is caused in the absorption change of the reduced haemoglobin at 670nm.

A second measurement is pictured in figure 7-7 where the haemoglobin concentration was changed stepwise from 8.5mmol/l down to 2.4mmol/l and after that the oxygen saturation was raised. The dilution of the haemoglobin was realised by adding of blood plasma to the erythrocytes.

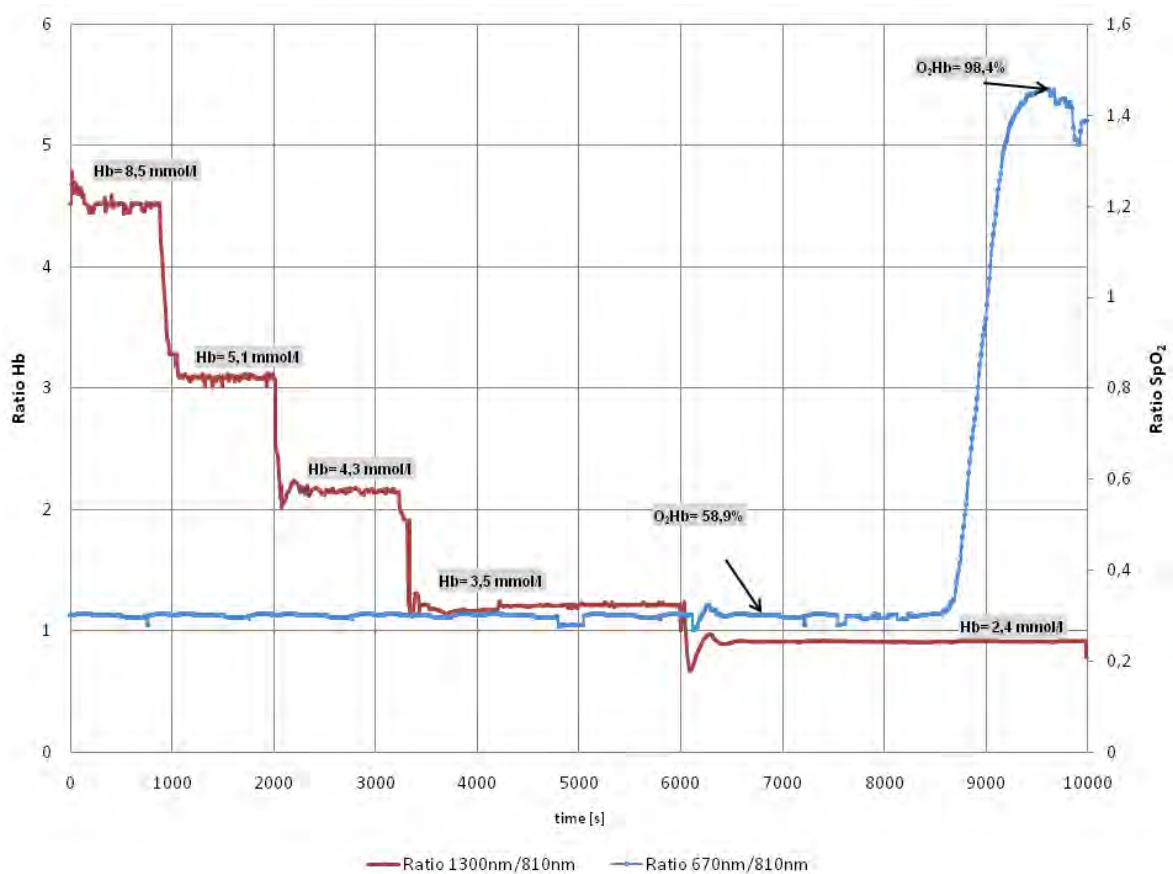


Figure 7-7: Calculated ratios during stepwise cHb change and oxygenation

The test commenced with the Hb concentration at 8.5mmol/l and the oxygen level was kept constant at 59%. The haemoglobin concentration was reduced in three steps down to 2.5mmol/l which is reflected in the calculated 1300nm/810nm ratio.

At each plateau the blood gas analyser Hb values also recorded. During the cHb changing the 670nm/810nm ratio was stable and indicated that the oxygen level was also constant. As the haemoglobin concentration reaches the lowest point, the oxygen saturation was increased from 59% up to 98%. It is a very important fact that both ratios are not influenced by each other.

## **7.6 Summary**

The theoretical foundations made in chapter 5 are fully confirmed by this experiment. As result obtained from the blood flow measurement it can be validated that a haemoglobin concentration is represented by the 1300nm/810nm ratio. A calibration curve obtained from the blood flow model is not usable for measurements in humans caused by the missing absorber layers (e.g.dermis) but the used method outlined in this investigation is suitable for a cHb determination in the blood donation. The next chapter will describe *in vivo* measurements to validate the presented technique.

## 8 Online Measurements *in vivo*

### 8.1 Introduction

After the successful *in vitro* validation of the non-invasive haemoglobin measurement method through the use of a blood flow model, an *in vivo* validation was undertaken. In contrast to the DC method previously used, the pulse energy algorithm need to be applied to obtain comparable data sets. (The pulse energy algorithm was presented in Chapter 6).

The development process for the non-invasive haemoglobin device required the formulation of a calibration curve for a correct interpretation of the calculated parameters in order to accurately determine haemoglobin concentration. In order to obtain a valid calibration curve, a comparison to an invasive reference was necessary. For this purpose the handheld device HemoCue was used, as illustrated in Figure 8-1. A comparison of the HemoCue Hb 201+ Hb measurement with a blood gas analyser was presented in Section 6.3.



Figure 8-1: Hb reference device HemoCue Hb 201+ with cuvette

The calibration study took place in Graduate Medical School of the University of Limerick. An ethical approval was confirmed by the University of Limerick Ethic Commission. A copy is of the confirmation is attached in the appendix. Each test person (subject) was monitored for around 10min with the non-invasive Hb sensor

system and all raw data of the three wavelengths were stored on the measuring PC. A section a raw data stream is shown in figure 8-2. During test motion was avoided and the finger clip was shielded from ambient light sources using an opaque fabric pouch and placed on the index finger of the left or right hand of the subject. Additionally, at the beginning of each sampling procedure, a spot measurement with the pulse oximeter Rad 5 from Masimo was conducted [89]. After taking the raw data a blood sample of the index finger was taken and analysed with HemoCue.

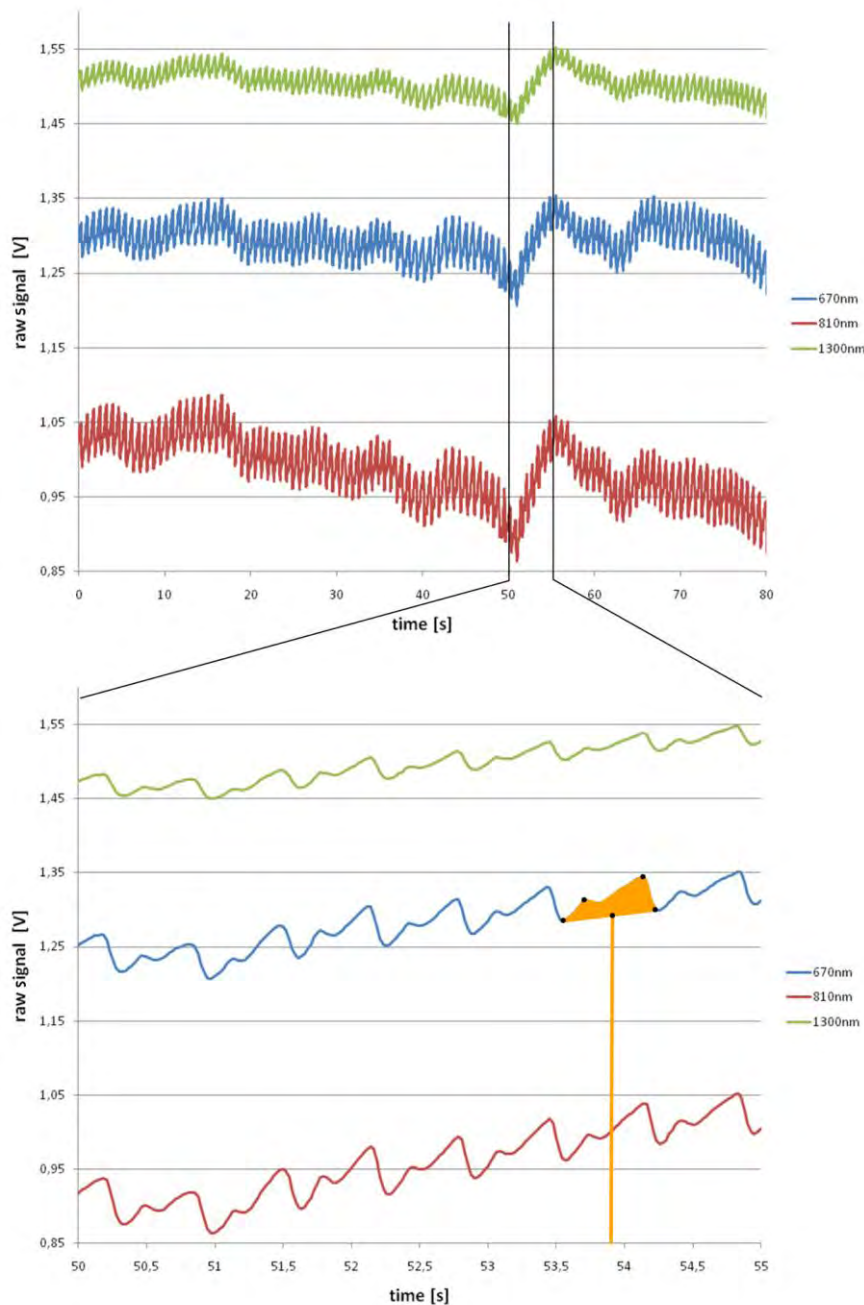


Figure 8-2: Raw PPG signals from a measurement using the non-invasive Hb finger clip probe during the calibration study

The pulse waves for all three wavelengths are shown in Figure 8-2, while the pulse energy and DC compound are highlighted in orange. A buffer of 250 samples was chosen which corresponds to approximately five pulses. For each buffer the 670nm/810nm and 1300nm/810nm ratios were calculated and stored. The raw data were stored in a separate file. Figure 8-3 illustrated an eighty second section of a measurement and the corresponding calculated ratios.

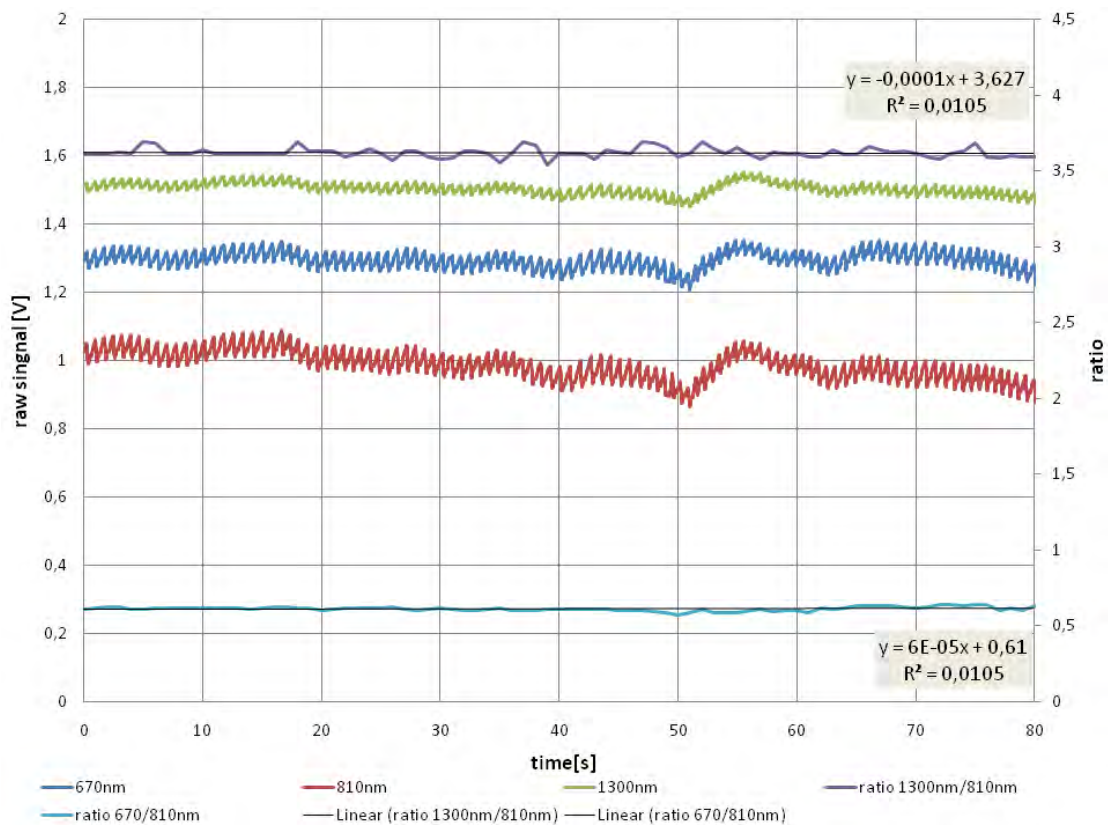


Figure 8-8-3: Raw signals and corresponding ratios for SpO<sub>2</sub> and cHb

As anticipated the 1300nm/810nm and the 670nm/810nm ratio are stable over the entire duration of the test. That means that the oxygen saturation and the haemoglobin concentration have not changed. The HemoCue was used as the cHb reference and gave a result of 9.9mmol/l, while the Masimo Rad 5 was stable at 98%. These values correspond to an average cHb ratio of 3.6 and a SpO<sub>2</sub> ratio of 0.6. By measuring a group of male and female subjects, a large variation in the haemoglobin concentration could be expected (Table1). By analysing the calculating the correlation ratios in comparison to the invasive probe, a calibration curve was

deduced. The SpO<sub>2</sub> level for healthy people lies in a small range from 95%-99% and therefore a calibration for the 670nm/810nm ratio would not reveal much information. A controlled change of the oxygen saturation is necessary in order to assess the physiologically important range from 75% up to 100%. This was not within scope of this research and remains open for further research.

## 8.2 The calibration curve

Figure 8-4 shows the comparison of 27 measurements for the 1300nm/810nm ratio with the reference device HemoCue. With this data a regression analysis was possible, which allows a prediction of the haemoglobin concentration using the calculated coefficient from the non-invasive haemoglobin sensor system.

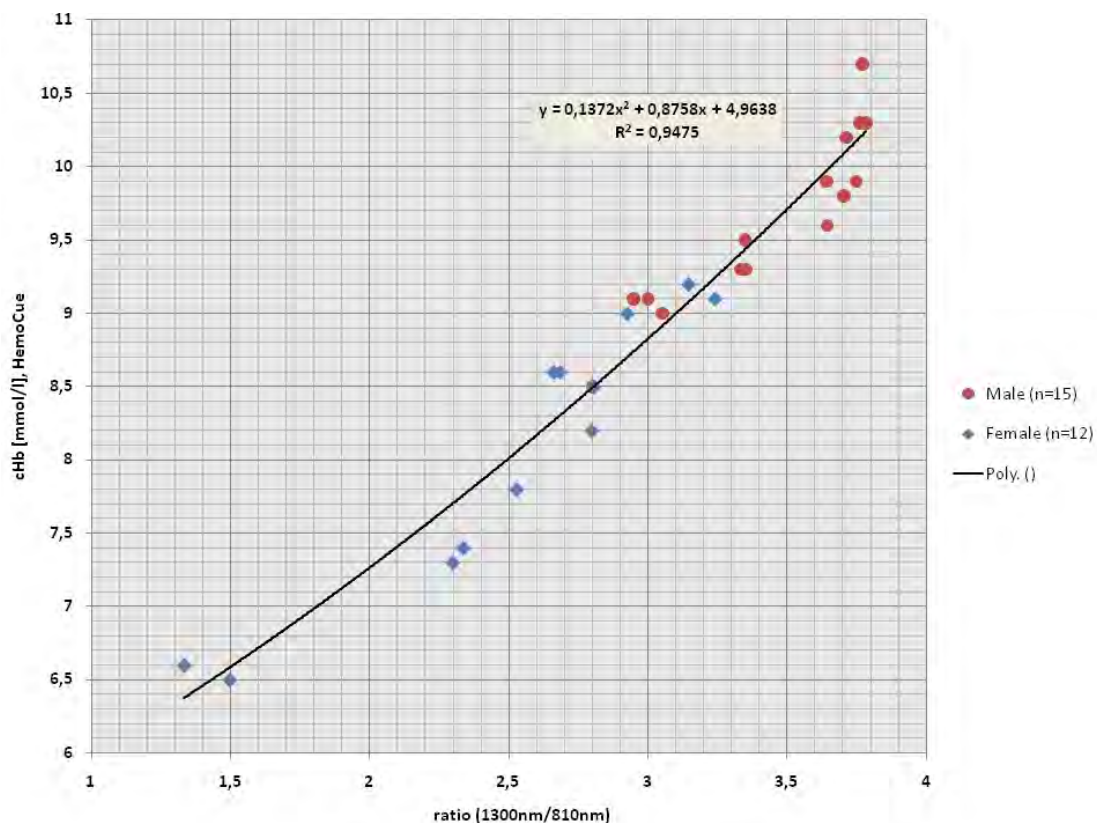


Figure 8-4: Comparison 1300nm/810nm ratio with the invasive measured value from HemoCue

By using the function obtained from the regression analysis the haemoglobin concentration was determined non-invasively with the 1300nm/810nm ratio (x):

$$cHb = 0.1372 x^2 + 0.8758 x + 4.9638 \quad (8.1)$$

In addition it was observed that eight of the primary thirty five measurements were invalid and could not be included in the calibration curve. This was due to the design of the finger clip used in the noninvasive device. The photodiode in the finger clip is located inside a metal cylinder, which in some cases applied too high a contact pressure to the finger. This effect is also known of in pulse oximetry, where the externally applied pressure distorts the real SpO<sub>2</sub> value, as explained in the following discussion both regression curves in figure 8-5 have in intersection point at around 95%. Therefore, in the normal SpO<sub>2</sub> range (> 95%) an underestimation is to be expected.

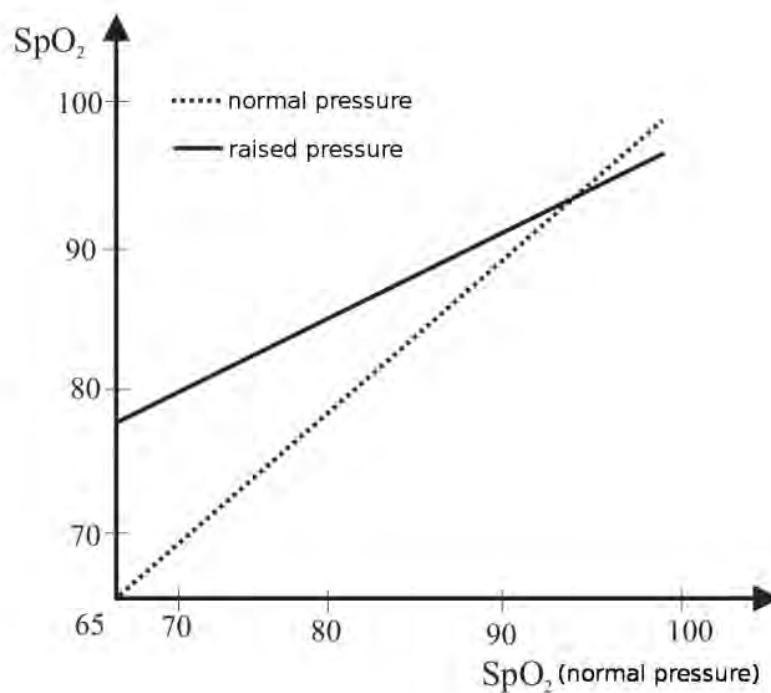


Figure 8-5: Influence of the contact pressure in pulse oximetry [90]

The reason for this effect is that the mechanical deformation of the tissue will result in a reduction of the optical pathway and a reduction of the blood perfusion [90]. The same effect is shown in figure 8-6 where higher pressure was applied for 170 seconds. After 170 seconds the finger clip was readjusted on another finger. In the first 170 second section of figure 8-6, with the pressure raised, the SpO<sub>2</sub> ratio was less and the cHb ratio was much higher than in the time section with normal

pressure. This result can be repeated to prove its validity. An explanation for the large change in the cHb ratio, can be attributed to the squeezing out of water from the finger tissues, and this excess water is as a result included in the measurement at 1300nm. However, under normal conditions with a correctly sized finger clip, when the pressure on the finger is not excessive then both ratios revert back to a plausible level.

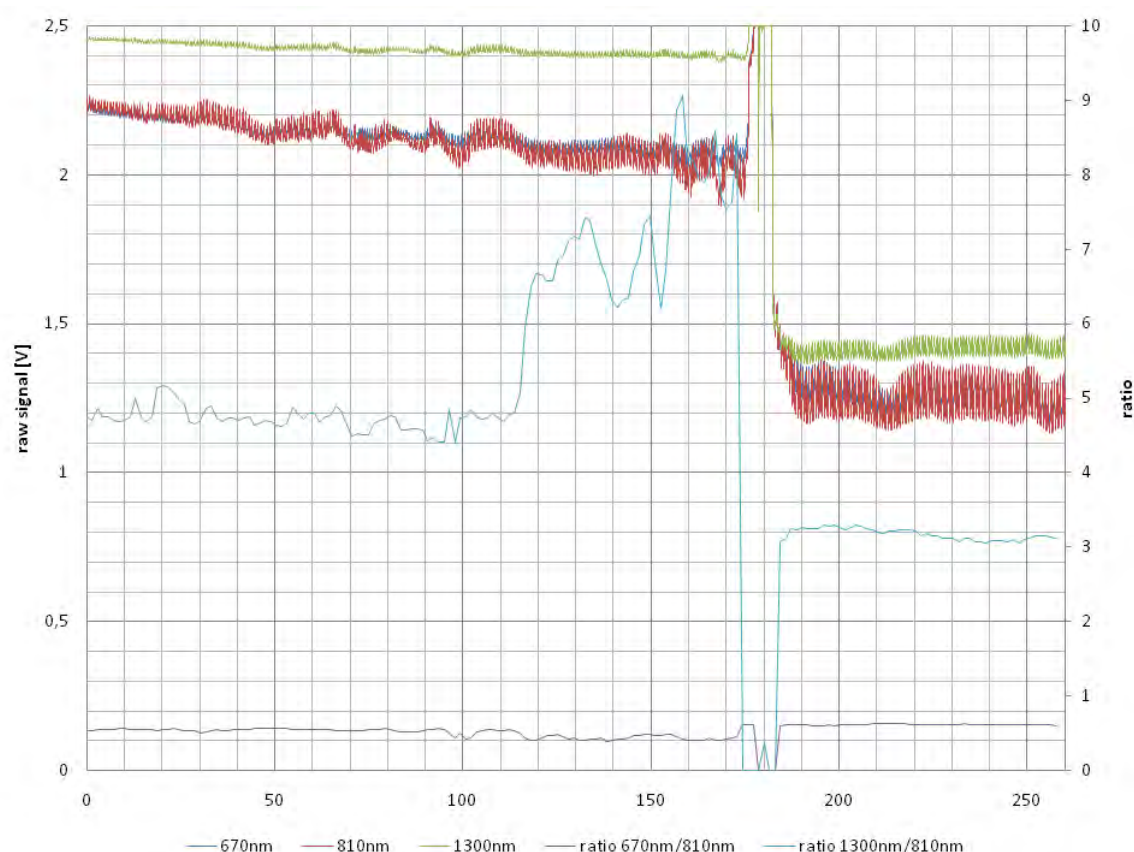


Figure 8-6: Raw signals and calculated ratios with raised contact pressure

### 8.3 Validation of the calibration curve

After the creation of a calibration curve, the sensor is capable of measuring the haemoglobin concentration online in humans. Therefore, in a second study twenty cHb measurements with the non-invasive device were compared with samples taken the HemoCue to validate the devices operation. Eleven male and nine female test subjects participated in the test. The test subjects were non-invasively measured for

around 3min and the cHb values were time averaged. Subsequently the time averaged cHb values were compared with invasive measurements taken with the HemoCue. The result of this test is shown in Figure 8-7.

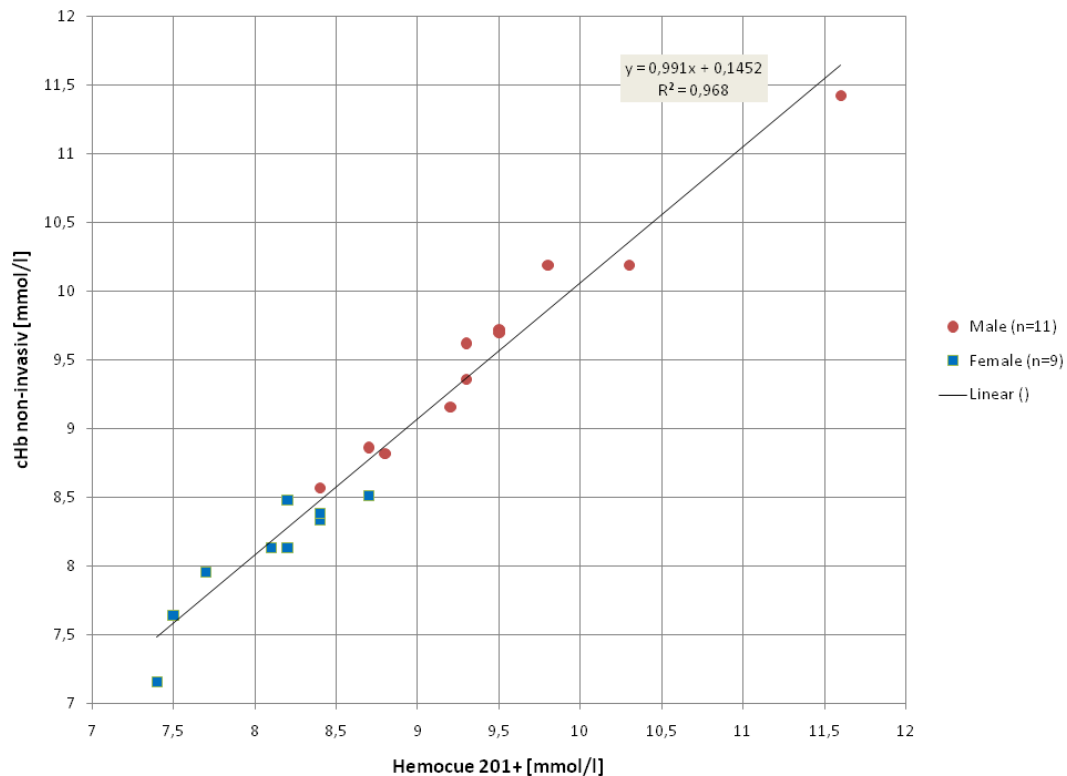


Figure 8-7: Comparison of twenty measurements from non-invasive Hb device and the HemoCue

A validation of the results is observed with a Bland-Altman-plot, which is shown in figure 8-8. Additionally the mean difference and the mean difference plus/minus the twice standard deviation are presented (confidence interval 95%). The standard derivation is 0.1817mmol/l and the mean difference is 0.06363mmol/l. Note that a systematic error between both methods cannot be observed or excluded as possibility. Nonetheless, the trend is marginally more an overestimation than an underestimation of cHb by the non-invasive device. Over the whole bandwidth from 7mmol/l up 11.5mmol/l a uniform distribution inside the confidence interval can be observed.

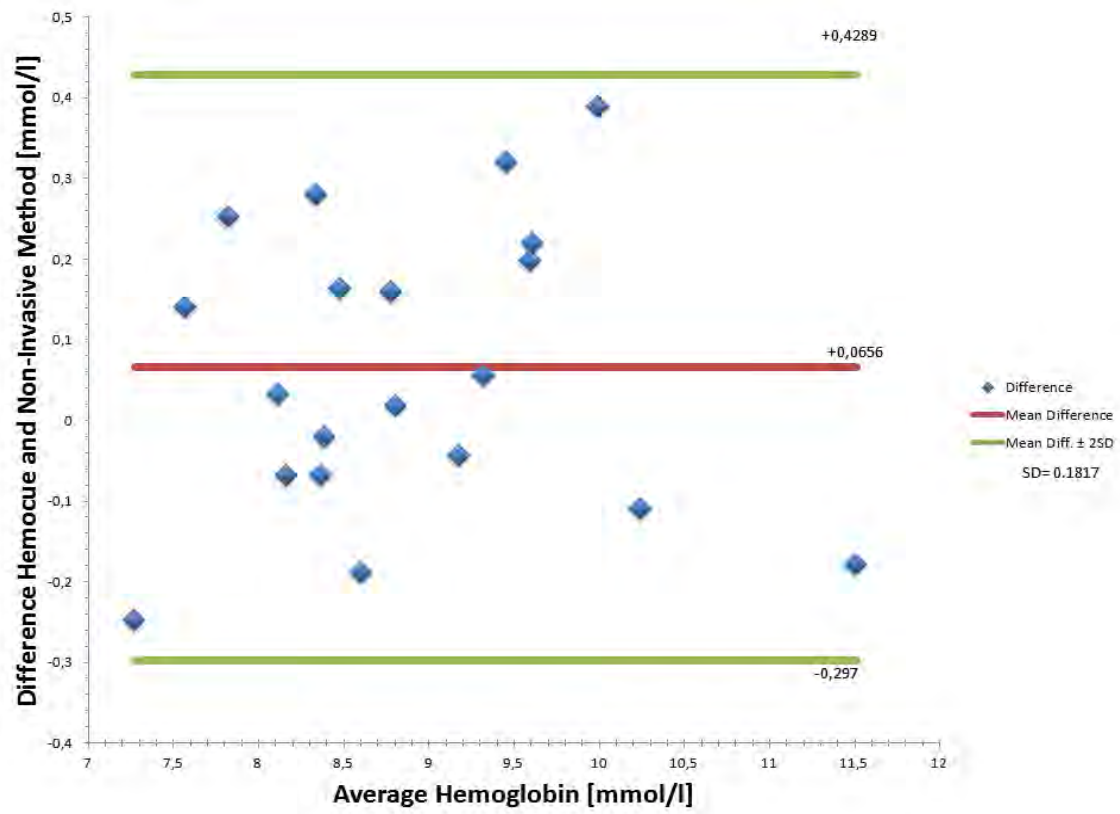


Figure 8-8: Bland Altman Plot to compare both measurement methods

## 8.4 Discussion

During the development process many different sensors were constructed and tested. It is evident that fabrication tolerances of the LEDs have a significant influence on results. During the study just one clip was used and therefore a systematic error caused by the hardware was potentially prevented. Figure 8-9 shows the comparison of the calibrated finger clip with a second uncalibrated clip.

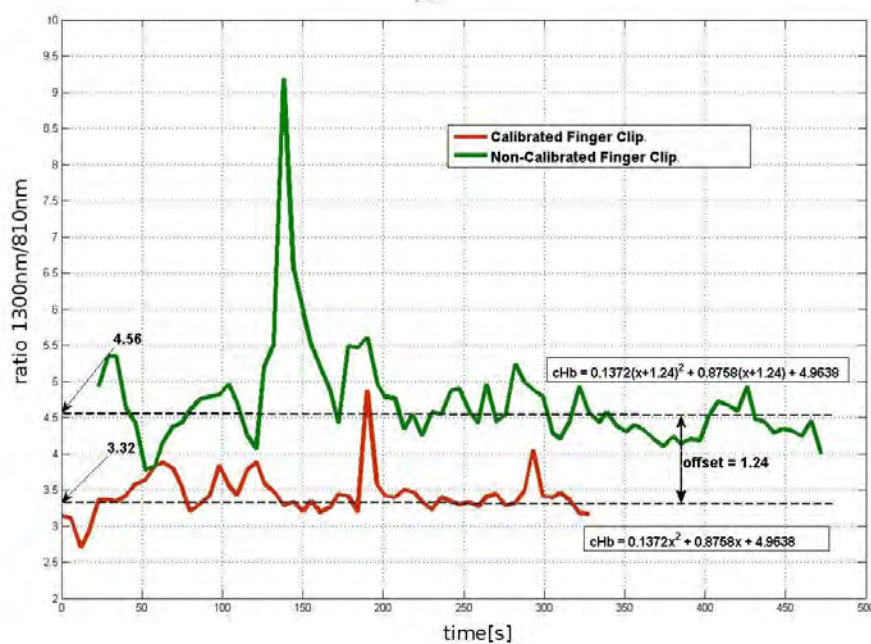


Figure 8-9: Comparison of two finger clips

The measurements presented in Figure 8-9 took place under real conditions with movement artefacts. Both clips were mounted on the right hand of the subject on different fingers. The settings such as power output and buffer length of both sensors system were the same. As a result of this comparison an offset drift between the two clips can be observed. The significant difference in ratio of 1.24 equates to around 2mmol/l and is caused by a wavelength shift of the 1300nm LED. Both LED spectra are shown in figure 8-10. The spectra of the 810nm LEDs were measured as identical.

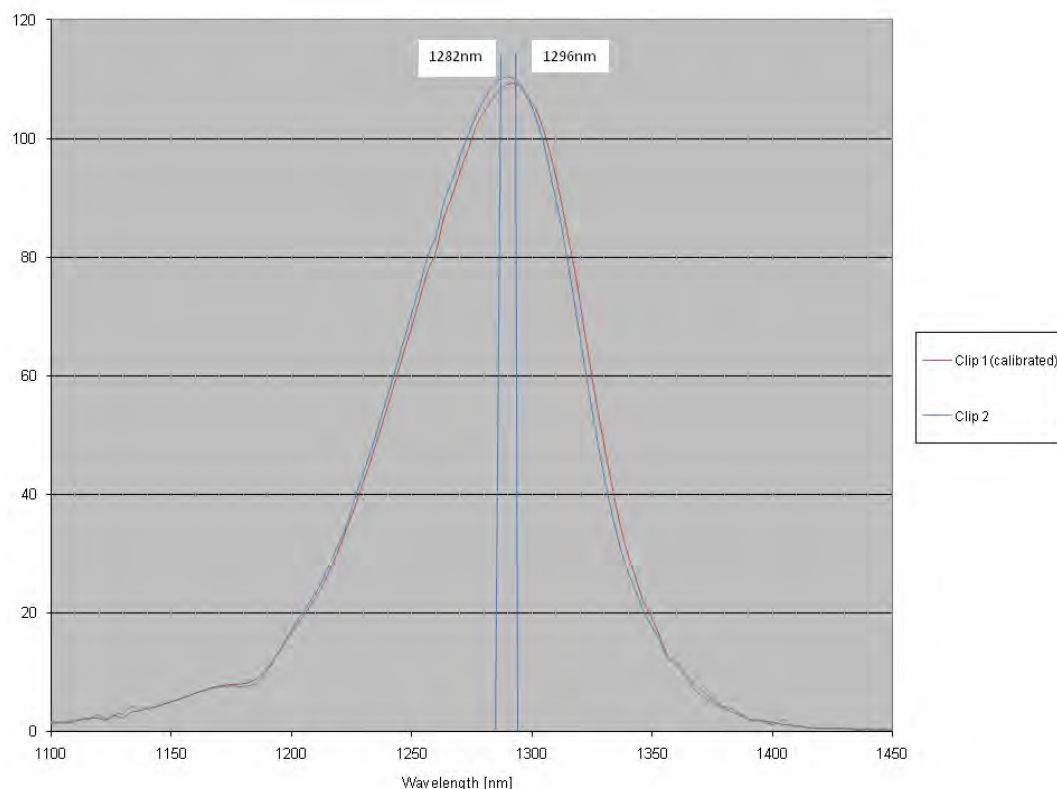


Figure 8-10: Wavelength shift between two clips

The large difference between both clips can be explained by the central wavelength shift of the LEDs, which is 14nm as shown in Figure 8-10. Due to the measurement occurring on a slope (Figure 7-3), the wavelength shift produces an exponential change in the absorbance value. To eliminate this potential error source resulting in manufacturing tolerances, LEDs with peak wavelengths of 1450nm or 1600nm would potentially solve this issue. At these wavelengths the absorbance characteristic of water is linear and a wavelength shift will not have a significant influence on the measurements. At the beginning of this research project, LEDs of sufficiently high power output with peak wavelengths at 1450nm or 1600nm were not available. However, in the meantime such LEDs have become available and it remains open for further research to test the operation of these wavelengths. For single research based prototypes it is a relatively insignificant consideration, as the finger clips are individually calibrated, however in case of a future commercialisation it will be an important consideration.

## 9 Summary and Outlook

During the perioperative period, which includes the period before surgery (preoperative), during surgery (intraoperative) and after surgery (postoperative), it is essential to measure diagnostic parameters such as: blood oxygen saturation; haemoglobin (Hb) concentration; and pulse rate. The Hb concentration in human blood is an important parameter to evaluate the physiological condition of an individual, as Hb is the oxygen carrying component of red blood cells. By determining the Hb concentration, it is possible, for example, to observe intraoperative or postoperative bleeding, and use this information as a trigger for autologous/allogenic blood transfusions.

The primary objective of this research has been the development of a non-invasive, real-time, Haemoglobin monitor based on the photo-plethysmography (PPG) method and using LEDs as the frequency sources. The system developed operates in the spectral range between 600nm and 1400nm. In an analogous way to pulse oximeters, the Hb sensor is clipped on a fingertip and light is transmitted through the fingertip. The system provides continuous real-time monitoring of the Hb concentration without the need to take blood samples.

This thesis discusses the theory needed to understand and design such a device, e.g.: the transport of light in biological tissue and turbid media; the PPG method; and a model for non-invasive Hb measurement is derived from first principles.

In order to empirically validate the theory of the Hb system, a prototype Hb sensor system and an artificial blood flow model were constructed, which simulate the human circulatory system. The blood flow model allowed a controlled variation of the oxygen saturation and haemoglobin concentration. Results obtained from spectrometer measurements and from the non-invasive Hb sensor system presented in chapter 7. Thereby the sensor system was attached to the blood tube and the spectrometer measurements were realised with optical cuvettes. A blood spectrum from 600nm to 1400nm with different haemoglobin and oxygen saturations was created. It is shown that an exact non-invasive Hb measurement is feasible with the chosen wavelengths at 810nm and 1300nm and that the measurement does not

depend on the oxygen saturation. A new developed algorithm for the pulse wave detection was used during all measurements. By comparing the new algorithm with a classic AC/DC peak method the new algorithm shows an improved detection rate in case of corrupted pulse waves caused by movement or low perfusion.

In a subsequent phase of the research project, the *in vivo* non-invasive haemoglobin concentration was successfully proven to be accurate by comparing it with invasive haemoglobin measurements. A clinical study was undertaken in the Graduate Medical School of the University of Limerick whereby blood samples of group of seventy-seven people were taken and subsequently analysed. Out of these data a calibration curve was created. The calibration curve with a coefficient of determination of 0.948, demonstrates the feasibility of an online haemoglobin measurement using this method.

In a second clinical study the non-invasive calculated Hb value obtained by using the calibration curve was compared with the invasive method. Thereby an accuracy of 0.43 mmol/l was reached. Actually this accuracy can only be reached by invasive methods and all non-invasive methods presented in chapter two do not reach this level.

The results show great promise but a final validation needs a clinical trial with more patients and a blood gas analyser as reference. It is also expected that the usage of sensors with fused photodiodes instead of the TO chassis will avoid measurements errors resulting from too high a contact pressure on the subjects finger.

As described in section 8.2.1 the usage of wavelength around 1600nm could further reduce the influence of wavelength shift on the final result. This is a preferred option if only one calibration curve is used for more than one sensor.

Finally it can be stated that a device was developed which would suit a clinical scenario where a detection of the haemoglobin is necessary. These would be the blood donation, during a surgery to monitor the blood transfusion, the perioperative area to detect inner bleeding and other. It can be also stated that the non-invasive measurement of total blood haemoglobin concentration is possible by using LEDs at centre wavelengths of 810nm and 1300nm. A US, EU and Irish patent application was filled in September 2010.

## 10 Own Publications

Timm, U., Lewis, E., Leen, G., Ewald, H., Kraitl, J. and McGrath, D., 'An analysis method and system for blood'. Filed US, EU and Irish patent application September 2010. (Patent)

U. Timm, G. Leen, E. Lewis, D. McGrath, J. Kraitl and H. Ewald "Non-invasive optical real-time measurement of total hemoglobin content" Eurosensor XXIV Conference, Eurosensor XXIV Conference, Volume 5, 2010, Pages 488-491

S. Andruschenko, J. Kraitl, U. Timm, E. Lewis, H. Ewald "A Novel Algorithm for "AC/DC" Ratio Calculation of Pulse Signals using Energy criteria of the Pulse" Biomed Tech 2010; 55 (Suppl. 1) Berlin • New York. DOI 10.1515/BMT.2010.675

S. Andruschenko, U. Timm, M. Hinz, S. Koball, J. Kraitl, E. Lewis and H. Ewald "Pulse Spectroscopy System for Non-Invasive Real-Time Monitoring of the Heart Beat Volume" The 9th IEEE Conference on Sensors (IEEE Sensors Conference), November 1-4, 2010, Waikoloa, Big Island, Hawaii

U. Timm, E. Lewis, G. Leen, D. McGrath, J. Kraitl and H. Ewald "Non-Invasive Optical Method to Determine the Total Hemoglobin Content in Real-Time", National Institute of Health Sciences Research Bulletin, December 2010

Timm U., Lewis E., Leen G., McGrath D., Kraitl J., and Ewald H., "Non-Invasive Continuous Online Hemoglobin Monitoring System". Fifth IEEE Sensors Applications Symposium (SAS-2010), 23<sup>rd</sup>-25<sup>th</sup> February, 2010. Limerick, Ireland. pp. 131-134. ISBN: 978-1-4244-4989-7

Kraitl J., Timm U., Lewis E. and Ewald H., "Optical sensor technology for a non-invasive continuous monitoring of blood components", BiOS, Spie Photonics West, 23-28 January 2010, San Francisco, California, USA

Timm U., Lewis E., McGrath D., Kraitl J., Ewald H., "A novel LED-Based Sensor System for Non-Invasive Hemoglobin Measurement" National Institute of Health Sciences Research Bulletin, December 2009

U. Timm, E. Lewis, D. McGrath, J. Kraitl, H. Ewald, "Sensor System for Non-Invasive Optical Hemoglobin Determination", The Eighth IEEE Conference on Sensors (IEEE Sensors Conference), October 25th-28th, 2009, Christchurch, New Zealand.

U. Timm, E. Lewis, D. McGrath, J. Kraitl, H. Ewald, "Sensor System Concept for Non-Invasive Blood Diagnosis", Eurosensors 2009, Lausanne, Switzerland, Procedia Chemistry, Volume 1, Issue 1, August 2009, Pages 493-496

Timm U., Lewis E., McGrath D., Kraitl J. and Ewald H., "Optical Sensor System for Non-Invasive Blood Diagnosis" , SAS 2009 – IEEE Sensors and Applications Symposium, 17-19 February 2009, New Orleans, LA, USA. pp 240-244, ISBN 978-1-4244-2787-1

Timm U., Lewis E., McGrath D., Ewald H., " Non-Invasive Optical Measurement of the Haemoglobin Concentration in Human Blood" National Institute of Health Sciences Research Bulletin, Decmber 2008, pp55, ISSN: 1649-0681

Timm U., Lewis E., McGrath D., Kraitl J. and Ewald H., "LED Based Sensor System for Non-Invasive Measurement of the Hemoglobin Concentration in Human Blood" , ICBME2008 -13th International Conference on Biomedical Engineering, 3-6 December 2008, Singapore, IFMBE Proceedings Vol.23 pp 825-829, ISBN 978-3-540-92840-9, ISSN 1680-0737

## 11 References

- [1] Zijlstra W. G., van Kampen E. J.: "Standardization of hemoglobinometry.I. The extinction coefficient of hemoglobincyanide.", *Clin. Chim. Acta* 5, pp.719-29, 1960
- [2] International Committee for the Standardization in Haematology; Expert Panel on Haemoglobinometry.: Recommendations for reference method for haemoglobinometry in human blood (ICSH standard 1986) and specifications for international haemoglobin-cyanide reference preparation", (3rd Edition), *ClinLab Haematol* 9, pp 73-79, 1987
- [3] Severinghaus, J.W. and Bradley, A.F.:" Electrodes for blood pO<sub>2</sub> and pCO<sub>2</sub> determination", *Journal of Applied Physiology* pp515=17, 1958
- [4] Clark Jr, L.C. and Lyons, C.," Electrode systems for continuous monitoring in cardiovascular surgery", *Annals of the New York Academy of Sciences*, pp29-45, 1962
- [5] Patricia L. Bounds Ph.D. "Blood Gas Analysis" The Gale Group Inc., Gale. *Gale Encyclopedia of Nursing and Allied Health*, 2002
- [6] Blumenthal S., Kakaty D. K., Marquardt M., Beck-Schimmer B., Borgeat A.: "Clinical Validation of the Hemocue Plasma Low Hemoglobin Photometer System", *ASA American Society of Anesthesiologists Annual Meeting*, San Francisco, CA, 2007
- [7] Gehring H., Hornberger C., Dibbelt L., Roth-Isigkeit A., Gerlach K., Schumacher J., Schmucker P.: "Accuracy of point-of-care-testing (POCT) for determining hemoglobin concentrations", *Acta Anaesthesiologica Scandinavica* 2002; 46, pp 980-86, 2002
- [8] Rosencwaig, A. and Griffiths, P.R." Photoacoustics and photoacoustic spectroscopy", *Physics Today* Volume 34., 1981
- [9] Deyo D.J., Esenaliev R.O., Hartrumpf O., Motamedi M.,Prough D.S. "Continuous noninvasive optoacoustic monitoring of hemoglobin concentration. *Anesthesiol Analgesia* 2001,92: S139
- [10] Esenaliev R.O, Petrov Y.Y., Hartrumpf O., Deyo D.J., Prough D.S., "Continuous, noninvasive monitoring of total hemoglobin concentration by an optoacoustic technique" *Appl Opt*, pp. 3401-7,2004
- [11] Petrova I.Y., Esenaliev R.O, Petrov Y.Y., Brecht H.P.E., Svensen C.H, Olsson J.," Optoacoustic monitoring of blood hemoglobin concentration: a pilot clinical study" *Opt Lett* Vol.30 2005, 1677-9
- [12] Secomski W., Nowicki A., Guidi F., Tortoli P., Lewin P.A. "Noninvasive in vivo measurements of hematocrit." *Journal Ultrasound Med* Vol. 22,2003 pp.375-84
- [13] Yamakoshi K.I., Shimazu H., Togawa T., Fukuoka M., Ito H. "Non-invasive measurement of hematocrit by electrical admittance plethysmography technique", *IEEE Trans Biomed Eng.* Vol27 1980, pp.156 – 61.

- [14] Yamakoshi K, Tanaka S, Shimazu H." Electrical admittance cuff for noninvasive and simultaneous measurement of hematocrit, arterial-pressure and elasticity using volume-oscillometric method" *Med Biol Eng Comput* Vol. 32 1994,pp.99-107.
- [15] John W. M., Gregory D. J., Selim S., Gregory Crawford, "Noninvasive Optical, Electrical, and Acoustic Methods of Total Hemoglobin Determination", *Clinical Chemistry* 54:2, pp264-272, 2008
- [16] Miller I. C., "Laser Ablation, Principles and Application", Springer Verlag Berlin, 1994
- [17] Takahisa U., Noriyuki T., Tamaki M, "Lower peripheral circulation in eumenorrhic young women with premenstrual symptoms, *BioPsychoSocial Medicine*, pp1-8, 2007
- [18] Jeon K.J., Kim S.J., Park K.K., Kim J.W., Yoon G. "Noninvasive total hemoglobin measurement" *Journal Biomed Opt.* Vol7, pp.45–50, 2002
- [19] Eisei Noiri; Naoki Kobayashi; Yoshiaki Takamura; Takehiko Iijima; Toshiyuki Takagi; Kent Doi; Akihide Nakao; et. al, " Pulse total-hemoglobinometer provides accurate *noninvasive monitoring*", *Crit Care Med* Vol 33 No12, 2005
- [20] Iwao Oshiro, Toru Takenaka and Jiro Maeda "New method for hemoglobin determination by using sodium lauryl sulfate" , *Clinical Biochemistry* Volume 15, Issue 2, Pages 83-88, April 1982
- [21] Emil H. Annabi, Steven J. Barker. , "Severel methaemoglobinemia detected by pulse oximetry" *Anesth Analg* 108: pp 898–899, 2009
- [22] Shvartsman LD, Fine I. Optical transmission of blood: effect of erythrocyte aggregation. *IEEE Trans Biomed Eng* Vol. 50, pp.1026 –33, 2003
- [23] Fine I, Geva D, Amir O, Monashkin E. "Clinical Evaluation of non-invasive hemoglobin testing device" *American Society of Anesthesiologists Annual Meeting* Vol. A-597. New Orleans, LA, 2004
- [24] Miller DR, Haynie ML, Levin NW, Brendolan A, Ronco C. Anemia screening via non-invasive transcutaneous measurement of hematocrit in hemodialysis and pre-ESRD patients." *Program and abstracts of Renal Week 2002: American Society of Nephrology 35th Annual Meeting; November 1-4, Philadelphia, 2002*
- [25] <http://www.critscan.com/home.html> 23.August 2010
- [26] McMurdy J.W., Jay G.D., Suner S., Trespalacios F.M., Crawford G.P. "Diffuse reflectance spectra of the palpebral conjunctiva and its utility as a noninvasive indicator of total hemoglobin." *J Biomed Opt.* 2006 Jan-Feb;11(1):014019.
- [27] Schmitt J. M., Zhou G. X., Walker E. C., Wall R. T.: "Multilayer model of photon diffusion in skin", *J. Opt. Soc. Am.* 7, 1990
- [28] Wilson B. C., Jacques S. L.: "Optical reflectance and transmittance of tissues: Principle and Applications", *IEEE J. Quan. Electro.* (26), 1990
- [29] Bergmann, Schäfer: *Lehrbuch der Experimentalphysik III - Optik*, 9. Auflage, de Gruyter Verlag, Berlin, New York (1993), S. 467

- [30] Hollis, V. "Non-Invasive Monitoring of Brain Tissue Temperature by Near-Infrared Spectroscopy" PhD Thesis, 2002
- [31] Bohren, C F, and Huffman "Absorption and scattering of light by small particles" First edn. New York: John Wiley and Sons, 1983
- [32] Jenkins, F A, and White, "Fundamentals of optics" Fourth edn. New York: McGraw-Hill., 1981.
- [33] Tuchin V.: Handbook of Optical Biomedical Diagnostics, Bellingham, USA: SPIE Press, pp. 206-207, 2002.
- [34] V. Tuchin, S. Utz, and I. Yaroslavsky, "Tissue optics, light distribution, and spectroscopy," *Opt. Eng.* 33, 3178–3188, (1994).
- [35] A. Ishimaru, "Wave Propagation and Scattering in Random Media," Academic, New York, Vol. 1, (1978).
- [36] V. Tuchin, Biomedical Photonics Handbook, chapter Light-Tissue Interactions, pages 3–1. CRC Press, Boca Raton, FL, USA (2003).
- [37] Phys104 - How Things Work (webpage) University of Maryland, College Park Fall 2008, Prof. Ted Jacobson
- [38] Bott A., Zdunkowski W.: "Electromagnetic energy within dielectric spheres" *J. Opt. Soc. Am. A* 4, 1361-1365, 1987
- [39] van de Hulst H. C.: "Multiple Light Scattering", Volume 1, Academic Press, New York, 1980
- [40] Mie G.: "Beitraege zur Optik trueber Medien, speziell kolloider MetallÄosungen", *Ann. Phys. IV*, pp 377-445, 1908
- [41] Chance B., Alfano R., Tromberg B. J. (Hrsg.): *Optical Tomography and Spectroscopy of Tissues III*, SPIE Vol. 3597, Bellingham, Washington, 1999
- [42] Zijp J. R., Bosch J. J.: "Pascal program to perform Mie calculations", *Opt. Eng.* 32(7), pp 1691-1695, 1993
- [43] Chandrasekhar S.: *Radiative Transfer*, Oxford Univ. Press, London, New York, 1950
- [44] M. Schweiger and S. Arridge, "The finite-element method for the propagation of light in scattering media: Frequency domain case," *Med. Phys.*, 24(6), 895–902, 1997
- [45] Ishimaru A.: "Diffusion Approximation in Wave propagation and scattering in random media", Academic Press, New York, 1978
- [46] Furutsu K.: "Diffusion equation derived from space-time transport equation" *J. Opt. Soc. Am.* 70, pp 360-366, 1980
- [47] Yoo K. M., Liu F., Alfano R. R.: "When does the diffusion approximation fail to describe photon transport in random media?", *Phys. Rev. Lett.* 64, pp 2647-2650, 1990
- [48] M. Patterson, B. Chance, B. Wilson, "Time Resolved Reflectance and Transmittance for the Noninvasive Measurement of Tissue Optical Properties," *Appl. Opt.* 28, 2331-2336, 1989

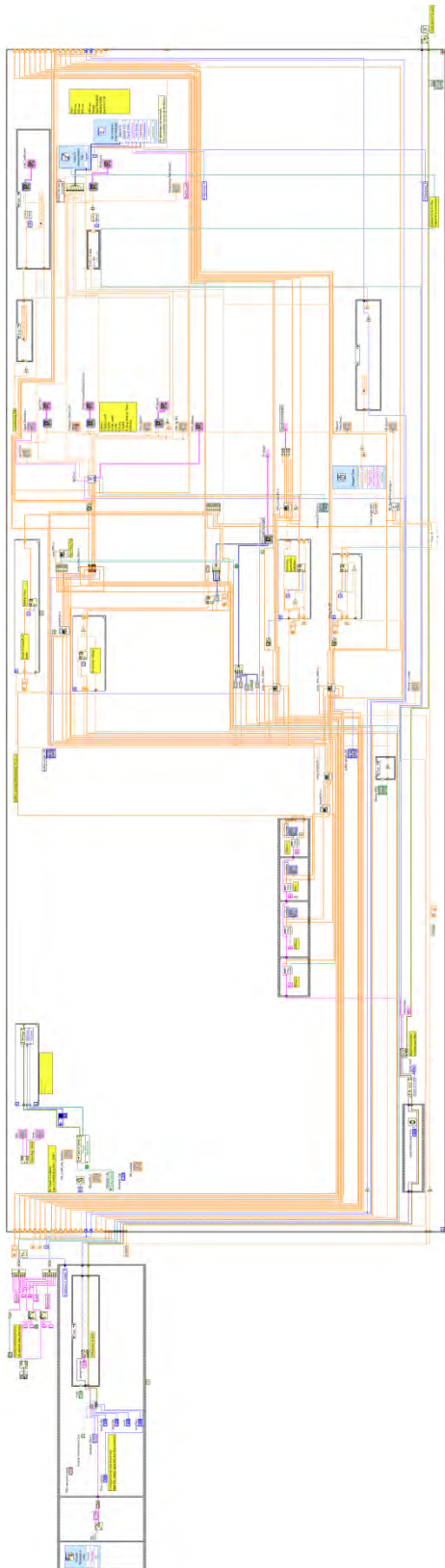
- [49] Cheong W.-F., Prahl S. A., Welsh A. J.: "A Review of the Optical Properties of Biological Tissues" IEEE J. Quant. Elect. 26, 2166-2185, 1990
- [50] Tromberg B. J., Svaasand L. O., Tsay T. T., Haskell R. C.: "Properties of photon density waves in multiple-scattering media" Appl. Opt. 32, 607-616, 1993
- [51] Ulbricht R.: "Die Bestimmung der mittleren räumlichen Lichtintensität durch nur eine Messung" Electrotech. Z. 21, 595-597, 1900
- [52] Van Albada M. P., van Tiggelen B. A., Lagendijk A., Tip A.: "Speed of Propagation of Classical Waves in Strongly Scattering Media" Phys. Rev. Lett.66, 3132-3135,1991
- [53] Roggan A., Minet O., Schroeder C., Mueller J.: "Determination of optical tissue properties with double integrating sphere technique and Monte Carlo simulations", Proc. SPIE 2100, pp 42-56, 1994
- [54] Roggan A., Friebel M., Doerschel K., Hahn A. and Müller G. : "Optical properties of circulating human blood in the wavelength range 400-2500 nm", J. Biomed. Opt. 4, pp 36-46, 1999
- [55] Winslow R. M., Rossi-Bernadi L.: "Oxygen-hemoglobin dissociation curve " in Crystal R. G., West J. B. et al., The lung: scientific foundations, New York, 1991
- [56] Weiss C.: "Funktion des Blutes", in Schmidt R. F., Thewes G. (Hrsg.): Einführung in die Physiologie des Menschen, 18. Auflage, Springer Verlag, Berlin, 1976
- [57] Schmidt R., Thewes G., Lang F.: "Physiologie des Menschen", 28. Auflage, Springer Verlag, Berlin, 2000
- [58] Hoffbrand A.V., Pettit J.E., "Essential Haematology", Wiley-Blackwell; 4th edition , 2001
- [59] MedicineNet.com "Hematorcrit", 9/2010
- [60] Edward. M. Canham, MD, FCCP; and David A. Beuther, MD, FCCP " Interpreting Arterial Blood Gases" PCCU Article 2007
- [61] Zijlstra W. G., Buursma A., Meeuwssen van der Roest W. P.: "Absorption spectra of human fetal and adult oxyhemoglobin, de-oxyhemoglobin, carboxyhemoglobin, and methemoglobin", Clin. Chem. 37, pp 1633-1638, 1991
- [62] Barlow R. B., Jun R. B., Polanyi M. L.: "Absorption measurements for Oxygenated and reduced hemoglobin in the range 0.6  $\mu$ m - 1.88  $\mu$ m", Clin. Chem.8, pp 67-71, 1962
- [63] Busse R.: "Kreislaufphysiologie", Thieme Stuttgart, New York, 1982
- [64] Klemsdal TO, Andersson TLG, Matz J, Ferns GAA, Gjesdal K, Änggard EE. Vitamin E restores endothelium dependent vasodilation in cholesterol fed rabbits: in vivo measurements by photoplethysmography. Cardiovascular Research;28:1397-402, 1994
- [65] Skin schematic skinovation.ca , webpage 5/2010

- [66] Odland G., "Structure of the Skin," Goldsmith L. A. (publisher): Physiology, Biochemistry, and Molecular Biology of the Skin, 2 Edition, Oxford University Press, New York, Oxford, 1991
- [67] Saidi I. S.: Transcutaneous optical measurement of hyperbilirubinemia in neonates, PhD Thesis, Rice University, Houston, USA, 1992
- [68] Saidi I. S., Jacques S. L., Tittel K. F.: "Mie and Rayleigh modeling of visible-light scattering in neonatal skin" *Appl. Opt.* 34, 7410-7418, 1995
- [69] van Gemert M. J. C., Jacques S. L., Sterenborg H. J., Star W. M.: "SkinOptics", *IEEE Trans. Biomed. Eng.* 36, pp 1146-1154, 1989
- [70] Jacques S. L.: Skin Optics, Oregon Medical Laser Center, <http://omlc.ogi.edu/> (2010)
- [71] Sadar D. K., Levy L. B.: "Optical properties of whole blood", *Lasers Med. Sci.* 13, pp 106-111, 1998
- [72] Stenn K. S.: "The Skin", in Weiss L. *Cell and Tissue Biology, A Textbook of Histology*, 6th Edition, Urban und Schwarzenberg Verlag, Baltimore, 1988
- [73] Lakowicz J. R., Berndt K. W., Johnson M. L.: "Photon migration in scattering media and tissue" *Proc. SPIE* 1204, 468-480, 1990
- [74] Moyle J. T. B.: "Pulse Oximetry, Principles and Practice", *BMJ*, 1994
- [75] Webster J.G. "Design of Pulse Oximeters" Institute of Physics Pub. 1997
- [76] Middleton P. M., Henry J. A.: "Pulse oxymetry: evolution and directions", *Int. J. Clin. Pract.* 54, pp 438-444, 2000
- [77] Kaestle S. „Ein Algorithmus zur zuverlässigen Verarbeitung von Pulsoximetrie-Signalen bei schwierigen Stoe rverhaeltnissen. Logos Verlag Berlin, 1999.
- [78] Kraitl J. „ Die nichtinvasive Bestimmung der Haemoglobinkonzentration im Blut mittels Pulsphotometrie“ Dissertation Feb 2008
- [79] Tietze, U., Schenk, Ch., Gamm, E „Halbleiter-Schaltungstechnik“ SBN: 978-3-642-01621-9, 13.Auflage, 2010
- [80] Datasheet Epigap EPC-1300-1.0-4, 16.05.2008, Rev.03
- [81] Datasheet Texas Instruments OPA 381, November 2003, SBOS291G
- [82] Datasheet Texas Instruments MSP430F1611, August 2006, SLAS358E
- [83] <http://www.ni.com/labview>
- [84] S.Andruschenko, J.Kraitl, U.Timm, E.Lewis, H.Ewald "A Novel Algorithm for "AC/DC" Ratio Calculation of Pulse Signals using Energy criteria of the Pulse" *Biomed Tech* 2010 New York. DOI 10.1515/BMT.2010.675
- [85] Website National Instruments: [http://zone.ni.com/reference/en-XX/help/371361D-01/gmath/derivative\\_xt](http://zone.ni.com/reference/en-XX/help/371361D-01/gmath/derivative_xt), August 2010
- [86] Rutsch, T.L.; Sankar, R.; Scharf, J.E.: "Signal Processing Methods for Pulse Oximetry", in *Proc.Comp. Biol. Med.*, vol. 26, no. 2, pp. 143-159, 1996.

- [87] Baker S.J.; Shah N.K.: The effects of motion on the performance of pulse oximeters in volunteers, *Anesthesiology*, no. 8, pp. 86-101, 1997.
- [88] HemoCue, AB Box 1204, 262 23 Ängelholm, SWEDEN [www.hemocue.com](http://www.hemocue.com)
- [89] Website August 2010 <http://www.masimo.com/pulseOximeter/Rad5.htm>
- [90] Mannheimer, P.D. The physio-optics of pulse oximetry - Numerical modeling and clinical experience. University of Luebeck, Dissertation, 2004.
- [91] Webpage: [http://linuz.sns.it/~sthew/was/Water\\_absorption\\_spectrum.png](http://linuz.sns.it/~sthew/was/Water_absorption_spectrum.png)  
March 2011
- [92] Webpage: <http://en.wikipedia.org/wiki/Photoplethysmograph> Nov. 2010
- [93] Webpage Epigap: <http://www.jenoptik.com/de-LEDs> Nov. 2010
- [94] Webpage: <http://www.zawaj.com/askbilqis/> Nov. 2010
- [95] Webpage: <http://www.radiometer.com> Nov 2010
- [96] Webpage: <http://www.heartzine.com>

## 12 Appendix

### 12.1 Screenshot Block Diagram LabVIEW



**12.2 Ethic Approval University of Limerick****UNIVERSITY of LIMERICK**

O'LLScoil LUIMNIGH

16<sup>th</sup> March 2010

Prof. Elfed Lewis  
Department of Electronic and Computer Engineering  
University of Limerick

RE: **S&E10/12** Non-Invasive Hemoglobin Determination

Dear Elfed,

The Faculty of Science and Engineering Research Ethics Committee, at its meeting of 16<sup>th</sup> March 2010, reviewed the above application and raised concerns with regard to what procedure will be put in place if something unexpected is found in a participants' blood sample.

The Committee has approved the application subject to their concerns being addressed.

Yours sincerely

A handwritten signature in black ink, appearing to read 'T. McGloughlin'.

Prof. Tim McGloughlin  
Chair  
Science & Engineering Research Ethics Committee

c.c. Ulrich Timm, Deirdre McGrath